Two Dimensional and Layered Functional Materials: First-principles Theoretical Analysis

A Thesis

Submitted For the Degree of

DOCTOR OF PHILOSOPHY

in the Faculty of Science

by

Anjali Singh

THEORETICAL SCIENCES UNIT
JAWAHARLAL NEHRU CENTRE FOR ADVANCED SCIENTIFIC RESEARCH
Bangalore – 560 064

MAY 2017

To my mother and husband

DECLARATION

I hereby declare that the matter embodied in the thesis entitled "**Two Dimensional and Layered Functional Materials: First-principles Theoretical Analysis**" is the result of investigations carried out by me at the Theoretical Sciences Unit, Jawaharlal Nehru Centre for Advanced Scientific Research, Bangalore, India under the supervision of Prof. Umesh V. Waghmare and that it has not been submitted elsewhere for the award of any degree or diploma.

In keeping with the general practice in reporting scientific observations, due acknowledgement has been made whenever the work described is based on the findings of other investigators.

Anjali Singh

CERTIFICATE

I hereby certify that the matter embodied in this thesis entitled "**Two Dimensional and Layered Functional Materials: First-principles Theoretical Analysis**" has been carried out by Ms. Anjali Singh at the Theoretical Sciences Unit, Jawaharlal Nehru Centre for Advanced Scientific Research, Bangalore, India under my supervision and that it has not been submitted elsewhere for the award of any degree or diploma.

Prof. Umesh V. Waghmare
(Research Supervisor)

Acknowledgements

I take this opportunity to thank my advisor Prof. Umesh V. Waghmare for his constant motivation and excellent guidance throughout my Ph.D. Working with him has been a thoroughly enjoyable experience, and his contagious enthusiasm for science has motivated me at various times. His valuable comments and instructions in preparing for seminars and writing papers have helped me immensely. I am extremely grateful for his kindness, endless support and encouragement during my stay at JNC.

I would like to express my gratitude to Prof. C.N.R. Rao, Prof. A. K. Sood and Prof D. D. Sarma for the interesting and fruitful scientific collaborations. I have greatly benefited from their expertise, and learned a lot in the process.

I would also like to thank Uttam Gupta, Manoj Kumar Jana, Dr. Biswanath Chakraborty, Achintya Bera, Satyendra Gupta and Banabir Pal for helpful collaborations.

I thank all the TSU faculty: Prof. Shobhana Narasimhan, Prof. Kavita Jain, Prof. Subir K Das, Prof. Swapan K. Pati, Prof. Vidyadhiraja and Prof. Meher K. Prakash for their instructive and enjoyable courses, and stimulating scientific interactions.

I would like to thank Prof. Chandrabhas Narayana and Prof. Balasubramanian for their interesting courses and scientific interections during the classes.

I would like to thank Jawaharlal Nehru Centre for Advanced Scientific Research, India for a research fellowship and Indo-Korea Science and Technology and JNCASR for funding my foreign visits.

I thank my present and past lab mates Sharmila, Meha, Vinay, Summayya, Krishnamohan, Jayshree, Abhishek, Koushik, Arpita, Suchitra, Pawan, Shashwat, Sandhya, Harish and Henu for the co-operative and cheerful environment. We had

scientific as well as non-scientific discussion in coffee breaks and group meetings.

I would like to acknowledge here the support in the form of computational facilities provided by the Centre for Computational Material Science (CCMS), JNCASR using which some of the calculations in the work presented here were performed. I would also like to thank the Complab staff, Vijay (CCMS) and Ananda Raman (CCMS) for tending to our problems at any time of the day.

I also extend my gratitude to Librarian, Academic and Administrative staff for their efficiency and helpfulness.

I take this opportunity to thank all my friends: Meha, Ananthu, Vinay, Sharmila, Chakri, Vybhav, Vinutha, Vijay, Darshana, Aditya, Shahab and Raj Kumar for their support and help.

I would also like to thank the Hostel staff, Mess workers and Chandraiah canteen for keeping me well fed. Sharanappa and Shivuanna for the hot cup of coffee, and Raju for maggi through wee hours during my stay in hostel.

I am thankful to Aruna and Kruti for their warm generosity, and for making me feel like a family.

Last but not the least, my parents (Maa and PaPa) and husband (Vishwesh) for their unending support and encouragement. They have always believed in me and shown me a right path in my hard times.

Synopsis

Technological growth is usually enabled and nurtured by the discovery of materials that exhibit excellent properties and can be grown readily. With advances in scientific theories, computational algorithms and resources, materials can be designed and their responses to external stimuli can be determined through computer simulations based on fundamental principles of physics. With these advances, computer simulations have become important in understanding and complementing experiments. In this end, first-principles density functional simulations have become powerful tools to obtain the accurate estimates of the properties. They permit prediction of the stability of new materials and their properties under the influence of external stimuli, providing access to atomistic information that is not readily accessible to experiments.

The thesis is broadly divided into three parts based on the kind of materials studied here. The first part (chapter 3) focuses on the theoretical analysis of how line defects (i.e. grain boundaries) influence the properties of 2D h-BN. The second part (chapter 4, 5, 6), focuses on detailed analysis of group VI transition metal dichalcogenides (TMDCs) in their bulk and two dimensional forms. In this part, we study various polymorphs of group-VI TMDCS, their structural phase transition, point defects, and effects of external pressure on their properties. The third part (chapter 7) presents a study of black phosphorous under pressure and effects of carrier doping on its vibrational properties.

Our simulations bridge the gap between theory and experiment, and allow us to access the information which is not readily available to experimental techniques. For example, with these calculations, one can focus on (1) a given type of defects at a time and study their effect on properties (first part of the thesis) and (2) effects of

carrier doping on electron-phonon coupling of phosphorene, which are useful characterization of the concentration of doping in devices. We highlight the usefulness of our work in developing a better understanding of experimental observations.

List of Publications

(1) **Anjali Singh** and Umesh V. Waghmare "Structural instabilities and wrinkles at the grain boundaries in 2-D h-BN: a first-principles analysis", *Phys. Chem. Chem. Phys.,* ***16****, 21664,* ***2014****.*

(2) Uttam Gupta, B.S. Naidu, Urmimala Maitra, **Anjali Singh**, Sharmila Shirodkar, Umesh V. Waghmare and C.N.R. Rao, "Characterization of few-layer 1T-$MoSe_2$ and its superior in the visible-light induced hydrogen evolution reaction", *APL Materials,* ***2****, 092802,* ***2014****.*

(3) **Anjali Singh**, Sharmila N. Shirodkar and Umesh V. Waghmare, "1H and 1T polymorphs, structural transitions and anomalous properties of$(Mo,W)(S,Se)_2$ monolayers: first-principles analysis", *2D Materials,* ***2****, 035013,* ***2015****.*

(4) Manoj K. Jana, **Anjali Singh**, Dattatray J. Late, Catherine R Rajamathi, Kanishka Biswas, Claudia Felser, Umesh V. Waghmare, C. N. R. Rao, "A combined experimental and theoretical study of the electronic and vibrational properties of bulk and few-layer Td-WTe_2", *J. Phys.: Condens. Matter,* ***27****, 285401,* ***2015****.*

(5) Biswanath Chakraborty, Satyendra Gupta, **Anjali Singh**, Manabendra, Kuiri, Chandan Kumar, D Muthu, Anindya Das, Umesh Waghmare and A. K. Sood, "Electron-hole asymmetry in the electron-phonon coupling in top-gated phosphorene transistor", *2D Materials,* ***3****, 015008,* ***2016****.*

(6) Achintya Bera, **Anjali Singh**, D.V.S. Muthu, U.V.Waghmare and A. K. Sood, "Pressure-dependent semiconductor to semimetal and Lifshitz transitions in 2H-$MoTe_2$: Raman and first-principles studies", *under review in JPCM.*

(7) Manoj Kumar Jana, **Anjali Singh**, Archana Sampath, U. V. Waghmare and

CNR Rao, "Structure and electron-transport properties of anion-deficient $MoTe_2$: a combined experimental and theoretical study", *in press.*

(8) Banabir Pal, **Anjali Singh**, Sharada G., Pratibha Mahale, Abhinav Kumar, S. Thirupathaiah, H. Sezen, M. Amati, Luca Gregoratti, Umesh V. Waghmare and D. D. Sarma, "Direct determination of the electronic structure of the elusive metastable state in chemically exfoliated MoS_2 layers", *under review in PRL.*

(9) Satyendra N. Gupta, **Anjali Singh**, Koushik Pal, Biswanath Chakraborti, D.V.S.Muthu, U. V. Waghmare and A. K. Sood, "Raman anomalies as signatures of pressure induced electronic topological and structural transitions in black phosphorus: Experiments and Theory", *under review in PRB.*

(10) Book Chapter: **Anjali Singh** and Umesh V. Waghmare, "Point defects, grain boundaries and planar faults in 2-D h-BN and TMX_2: Theory and Simulations"in 2-D Inorganic Materials beyond Graphene, CNR Rao and Umesh V. Waghmare, World Scientific Publisher, *in press.*

List of Figures

List of Tables

Contents

III Black Phosphorus

Chapter 1

Introduction

With emergence of two-dimensional materials marked with the experimental isolation of graphene by mechanical exfoliation of graphite in 2004 [2], the research field of 2-dimensional layered materials has witnessed a remarkable expansion with intense activity. Graphene and other 2-dimensional materials, such as transition metal dichalcogenides (TMDCs), hexagonal boron nitride, phosphorene, etc. have received tremendous attention in the fields of material science, nano-electronics, photonics, and energy technologies. In the bulk form, these materials have layered structure consisting of few-atom-thick sheets stacked and held together by weak van der Waals forces which allow their isolation into single 2D-layer or sheets. The family of 2D layered materials exhibits metallic, insulating, semiconducting and superconducting properties [3–6, 8–11, 195], which make it possible to realize various electronic and optoelectronic devices, giving rise to many new device concepts and theories.

Graphene is a semimetal with excellent electronic and thermal conductivity. With its high transparency due to monolayer thickness, graphene would be one of the best candidates for transparent conductors and electrodes [12]. Its peculiar electronic structure provides a platform to study various physical phenomena, such as massless Dirac fermions and anomalous room-temperature quantum Hall

effect [13, 14]. While the high carrier mobility of graphene is well suited for making field effect transistors (FETs), their on-off ratio is too low due to the vanishing band gap graphene [15]. This essentially means that there is need for other 2D materials with a finite band gap and high mobility which are suitable for nano-electronic devices. In this thesis, we investigate 2D materials beyond graphene using first-principles calculations and compare our results with experiments.

Semiconducting 2D materials such as TMDCs form another family of materials that offer very promising properties. Unlike graphene which is a semimetal and therefore unsuitable for digital electronics, these atomically thin layers possess a sizeble band gap which makes them suitable for building active electronic devices such as a field effect transistor, a basic unit of logic circuits and processors. The family of transition metal dichalcogenides (TMDCs) covers the need for 2D layered semiconductors with a vast spectrum of properties. Nowadays, these materials are particularly highlighted as the integrated circuit industry based on Si-MOSFET is approaching the limits of down-scaling, which has been used over decades to improve the processing power per unit area. 2D semiconducting TMDCs are considered to be a potential solution due to their ultrathin thickness, which allows efficient modulation of the carrier transport. Moreover, the direct band gap of monolayer TMDCs guarantee promising applications in optoelectronics, like light emitting diodes (LEDs) and photodetectors [16,17]. In addition, owing to the broken inversion symmetry of the crystalline structure of monolayer TMDCs, the spin-valley coupling leads to realization of novel spin-tronic and valley-tronic devices [18, 19]. In contrast to graphene, the on-off ratio of FETs made of TMDCs is sufficiently high [20]. However, the carrier mobility of TMDCs is relatively low, partly due to the localized d-electrons in the valence bands of the transition metal elements [21] and also the defects that are common in as-grown samples. Alternative 2D materials are still constantly sought for addressing these issues.

Few layers of black phosphorous is a relatively new member of the family of 2D materials with unique properties. Unlike gapless graphene, black phosphorous is a direct band gap semiconductor with gap ranging from 0.3 eV in bulk to 2 eV in monolayer [22–24], covering a wide range of electromagnetic spectrum. This is in contrast to TMDCs which exhibit a direct band gap of $\sim$ 1 to 2 eV only in their monolayer form. The narrow gap of black phosphorous (in few layer form) bridges the gap between the zero band gap graphene and large band gap TMDCs, making BP a suitable for mid infrared optics [25]. For possible applications in electronic devices, black phosphorous offers a good possibility with mobility of $\sim$ 1000 cm^2/V-sec at room temperature and on-off ratio of $\sim$ 10^5 with excellent current saturation [26]. Theoretically, much higher mobility (up to 10^5 cm^2/Vs) has been predicted for monolayered phosphorene [27]. With improved defect control and interface engineering, the mobility is expected to be further improved. If the issue with their stability in air can be adequately addressed, the few layers of phosphorene and black phosphorous could be potential candidates for next generation nanoelectronic applications.

This thesis is divided into three parts based on the 2-D materials studied. The first part focuses on the theoretical analysis of how line defects (i.e. grain boundaries) influence the properties of 2D h-BN and graphene. The second part presents on a detailed analysis of group VI transition metal dichalcogenides (TMDCs) in their bulk and two dimensional forms. In this part, we study various polymorphs of group-VI TMDCS, their structural phase transitions, point defects, and effects of external pressure on their properties. The third part presents a study of black phosphorous under pressure and effects of carrier doping on its vibrational properties. Our simulations studies bridge the gap between theory and experiment, and allow us to access the information which is not readily available to experimental techniques. We highlight the relevance of our work in developing better understanding

of experimental observations.

This thesis mainly focuses on effects of defects and external field on the materials studied here, and uses first-principles calculations effectively to determine and understand these effects on materials' properties.

1.1 Defects

Defects mean any region where the microscopic arrangement of atoms differs drastically from that of a perfect crystal. Defects are inherently present in materials, that appear during synthesis or treatment of material [28–30], and can have notable effects on a range of properties of the materials, such as electronic, optical, thermal properties, mechanical strength, electrical conductivity, corrosion and chemical reactivity. For example, mechanical strength and ductility of metals are determined by defects whereas electrical conductivity and thermal conductance of semiconductors are controlled by defects [31].

Defects are classified as planar, line, or point defects, depending on whether the imperfect region is bounded on the atomic scale in one, two or three dimensions. There are two types of defects (i) intrinsic and (ii) extrinsic defects [32]. Defects which appear as thermodynamic effects, and increase in number and size with increased temperature are known as intrinsic defects. Extrinsic defects are the ones which arise from the deviation in stoichiometry and do not necessarily depend on temperature. Intrinsic defects include point defects (vacancies), line defect (dislocations), grain boundaries, stacking and growth faults. In the structures with reduced dimensionality, the types of defects are fewer, and their effects become more pronounced in 2D materials. Due to their relevance to the technological applications, we have studied the grain boundaries and in hexagonal boron nitride (h-BN) [3] and planar defects in Group-VI transition metal dichalcogenides (TMDCs) [4]. We

identified the signatures in electronic and vibrational properties of these materials.

Grain boundaries or interfaces in 2D materials appear naturally during the growth of these materials [30]. At these interfaces, the atomistic structure deviates from the perfect crystal structure and leads to changes in electronic and optical properties [3, 30]. Grain boundaries lead to out-of-plane deformation of the flat 2D structures [3, 33]. h-BN has a tendency to form ripples or wrinkles in the presence of these interfaces. "Planar" defects are normally found in MX_2 type compounds whose single layer consists of 2-3 atomic planes (*e.g.* MoS_2). Planar defects can be introduced by sliding one atomic plane (out of 2-3 planes) with respect to the rest (keeping the other layers fixed) [4]. These planar defects introduce a structural transformation to 1T form, and gives rise to metal to semiconductor phase transition only in group IV MX_2. This 1T structural form shows interesting ferroelectric properties which can be utilized for device formation. In another work, we show how point defects (anion-deficiency) affect electronic and thermoelectric properties of $MoTe_2$.

1.2 Effect of External Field

External field (*e.g.* electric field induced charge doping and pressure) can be important in tunning the properties of nano-materials. Tunning these parameters or fields affect the performance of the devices like field effect transistors and sensors. Within experimental work alone, it is difficult to identify such effects of external field on these materials. Hence, theoretical study plays a important role in obtaining fundamental insights (electronic scale to macroscopic properties) of materials. For example, black phosphorous shows structural phase transition under external applied pressure whereas $MoTe_2$ undergoes electronic topological transition. Hydrostatic pressure changes the crystal structure of black phosphorus and modifies

its electronic properties. As the most stable known allotrope of phosphorus, black phosphorus exhibits transition to three different phases under moderate high hydrostatic pressures: the orthorhombic phase with wrinkled hexagons, the graphene-like rhombohedral phase with hexagonal lattice for pressures P $>$ 4.5 GPa, and the simple cubic phase with each P atom being in the octahedral center of other six P atoms for P $>$ 10.3 GPa. In contrast, $MoTe_2$ is remarkably robust and remains in the same structure upto 30 GPa, but shows isostructural and electronic topological transitions which are discussed in detail in this thesis. In our work on electron/hole doping in phosphorene, we explain the observed asymmetry in changes in properties with respect to electron and hole doing [6].

1.3 Why First-principles Theoretical Study?

Density functional theory is a powerful tool to determine the electronic ground state and predict structural properties of crystals, molecules and surfaces. For example a line defect in carbon nanotube was theoretically predicted using density functional theory [33], which was later verified experimentally [30]. This shows how the theoretical prediction and analysis of defects can facilitate experimental observation of these defects, and identify which properties of a material are affected by these defects. With these simulations one can focus on specific type of defects at a time and their interactions can also be studied, which is hard to access experimentally. We can control doping concentration with the help of these simulations, and avoid unintentional doping whereas the characterization of doping concentration is not straightforward experimentally. We can determine the effects of particular type of doping (hole/electron) on vibrational modes which is crucial information for experimental characterization (*e.g.* Raman spectroscopy) of nano-electronic devices.

We can access pressure dependent phase transitions associated with changes in electronic structure such as semiconductor to metal transition and topological transition (Lifshifz transition), while the electronic spectroscopy is tricky in experiments on materials under pressure.

1.4 Overview of the Thesis

The objective of this thesis is to determine physical properties and the behavior of 2D as well as bulk materials with and without structural imperfections or defects using first-principles theoretical calculations and explain experimental observations. The materials studied here are not only technologically important, but are also fundamentally interesting as they exhibit unusual phenomena involving physics of coupled electrons and phonons.

After a brief introduction, I emphasize the motivation and central ideas in this chapter. In chapter 2, I present a brief overview of the formalism and first-principles density functional theoretical methods used in this work. This thesis is organized in three parts based on the layered materials investigated.

Part I: 2D h-BN

In chapter 3, we determine the structure of grain boundaries (GBs) or faults, and study their effects on the electronic and vibrational properties of h-BN. As grain boundaries in graphene are well studied, we compare our results obtained for h-BN with those on graphene. We first present the schemes of classification and construction of GBs in 2-D h-BN and graphene in terms of (a) stacking faults and (b) growth faults. We show that a stacking fault involves linked rhombi and octagonal rings (4:8), and while a growth fault involves linked pentagonal and octagonal rings (5:5:8). While a growth fault is energetically more stable than a stacking fault in

graphene, the polarity of B and N results in reversed ordering of their stability in h-BN. Our analysis leads to prediction of new types of low-energy GBs of h-BN and graphene. At the fundamental level, we show that the planar structure is unstable with respect to buckling (out-of-plane deformation) that originates at the GB, which results in the formation of a wrinkle (short length scale buckling) at the GB as well as rippling (long length scale buckling) of the structure. We predict the variation in Raman and IR spectra as signatures of these GBs, and present scanning tunneling microscopy (STM) images, that would facilitate experimental characterization and validation of our theoretical predictions.

Part II: Group VI Transition Metal Dichalcogenides

Monolayered transition metal dichalcogenides (MX_2, M= Mo, W and X= S, Se) are two-dimensional semiconductors exhibiting interesting physical and chemical properties, and have the potential to be used in nano-electronic devices. Among the 1H and 1T structural forms exhibited by monolayers of transition metal dichalcogenides, the group VI compounds MX_2 (M= Mo, W and X= S, Se) largely occur in the 1H form. Recently, transformation of the 1H form to the 1T form with metallic electronic structure at high temperatures was demonstrated in MoS_2 with Re-substitution, and upon electron irradiation. In chapter 4 (a), we present the energy landscape associated with the 1H to 1T phase transition, and relate the observed intermediate structures to the structural instabilities of the 1T structure of MX_2 compounds. We show that the metallic centrosymmetric 1T (c1T) structure of these compounds is generally unstable with respect to dimerization or trimerization of metal atoms, leading to competing metallic $\sqrt{3}\times 1$ 1T form and ferroelectric semiconducting $\sqrt{3}\times\sqrt{3}$ 1T form respectively. While the former is a more stable 1T form of $MoSe_2$, WS_2 and WSe_2, the latter is a more stable 1T form of MoS_2 exhibiting rich ferroelectric dipolar domain structure. With vicinity to metal-semiconductor

transitions, their semiconducting forms are shown to exhibit anomalous response to applied electric field. To facilitate experimental verification of these subtle features of the 1T forms of MX_2 monolayers, we present comparative analysis of their vibrational properties, and identify their Raman and Infra-Red spectroscopic signatures.

Next, electronic structure of the 1T metastable phase of MoS_2 is analyzed in-depth. While the potential of 1T MoS_2 phase for different technological applications has been appreciated, basic understanding of its electronic nature is still lacking. 1T MoS_2 can exist in several structural forms (*e.g.* 1T′, 1T″ and 1T‴). In chapter 4 (b), with self-energy corrected first-principles calculations of its electronic structure, we show that the 1T′ phase is relevant to experimental samples grown by chemical exfoliation, and has the ground state with a small bandgap ($\sim$ 90 meV). Thus, it is semiconducting in contrast to many claims of its metallic behavior in the literature[3]. Our finding complements the work by experimentalists (Prof. D. D. Sarma's group, IISc), to find out which structural form of 1T MoS_2 is present in their samples.

In chapter 4 (c), we provide a possible explanation for how $MoSe_2$ has superior photo-catalytic activity compared to MoS_2 in both 1H and 1T structures towards hydrogen evolution reaction (HER). First-principles calculations reveal that 1T-$MoSe_2$ has a lower work function than 2H-$MoSe_2$ as well as 1T and 2H-MoS_2, making it easier for an electron to be donated from 1T-$MoSe_2$ to reduce H^+ and produce H_2. Metallic 1T-$MoSe_2$ prepared by Li intercalation followed by exfoliation of bulk 2H-$MoSe_2$ shows excellent H_2 evolution activity in comparison to few-layered semiconducting 2H-$MoSe_2$. We show that 2D surfaces of MoS_2 and $MoSe_2$ do not quite adsorb hydrogen ($E_{ads} > 0$). To understand this, we simulated ribbons of MoX_2 (X = S, Se) with two different types of edges (Mo terminated edge and X terminated edge), and studied their interaction with H (with 100% H coverage at the edges). The binding energy of hydrogen at the metal edge is about the same in the two compounds, while the Se edge of $MoSe_2$ shows weaker binding with hydrogen than

the S edge of MoS_2. This investigation has helped us in understanding experiments (Prof. CNR Rao's group, JNCASR) that showed that $MoSe_2$ performs better as a catalyst for HER than MoS_2.

In chapter 5 (a), we present analysis of the behavior of bulk 2H-$MoTe_2$ under pressure, based on its electronic structure and vibrational properties determined by first-principles density functional theoretical calculations. We find a low pressure ($\sim$ 8 GPa) isostructural semiconductor to metal transition. The topology of the Fermi-surface evolves as a function of pressure, with abrupt appearance of electron and hole pockets at P $\sim$ 20 GPa marking a Lifshitz transition. In experiments, these transitions are marked by changes in the pressure coefficients of frequencies of A_{1g} and E^1_{2g} Raman modes as well as their relative intensity. Our theoretical analysis shows that the structure remains the same upto 30 GPa. We find that pressure has a strong influence on the electron phonon coupling (EPC) of A_{1g} mode, which is consistent with experiments. All the Raman active modes harden with increasing pressure, and EPC increases under compression due to changes in the Fermi surface. Our findings should stimulate further experiments on high pressure and low temperature resistivity to capture the anomalies near the Lifshitz transition.

In chapter 5 (b), we present first-principles calculations based on density functional theory to determine the nature of electronic states associated with Te-vacancies in 2H-, 1T′- and Td-$MoTe_{2-x}$. The defect states associated with Te-vacancies are shown to appear within the gap of 2H-$MoTe_2$ and in the pseudo gap of 1T′-$MoTe_2$, thereby reducing the band gap of the former and making the latter more metallic. These defect states are crucial in understanding the trends in the temperature-dependent transport properties of Te-deficient 2H- and 1T′-$MoTe_{2-x}$ observed in experiments. Pristine bulk 2H-$MoTe_2$ is an indirect gap semiconductor, whereas the pristine 1T′ and Td-forms of $MoTe_2$ are semi-metallic. The thermal conductivities of 2H-$MoTe_{2-x}$ and 1T′-$MoTe_{2-x}$ thus exhibit opposite trends with temperature due

to the dominant electronic contribution to the thermal transport in the latter. The trends in transport properties observed in experiments can be explained with theory only after taking into account Te-vacancies. We also present a comparative analysis of effects of local and non-local van der Waals interaction on the structure and band gap of bulk 2H-$MoTe_2$ and Te-deficient 2H-$MoTe_2$.

In chapter 6, we present first-principles theoretical analysis of structural, electronic and vibrational properties of monolayered and bulk forms of Td-WTe_2. Spin-orbit coupling is shown to govern the semi-metallic character of Td-WTe_2. Frequencies and symmetry of the lattice vibrations of Td-WTe_2 obtained with first-principles calculations have been analyzed. Out of the 33 possible zone-center Raman active modes, five distinct Raman bands are observed near 112, 118, 134, 165 and 212 cm^{-1} in bulk Td-WTe_2. Based on the symmetry analysis and calculated Raman tensors, we assign the observed modes at 165 cm^{-1} and 212 cm^{-1} to the $A_1^{'}$ and $A_1^{''}$. We bring out the connection of the Td-structure with the c1T form of layered metal dichalcogenides, and explain its stability in terms of the electronic and vibrational properties of the c1T form. Most of the Raman bands harden with reducing thickness, and the ratio of integrated intensities of the $A_1^{''}$ to $A_1^{'}$ bands decreases in the few-layered samples consistent with experiment. Our finding helps in (a) identification of the symmetry of the intense modes observed in Raman spectra and (b) understanding the signatures of number of layers in Raman active modes.

Part III: Black Phosphorous

In chapter 7 (a), we report an extraordinary carrier dependent electron-phonon interaction in doped monolayer black phosphorus (BP) or phosphorene: the armchair oriented (polarized) in-plane A_g^2 phonon and out-of-plane A_g^1 phonon interact more strongly with electron-like carriers than the hole-like. The electron-phonon interaction captured through in-situ Raman spectroscopic studies in gated phosphorene

transistors in experiment, is confirmed with our density functional theory based calculations. We corroborate the line width broadening of A_g^2 and A_g^1 and phonon softening as a function of electron concentration seen in experiments. The other Raman active B_{2g} phonon with atomic displacement oriented along zigzag direction does not show any appreciable coupling to carriers. The Raman active modes with A_g symmetry respond more significantly to electron doping than to the hole doping. The contrasting effects of electron and hole doping on EPC are explained with symmetry arguments, and have been estimated quantitatively with first-principles calculations. The findings will be important in design of transistors with phosphorene, as the interaction of carriers with phonons is a deterministic factor in achieving desired carrier mobilities in devices.

In chapter 7 (b), we determine the Raman signatures of possible pressure dependent transitions in Black phosphorus (BP) up to 24 GPa. The electron-phonon coupling of Raman modes A_g^1, B_{2g} and A_g^2 of its orthorhombic phase show a minimum at ~ 0.6 GPa consistent with the observed Raman line-widths in experiment close to pressure dependent electronic topological transition (ETT), where band gap closes to zero. Frequencies of B_{2g} and A_g^2 Raman active modes become anomalous in the rhombohedral phase at 7.4 GPa, and the new modes appearing in the rhombohedral phase are also found to show anomalous softening with pressure as seen in experiments.

Chapter 2

Methods and Formalism

Materials are composed of atomic nuclei bound together by electrons, which are the fundamental particles and determine the properties of materials. Ground state properties of materials can be determined as first derivatives (*e.g.* stress, magnetization and forces are first derivative of energy w.r.t. strain, magnetic fields and atomic positions) and second derivatives (*e.g.* elastic constants, inter-atomic force constants and magnetic susceptibility are second derivative of energy w.r.t. strain, atomic positions and magnetic fields) of the total energy, which is the sum of the many electron ground state energy and electrostatic interaction between nuclei, within the adiabatic approximation.

The development of Density Functional Theory proposed by Walter Kohn [34] with a few approximations to ease the computational effort has led to significant advances in the theory and simulations of material properties. It is a theory of many-body fermionic system, with a mapping onto an independent fermion methods. DFT calculations have been used to make important contributions to a diverse range of compelling scientific questions, generating information that would be hard to determine with experimental work alone.

In this chapter, we discuss the theoretical methods which have been employed

in this thesis to determine the physical properties of the materials. We give a brief account of formulation of the density functional theory and its mapping to an independent-particle method to address the quantum ground state of many-body problem of electrons in materials. We discuss the technical details of calculating total energies, and describe Hybrid functional and GW approximations, which are useful in determining the excited state properties of materials. Next, we review two approaches of phonon calculations, namely, frozen phonons and linear response.

2.1 Introduction

The fundamental Hamiltonian of a system of interacting electrons and nuclei is given by,

$$\begin{aligned}\hat{H} = -\frac{\hbar^2}{2m_e}\sum_i \nabla_i^2 - \sum_{i,I}\frac{Z_i e^2}{|\mathbf{r}_i - \mathbf{R}_I|} + \frac{1}{2}\sum_{i\neq j}\frac{e^2}{|\mathbf{r}_i - \mathbf{r}_j|}, \\ -\sum_I \frac{\hbar^2}{2M_I}\nabla_I^2 + \frac{1}{2}\sum_{I\neq J}\frac{Z_I Z_J e^2}{|\mathbf{R}_I - \mathbf{R}_J|}\end{aligned} \tag{2.1}$$

where $\hbar$ is the Planck's constant, m_e and M_I are the masses of i^{th} electron and I^{th} ion respectively, e is the charge of an electron, and Z_I is the atomic number of the I^{th} ion, $\mathbf{r}_i$ and $\mathbf{R}_I$ are position vectors of i^{th} electron and I^{th} ion respectively. The first and the third terms in Eq. 2.1 are the kinetic and electrostatic interaction potential energies of electrons respectively. Whereas the fourth and the fifth terms are the kinetic and potential energies of ions respectively. The second term is the electrostatic interaction between ions and electrons, which is treated as an external potential for the electronic problem, and also include the effect of external perturbation such as electric or magnetic fields. The nuclear kinetic energy can be ignored, considering that the mass M_I is $\gtrsim 1836$ times that of electrons. This approximation is known as *Bohn-Oppenheimer* or the *adiabatic approximation*. Within this approximation,

the nuclear dynamics does not induce electronic transition, thus the many body wavefunction can be written as a product of electronic and nuclear wavefunctions,

$$\Psi(\mathbf{R}, \mathbf{r}) = \phi(\mathbf{R})\psi(\mathbf{R}, \mathbf{r}), \tag{2.2}$$

where $\psi(\mathbf{r}, \mathbf{R})$ is the electronic wavefunction of eigenfunctions corresponding to nuclear position $\{\mathbf{R}\}$, and $\phi(\mathbf{R})$ are nuclear wavefunction independent of electronic position ($\mathbf{r}$). The many-body wave-functions of electrons are obtained by time-independent Schrödinger equation:

$$\hat{H}\Psi(\mathbf{R}, \mathbf{r}) = \epsilon\Psi(\mathbf{R}, \mathbf{r}) \tag{2.3}$$

Substituting equation 2.1 and 2.2 in 2.3 we get,

$$\Big[-\frac{\hbar^2}{2m_e}\sum_i \nabla_i^2 - \sum_{i,I}\frac{Z_i e^2}{|\mathbf{r}_i - \mathbf{R}_I|} + \frac{1}{2}\sum_{i\neq j}\frac{e^2}{|\mathbf{r}_i - \mathbf{r}_j|} + \frac{1}{2}\sum_{I\neq J}\frac{Z_I Z_J e^2}{|\mathbf{R}_I - \mathbf{R}_J|}\Big]\psi_n(\mathbf{r}, \mathbf{R}) = E_n\psi_n(\mathbf{r}, \mathbf{R}), \tag{2.4}$$

and

$$\Big[-\frac{\hbar^2}{2M_I}\sum_I \nabla_I^2 + E_n\Big]\phi_m(\mathbf{R}) = \xi_m\phi_m(\mathbf{R}) \tag{2.5}$$

Here $\mathbf{r}_i$ is the position of electron i; r = $\{\mathbf{r}_i\}$. The ground state wavefunction ψ_0, *i.e* the lowest energy state, can be determined by minimizing the total energy with respect to all the parameters defining $\psi(\mathbf{r})$, with the constraint that ψ must obey the particle anti-symmetry and conservation laws. The Born-Oppenheimer approximation hence reduces the problem to solving for the ground state for a given set of ionic positions $\{\mathbf{R}_I\}$. However, the many-body electronic Hamiltonian in Eq.2.4 is difficult to be solved exactly as ψ_n is still a function of $3N_e$ variables (N_e

is the number of electrons in the system), hence other approximations are essential to solution of this eigenvalue problem.

2.2 Density Functional Theory

Density functional theory is a theory of correlated many-body systems, having a close association with independent-particle method. The work of Hohenberg-Kohn in 1964 [35], and Kohn-Sham in 1965 [34] led to the formulation of DFT, which has become a powerful tool today for treating electrons in atoms, molecules and condensed matter.

2.2.1 Hohenberg-Kohn Theorems

The two theorems proved by Hohenberg and Kohn form the basis to formulation of density functional theory as an exact theory for ground state of many-body fermionic systems.

Theorem I: The external potential $V_{ext}(\mathbf{r})$ of an interacting gas of electrons can be determined uniquely, within a constant, by the ground state particle density $n_0(\mathbf{r})$. Thus, all the properties of the system can be determined completely, once the ground state density n_0 is known.

Theorem II: A universal functional for the energy E[n] in terms of the density n($\mathbf{r}$) can be defined, for any external potential, $V_{ext}(\mathbf{r})$. For any particular $V_{ext}(\mathbf{r})$, the exact ground state energy of the system is the global minimum value of this functional, and the density n($\mathbf{r}$) that minimizes the functional is the exact ground state density $n_0(\mathbf{r})$. The total energy functional, as uniquely determined by n($\mathbf{r}$), is

$$E_{HK}[n] = T[n] + \int d^3r V_{ext}(\mathbf{r}) n(\mathbf{r}) + E_{int}[n] + E_{II} \tag{2.6}$$

where E_{II} denotes the energy of electrostatic interaction of nuclei.
A functional $F_{HK}[n]$, which includes kinetic and potential energies of interacting electron system, can be defined as:

$$F_{HK}[n] = T[n] + E_{int}[n] \tag{2.7}$$

Thus, if the functional $F_{HK}[n]$ is known, minimization of total energy with respect to n(r) can be used to determine, the exact ground state density and energy.
These Hohenberg and Kohn theorems make a significant contribution towards calculation of ground state energy by reducing it to the minimization problem with function of $3N_e$ to that of 3 variables. The difficulty with the above formulation is that there is no known way to extract kinetic energy directly from the density. The kinetic energy expressed in terms of N_e wavefunctions has derivatives as a functions of the number of electrons that are discontinuous at integer occupation numbers. This implies that the exact functional varies in a non-analytic manner as a function of number of electrons. This lead to Kohn and Sham approach, where kinetic energy is treated in terms of single particle wavefunctions and interaction terms as functionals of the density.

2.2.2 Kohn-Sham Ansatz

In the Kohn and Sham formalism [34], the exact Hamiltonian of an interacting many-body system is mapped onto a fictitious non-interacting single particle Hamiltonian, which can be solved efficiently. The total energy functional in Kohn-Sham formalism

can be written as,

$$E_{KS} = -\frac{\hbar^2}{2m}\langle\psi_i|\nabla^2|\psi_i\rangle + \int d\mathbf{r} V_{ext}(\mathbf{r})n(\mathbf{r}) + \frac{1}{2}\int d^3\mathbf{r}d^3\mathbf{r}'\frac{n(\mathbf{r})n(\mathbf{r}')}{|\mathbf{r}-\mathbf{r}'|} + E_{ion-ion} + E_{XC}[n],$$
$$= T_s[n] + \int d\mathbf{r} V_{ext}(\mathbf{r})n(\mathbf{r}) + E_{Hatree}[n] + E_{ion-ion} + E_{XC}[n], \tag{2.8}$$

where E_{Hatree} and E_{XC} are the Hartree and exchange-correlation contributions to the total energy and T_s is the non-interacting kinetic energy of electrons.

The Kohn-Sham non-interacting single particle Hamiltonian is

$$H_{KS} = T_s[n] + V_{KS}(\mathbf{r}), \tag{2.9}$$

where V_{KS} is Kohn-Sham potential which is defined as,

$$V = V_{ext}(r) + V_{Hatree}(r) + V_{XC}(\mathbf{r}) \tag{2.10}$$

where V_{ext}, V_{Hatree} and V_{XC} are external, Hartree and exchange-correlation potentials respectively. The single particle Kohn-Sham equations are

$$H_{KS}\psi_i(\mathbf{r}) = \epsilon_i\psi_i(\mathbf{r}) \tag{2.11}$$

and the ground state density can be written in the terms of single particle wavefunction, ψ_i as,

$$n(\mathbf{r}) = \sum_i^{N_e} |\psi_i(\mathbf{r})|^2, \ and \ N_e = \int d\mathbf{r}\ n(\mathbf{r}) \tag{2.12}$$

Since Kohn-Sham equations are non-linear equations (Eq. 2.11), a self-consistent iterative method is used to solve them as illustrated in Figure 2.1.

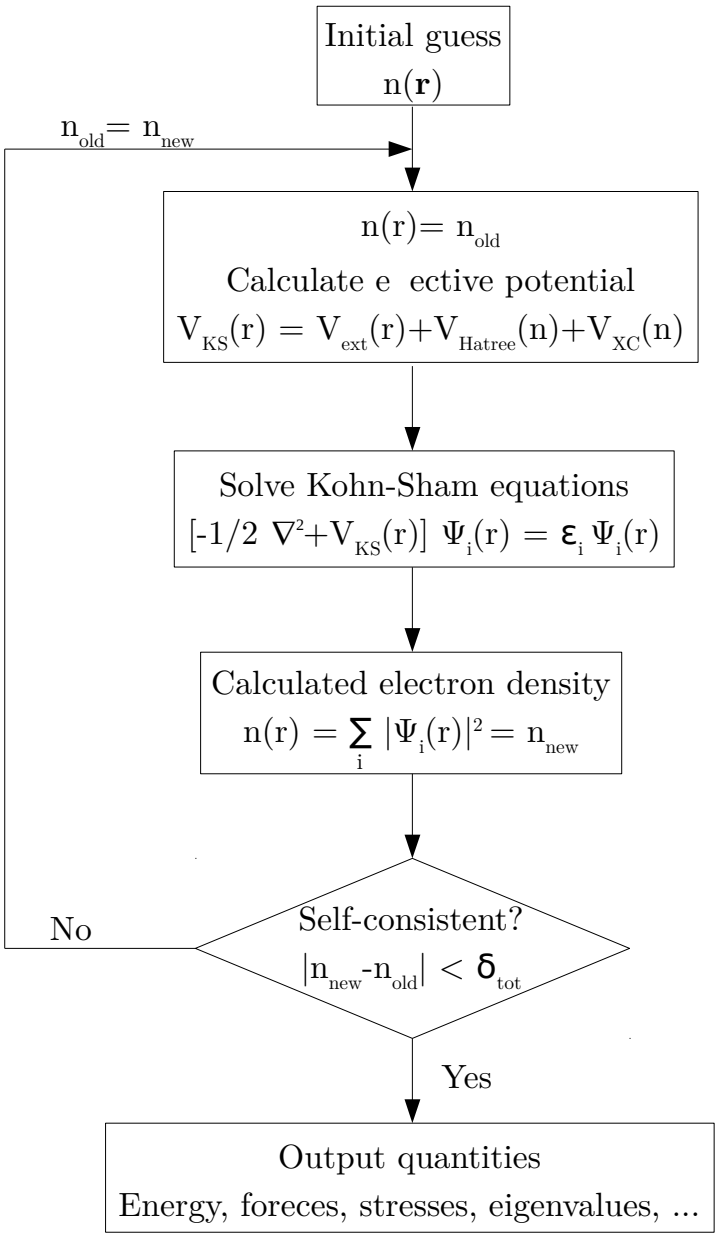

Figure 2.1: Flow chart showing the self-consistency loop for the iterative solution of Kohn-Sham equations.

2.2.3 Exchange-correlation functionals

All the many-body effects in kinetic, exchange and correlation are grouped into the exchange-correlation energy E_{XC}. It is defined as the difference of exact energy and Hartree energy. The exchange-correlation function is given as,

$$E_{XC}[n] = T[n] - T_s[n] + E_{ee}[n] - E_{Hatree}, \tag{2.13}$$

The exact form of exchange correlation energy function is not know, and the accuracy is limited by the approximations made in the formulation of this functional. There are two commonly used approximation to determine exchange-correlation energy, namely local density approximation (LDA) [34] and generalized gradient approximation (GGA) [36].

In LDA, the exchange-correlation energy density at each point is the same as that of a homogeneous electron gas of the same density:

$$E_{XC}^{LDA} = \int d\mathbf{r} n(\mathbf{r}) \epsilon_{XC}(n(\mathbf{r})) \tag{2.14}$$

where $\epsilon_{XC}(n(\mathbf{r}))$ is the exchange-correlation energy per particle of a homogeneous electron gas of density $n_0 = n(\mathbf{r})$. Several parameterizations for ϵ_{XC} exist, but the most commonly used is that of Perdew and Zunger [37]. The parameterization uses interpolation formulas to link these exact results for the exchange and correlation energy at many different densities. In LDA, corrections to the exchange-correlation energy due to the inhomogeneities in the electronic charge density about r is ignored. In spite of this, LDA works remarkably well in inhomogeneous electronic systems.

LDA fails in the situations where the density undergoes rapid changes such as in molecules. An improvement to this can be made by considering the gradient of the electron density, the so-called Generalized Gradient Approximation (GGA).

The exchange-correlation energy is expressed in terms of the gradient and spatial derivatives of the charge density as,

$$E_{XC}^{GGA} = \int d\mathbf{r} n(\mathbf{r}) \epsilon_{XC}(n(\mathbf{r}), \nabla n(\mathbf{r})). \tag{2.15}$$

This leads to a notable improvement over LDA results with accuracy approaching that of correlated wavefunction methods [38]. There are different parameterizations of the GGA, some of the commonly used approximations of exchange-correlations energy functional are the ones parameterized by Perdew and Wang (PW91) [39] and Perdew, Burke and Ernzerhof (PBE) [36].

2.2.4 Pseudopotentials

Another approximation in our DFT calculations is that of pseudopotentials. This is based upon the observation that the core electrons are relatively unaffected by the chemical environment of an atom. It is assumed that their (large) contribution to the total binding energy does not change when isolated atoms are brought together to form a molecule or a crystal. The actual energy differences of interest involve changes in the valence electron interaction and energies. If the binding energy of the core electrons can be subtracted out, the contribution of valence electrons is a much larger fraction of the total binding energy, and easier to calculate accurately. This is because a strong nuclear Coulomb potential and highly localized core electron wave-functions are difficult to represent numerically.

Since the atomic wave-functions are eigenstates of the atomic Hamiltonian, they are mutually orthogonal. Since the core states are localized in the vicinity of the nucleus, the valence states oscillate rapidly in the core region to maintain the orthogonality with wavefunctions of core electrons. Such rapid oscillations result in a large kinetic energy of valence electrons in the core region, which roughly cancels

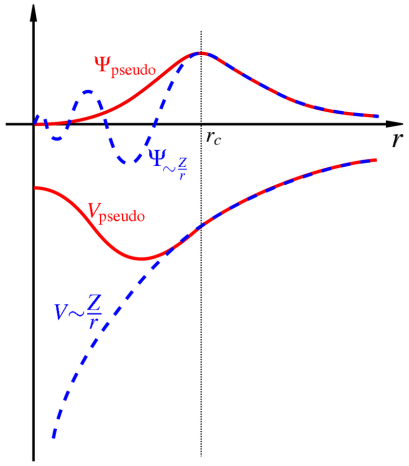

Figure 2.2: Schematic representation of an all electron potential (dotted line) and pseudopotential (solid line) along with corresponding wavefunctions.

the large potential energy due to the strong Coulomb potential.

It is therefore convenient to replace the strong Coulomb potential and core electrons with an effective pseudopotential, which is much weaker. This involves replacing the valence electron wave-functions, which oscillate rapidly in the core region, with pseudo-wave-functions, which vary smoothly in the core region (see Figure 2.2). The pseudopotential is constructed by considering a cut-off radius (r_c) such that the all electron and pseudo wavefunctions of valence electrons are the same beyond r_c (refer Figure 2.2). In the core region, the eigenvalues and scattering properties are conserved by pseudo wavefunctions. If the charge of each pseudo wavefunction is equal the charge of the actual wavefunction in the region r $< r_c$, the pseudopotential is known as norm-conserving pseudopotential [40]. This is generalized in ultrasoft pseudopotential [40], in which the total charge in the core is conserved with augmented charge density. Ultrasoft pseudopotentials reduce the computational cost significantly, while maintaining the accuracy and transferability.

2.2.5 Basis sets

There are three basic approaches to the calculate the Kohn-Shame wavefunctions in materials, which are equally accurate provided they are applied carefully and taken to comparable convergence. In Kohn-Sham formalism, the independent-particle wavefunctions are expanded using basis sets and these methods are classified based on their basis sets. The commonly used basis sets are plane waves, atomic orbitals and a combination of both known as mixed basis.

Plane wave basis is used widely due to their simplicity and absence of Pulley forces. Since plane wave are eigenfunctions of the Schrödinger equation with constant potential, they are the natural basis for description of band structure of many materials including sp-bonded metals and semiconductors. The Kohn-sham wavefunction in the plane basis can be expanded as,

$$\psi_i(\mathbf{r}) = \sum_{|G|} C_{i,(k+G)} e^{i(k+G).r}, \tag{2.16}$$

where G is the reciprocal lattice vector and k is Bloch wavevector at which Kohn-Sham equations are solved [41, 42]. This expansion is infinite and is truncated to make it computationally feasible. To truncate the set of G vectors, a kinetic energy cutoff is used. The number of reciprocal lattice vectors in the sum is limited by including all those vectors which satisfy the condition,

$$\frac{\hbar^2}{2m_e}|k+G|^2 \leq E_{cut}. \tag{2.17}$$

The cutoff energy (E_{cut}) is increased until the calculated energy converges.

Atomic orbital basis [43, 44] captures the essence of atomic-like features of wavefunctions of molecules and solids. Mixed basis is a more general basis where the atomic-like features are incorporated near the core, and smoothly varying (plane

waves) away from the nucleus [45]. We have used plane wave basis in all our calculations here.

2.2.6 Hybrid Functional

Hybrid functionals are a class of approximations to the exchange-correlation energy functional in density functional theory that include a portion of exact exchange from Hartree-Fock (HF) theory with exchange and correlation of DFT. The exact exchange energy functional is expressed in terms of the Kohn-Sham orbitals rather than the density. A hybrid functional [46], which include certain amount of Hatree-Fock exchange, has further improved the GGA results. This improvement apparently originates from the inclusion of non-dynamical correlations which effectively delocalize the GGA exchange hole. Efficient hybrid calculations of periodic solids are possible using Gaussian-type orbitals and periodic boundary conditions (PBC) [47, 48].

In this thesis, we have used Heyd-Scuseria-Ernzerhof (HSE) functional to calculate band gaps of $MoTe_2$ and MoS_2. The HSE exchange-correlation functional [46] uses an error function screened Coulomb potential (short ranged) to calculate the exchange portion of the energy in order to improve computational efficiency, especially for metallic systems. The form of screened Coulomb potential hybrid density functionals given by,

$$E_{XC}^{\omega PBEh} = aE_X^{HF,SR}(\omega) + (1-a)E_X^{PBE,SR}(\omega) + E_X^{PBE,LR}(\omega) + E_C^{PBE}, \qquad (2.18)$$

where a is the mixing parameter and ω is an adjustable parameter controlling the short-range interactions. Standard values of a=$\frac{1}{4}$ and ω =0.2 $\mathring{A}^{-1}$ (usually referred to as HSE06) have been shown to obtain good results for most of systems. The HSE exchange-correlation functional reduces to the PBE0 hybrid functional for ω

$= 0$. $E_X^{HF,SR}(\omega)$ is the short range HF exact exchange functional, $E_X^{PBE,SR}(\omega)$ and $E_X^{PBE,LR}(\omega)$ are the short and long range component of the PBE exchange functional, and $E_C^{PBE}(\omega)$ is the PBE [36] correlation functional. The most striking change due to use of the hybrid functional is in the predicted excitation energies or bandgaps.

2.2.7 GW Approximation

The Green function method is a suitable approach for studying excited state properties. To calculate the Green function one requires the self-energy operator which is non-local and energy dependent. The GW approximation is a simple and fruitful approximation to the self-energy. The Kohn-Sham eigenvalues ϵ_i have no clear physical meaning except for that of the highest occupied state. Although there is no theoretical justification, they are often interpreted as single-particle excitation energies corresponding to excitation spectra of the system upon a removal or addition of an electron. Single-particle excitation energies or quasiparticle energies [49, 50] can be calculated with the Green function formalism [51, 52]. Quasiparticle energies E_i are obtained from the quasiparticle equation:

$$\Big[-\frac{1}{2}\nabla^2(\mathbf{r}) + V_{Hatree}(\mathbf{r}) \Big] \psi_i(\mathbf{r}) + \int d^3\mathbf{r} \sum (\mathbf{r}, \mathbf{r}'; E_i) \psi_i(\mathbf{r}') = E_i \psi_i(\mathbf{r}) \qquad (2.19)$$

The non-local and energy dependent potential $\sum$, or the self-energy, contains the effects of exchange and correlations. It is in general complex with the imaginary part describing the damping of a quasiparticle. It can be seen that the different single-particle theories amount to approximating the self-energy operator $\sum$. Calculations of self-energy is unfortunately intensive even for the electron gas. The form of the self-energy in the GW Approximation (GWA) is the same as in the HF approximation (HFA) but the Coulomb interaction is dynamically screened, remedying the most serious deficiency of the HFA.

The GWA includes an important physical ingredient in extended systems, namely screening or polarization of the medium which is absent in the HFA. It is well known that the neglect of screening results in unphysical results for metals such as zero density of states at the Fermi level and in semiconductors and insulators to overestimated band gaps. Since screening is a common feature in all electronic systems, it is perhaps not surprising that the GWA works in a wide variety of materials.

Applications of a GWA to large and complex systems is still not quite feasible due to computational effort involved. Simplified GW schemes, which maintain the accuracy of full calculations and are computationally efficient, are therefore much desirable. Many schemes have been proposed but most of them are designed for semiconductors. While they give reliable band gaps, details of the band structure are not completely accounted for. Non-locality as well as energy dependence of the self-energy must be taken care in reliable schemes of calculations. With efficient schemes, many interesting problems can then be tackled such as chemisorption at surfaces, 3d impurities in semiconductors, interfaces, band off-sets in heterojunctions.

2.2.8 Dispersive interaction

GGA functionals including hybrid schemes have a general drawback that they can not describe long-range electron correlations that are responsible for van der Waals (vdW, dispersive) forces [53, 54] as they replace part of the local HF exchange by nonlocal HF exchange. The vdW interactions between atoms and molecules play an important role in many chemical problems [55]. In recent years, to include these dispersive interactions in DFT calculations, several methods have been developed. These interactions are divided into two classes, (1) treatment of dispersion interaction as semi-empirical corrections on top of existing local functionals, and (2) to develop non-local exchange-correlation energy functionals that can incorporate the

London interactions [56,57]. To account for such weak interactions between layers of materials such as $MoTe_2$, WTe_2, we have used parametrized DFT-D2 scheme (class 1) of Grimme [56]. This gives a fairly accurate treatment of London dispersion interactions at relatively low computational cost, and we briefly describe the formulation below. The total energy with dispersion correction is given as,

$$E_{DFT-D2} = E_{KS-DFT} + E_{disp} \tag{2.20}$$

where E_{KS-DFT} is the self-consistent Kohn-Sham energy and E_{disp} is the an empirical dispersion correction given as,

$$E_{disp} = -s_6 \sum_{i=1}^{N_{at}-1} \sum_{j=i+1}^{N_{at}} \frac{C_6^{ij}}{R_{ij}^6} f_{dmp}(R_{ij}) \tag{2.21}$$

Here, N_{at} is the number of atoms in the system, C_6 denotes the dispersion coefficient for atom pair (i, j), s_6 is a global scaling factor that depends only on the approximate functional used in KS-DFT, and R_{ij} is an interatomic distance. In order to avoid near-singularities at small R, a damping function f_{dmp} must is used:

$$f_{dmp}(R_{ij}) = \frac{1}{1 + e^{-d(R_{ij}/R_r - 1)}} \tag{2.22}$$

Here, R_r is the sum of atomic van der Waals radii and the parameter d determines the dispersion corrections to the total energy and is fixed to 20 by Grimme to give accurate dispersion energies, but still maintaining negligible energies for typical covalent bonding situations. The dispersion coefficient C_6^{ij} for a given pair of atoms i and j, is taken as a geometric mean of the individual coefficients,

$$C_6^{ij} = \sqrt{C_6^i C_6^j}. \tag{2.23}$$

2.3 Calculation of Phonons

Phonon, a quantum of vibration energy that arises from oscillating atoms within the crystals. With Born-Oppenheimer approximation, the electrons remain in their ground state, and hence the total energy is only function of ionic positions, E($\{\mathbf{R}_I\}$). There are mainly two approaches for the calculation of phonons from first-principles: (1) Direct calculation of total energy as a function of the positions of the atoms (frozen-phonon method) (2) Perturbative approach involving calculations of the second derivatives of energy (response function method) with respect to atomic positions.

2.3.1 Frozen phonons

In the frozen phonon method, a small, a finite perturbation (atomic displacement) is frozen in the system, and the total energy and forces are calculated. The forces on atoms are calculated within the framework of density functional theory, making it a direct approach for phonon calculations. The potential energy of the system on Taylor expansion is

$$V = V_0 + \sum_{I,\alpha} \frac{\partial E}{\partial \mathbf{R}_{I,\alpha}}\Big|_{u=0} u_{I\alpha} + \frac{1}{2} \sum_{I,J,\alpha,\beta} \frac{\partial^2 E}{\partial \mathbf{R}_{I,\alpha} \partial \mathbf{R}_{J,\beta}}\Big|_{u=0} u_{I\alpha} u_{J\beta} + O(u^3). \qquad (2.24)$$

where, $\mathbf{R}_I = \mathbf{R}_I^0 + u_I$, $\mathbf{R}_I^0$ is the equilibrium position of the I^{th} ion and u_I is displacement of the atom. The second term of the equation is equal to zero as all the ions are placed in their equilibrium position. Ignoring the constant term (V_0) and $O(u^3)$, focusing on the quadratic terms, the force constant matrix $K_{IJ,\alpha\beta}$ is given

by,

$$\begin{aligned} V &= \frac{1}{2} \sum_{I,J,\alpha,\beta} \frac{\partial^2 E}{\partial \mathbf{R}_{I,\alpha} \partial \mathbf{R}_{J,\beta}}\Big|_{u=0} u_{I\alpha} u_{J\beta}, \\ &= \frac{1}{2} \sum_{I,J,\alpha,\beta} K_{I\alpha,J\beta} u_{I\alpha} u_{J\beta}. \end{aligned} \tag{2.25}$$

Solving the equation of motion for harmonic oscillator we get,

$$M_I \frac{\partial^2 u_{I\alpha}}{\partial t^2} = -\sum_{J,\beta} K_{I\alpha,J\beta} u_{J\beta}. \tag{2.26}$$

$u_I\alpha$ has time dependence as follows

$$u_I(t) = \hat{u}_I e^{i\omega t} \tag{2.27}$$

and from equation,

$$\omega^2 M_I \hat{u}_{I\alpha} = \sum_{J,\beta} K_{I\alpha,J\beta} \hat{u}_{J\beta}. \tag{2.28}$$

We can get frequencies (ω) and eigenvectors ($\hat{u}$) of phonons by solving the above eigenvalue (ω^2) equation. There are 3N number of modes and dimension of force constant matrix is $3N \times 3N$ for a given N atom system. The local structural stability of a crystal is determined with the value of phonon frequencies. If $\omega^2 > 0$, the system is stable *i.e.* the excitation of any phonon mode with frequency ω increases the energy of the system. For a unstable system, $\omega^2 < 0$ *i.e.* finite amplitude of certain phonon modes results in lowering of total energy of the system.

However, this technique can determine the full phonon dispersion of a crystal only with use of large "supercells" in calculations, whose size depends on the wavelength of perturbation. Thus it increases the computational cost of phonon calculations at non-zero **q**-points. Density functional perturbation theory is a technique which overcomes this drawback of frozen phonon method.

2.3.2 Density Functional Perturbation Theory

Many physical properties of a system depend upon its response to some form of external perturbation. The response functions are first, second and third derivative of the total energy with respect to external perturbation, λ. Some of the physical properties of interest include polarizabilities, phonons, forces, stresses, Born effective charges, elastic constant, Raman intensities and cross-sections.

A linear response technique used to calculate second derivatives of the ground state energy w.r.t. external perturbation (λ_i) is known as density functional perturbation theory (DFPT). The first and second derivatives of ground state energy are given as,

$$\begin{aligned} \frac{\partial E}{\partial \lambda_i} &= \frac{\partial E_{ion-ion}}{\partial \lambda_i} + \int d\mathbf{r} \frac{\partial V_{ext}(\mathbf{r})}{\partial \lambda_i} n(\mathbf{r}), \\ \frac{\partial^2 E}{\partial \lambda_i \lambda_j} &= \frac{\partial^2 E_{ion-ion}}{\partial \lambda_i \lambda_i} + \int d\mathbf{r} \frac{\partial^2 V_{ext}(\mathbf{r})}{\partial \lambda_i \lambda_i} n(\mathbf{r}) + \int d\mathbf{r} \frac{\partial n(\mathbf{r})}{\partial \lambda_i} \frac{\partial V_{ext}(\mathbf{r})}{\partial \lambda_j} \end{aligned} \tag{2.29}$$

The electron density response $\partial n(\mathbf{r})/\partial \lambda_j$ is obtained by linearizing Eq. 2.12 as,

$$\Delta n(\mathbf{r}) = 2Re \sum_{i}^{N_e/2} \psi_i^*(\mathbf{r}) \Delta \psi_i(\mathbf{r}). \tag{2.30}$$

Within the linear response, $\Delta n(\mathbf{r}) = \partial n(\mathbf{r})/\partial \lambda_j$. The variation in the wavefunction can be obtained by solving standard first-order perturbation theory:

$$(H_{KS} - \epsilon_i)|\Delta \psi_i\rangle = -(\Delta V_{KS} - \Delta \epsilon_i)|\psi_i\rangle, \tag{2.31}$$

here, ΔV_{KS} and $\Delta \epsilon_i$ are first order variations of Kohn-Sham effective potential and

eigenvalues respectively.

$$\begin{aligned} \Delta V_{KS}(\mathbf{r}) &= \Delta V_{ext}(\mathbf{r}) + e^2 \int d\mathbf{r}' \frac{\Delta n(\mathbf{r}')}{|\mathbf{r}-\mathbf{r}'|} + \int d\mathbf{r}' \frac{\partial^2 V_{XC}}{\partial n(\mathbf{r}) \partial n(\mathbf{r}')} \Delta n(\mathbf{r}'); \\ \Delta\epsilon_i &= \langle\psi_i|\Delta V_{KS}|\psi_i\rangle. \end{aligned} \tag{2.32}$$

$\Delta\psi_i$'s can be projected onto empty states as the electron density responds to only those perturbations that couple both the occupied and empty states:

$$(H_{KS} - \epsilon_i)|\Delta\psi_i\rangle = -\hat{P}_{empty}\Delta V_{KS}|\psi_i\rangle, \tag{2.33}$$

where $\hat{P}_{empty}$ is the projection onto the empty states manifold defined in terms of occupied states ($\hat{P}_{occ}$) given by,

$$\hat{P}_{empty} = 1 - \hat{P}_{occ}; \hat{P}_{occ} = \sum_{i=1}^{N_e/2} |\psi_i\rangle\langle\psi_i|. \tag{2.34}$$

By solving this set of linear equations, one can calculate the relevant response properties of the system efficiently and with reasonable accuracy.

An advantage of DFPT with respect to the frozen-phonon technique is that the linear response to a monochromatic phonon perturbation is also monochromatic with the same wave-vector q. This is a consequence of the linearity of DFPT equations with respect to the perturbing potential. The calculation of the dynamical matrix can thus be performed for any q-vector without introducing supercells: the dependence on q factors out and all the calculations can be performed with lattice-periodic functions.

Part I

2D Hexagonal Boron Nitride

Chapter 3

Grain boundaries in 2D h-BN: structural instabilities and wrinkles*

3.1 Introduction

Fascinating properties of 0-D, 1-D and 2-D nano-forms of carbon have generated immense activity of research in the last two decades [58–60]. Among these, graphene (the 2-D form) is the mother form, which gives rise to other nano-forms through deformation or introduction of structural point defects (involving pentagonal carbon rings). Of late, there have been efforts to develop 3-D *nano*-structured forms of carbon that would open up new domains of applications [61, 62]. To this end, understanding of the structure of interfaces or extended line defects in graphene is expected to be crucial. While 2-D h-BN is the only other known material which is isostructural to graphene (almost lattice matched!), it exhibits rather different

*This work has been published in *Phys. Chem. Chem. Phys.*, 2014 [3]. Reproduced by permission of Royal Society of Chemistry, URL: $http://dx.doi.org/10.1039/C4CP0226$.

structural defects [63]. As a result, a solid solution, $C_x(BN)_{1-x}$ (CBN) between h-BN and graphene is promising in the development and engineering of 3-D materials with nano-scale architecture based on h-BN and graphene [64].

To develop such 3-D nano-forms of CBN, it is important to understand the interfaces or GBs in h-BN and graphene on the same footing. Such interfaces are analogous to GBs (well known in the context of 3-D crystalline materials), as they determine the way in which two flakes (grains) of 2-D materials are stitched together through non-hexagonal structural units (*e.g.* pentagon and heptagon pair [65]). In this work, we use the terms 'interfaces' and 'line defects' to broadly represent GBs.

Line and point defects invariably occur during the synthesis of these materials. They alter the local structural symmetry and can have interesting effects on their global properties, such as band gaps of h-BN [66]. Graphene and h-BN can be synthesized *via* different techniques such as chemical vapor deposition (CVD), chemical exfoliation, and electrochemical reduction [67–72]. The presence of point defects [28,73,74] and line defects [30,74,75] in h-BN and graphene is clearly evident in detailed characterization based on transmission electron microscopy (TEM) and scanning tunneling microscopy (STM). Notable changes in electronic, [33,76–81] mechanical, [82, 83] chemical [84] and magnetic [85] properties of graphene have been reported due to such structural changes at the GBs, though only a few reports are available on the analysis of GBs in h-BN and their effects on its electronic [86] and magnetic [87] properties.

Liu *et al.* [87] have discussed dislocations and GBs in monolayered h-BN, analysing square-octagon and pentagon-heptagon pair dislocations and transformation reaction of GBs for the tilt angle varying from $0\,^\circ$ to $240\,^\circ$. Their work focused on relative stability and electronic properties of these GBs. Li *et al.* [66] have studied 'B_2, N_2 and C_2 pentagon-octagon-pentagon (5-8-5)' line defects in 2D h-BN, and explained electronic and magnetic properties associated with these defects in h-BN. While the

structural instabilities are associated with Stone-Wales point defects [76] and line defects [88–90] are known to give rise to buckling of the structure of graphene, analysis of the structural instabilities associated with GBs or line defects in 2D h-BN is lacking. Though Raman spectroscopic characterization of defects in graphene has been quite effective, it lacks the specificity with respect to the kind of defects which requires the identification of specific vibrational signatures (if any) of GBs. It is thus desirable to study structural stability and spectroscopic properties of GBs in monolayer h-BN and graphene in detail.

We present here a detailed structural analysis of extended line defects or GBs in h-BN and graphene benefiting from the ideas of growth and stacking faults that are well established in metallurgy. This is expected to help understand how these GB structures may form during growth of these materials in experiments. The defect structures discussed in this article are essentially 60° GBs [90, 91] and inversion domain boundaries [92].

We identify the signatures of these GBs in the electronic and vibrational spectra. Our comparative analysis based on first-principles density functional theoretical (DFT) calculations provide a unified understanding of the interfaces or GB structures in h-BN and graphene. Our systematic scheme for the construction of GBs in these 2-D materials allows us to predict novel low energy interfaces. From their energetics, we assess the relative stability of various GBs in these materials, and understand it in terms of the changes in bonding. The structural instabilities and buckling (ripples and wrinkles) of planar structures associated with these GBs are analysed through a detailed study of their vibrational spectra. The spectroscopic signatures identified here would permit non-invasive characterization of such interfaces using Raman and IR spectroscopies.

3.2 Computational Methods

Our first-principles simulations are within the framework of density functional theory (DFT) as implemented in QUANTUM ESPRESSO (QE) package, [41] which employs plane wave basis and pseudopotentials. We use a generalized gradient approximation (GGA) of the Perdew, Burke and Ernzerhof (PBE) [36] form of the exchange correlation energy functional and ultrasoft pseudopotentials [40] to represent the interaction between ionic cores and valence electrons. The plane wave basis for representation of Kohn-Sham wavefunctions and charge density has been truncated with energy cutoffs of 30 Ry and 180 Ry respectively. We aided the convergence to self-consistency by smearing the occupation numbers with the Fermi-Dirac distribution function, with the smearing width of 0.003 Ry. Structures have been relaxed through the minimization of energy using Broyden-Fletcher-Goldfarb-Shenno (BFGS) scheme, until magnitude of each component of Hellman-Feynman force is smaller than 0.001 Ry/bohr. We use a periodic supercell to model 2-D h-BN (monolayer) and graphene. In order to ensure negligible interaction between the nearest periodic images of the 2-D sheet, a vacuum of 15 Å is introduced along c-axis. Integrations over the Brillouin zone are sampled with a 4x3x1 uniform mesh of k-points for a 3x4 supercell (rectangular supercell with 96 atoms, where unit cell consist of 8 atoms) and a 2x6x1 mesh for a 7x2 (rectangular supercell with 104 atoms, where unit cell consists of 8 atoms) supercell for 4:8 and 5:5:8 GBs respectively. Vibrational spectrum at the zone center Γ-point is determined using the frozen-phonon method with finite difference formulae and atomic displacements of ± 0.04 Å.

To assess relative stability of GBs, we define their energy per unit length as:

$$E_{GB} = \frac{E^{GB}_{BN/g} - N \times E_{bulk}}{l} \tag{3.1}$$

where, $E^{GB}_{BN/g}$ is the total energy of h-BN or graphene supercell with a GB, E_{bulk}

is the total energy of a primitive cell of h-BN or graphene, and N is the number of B-N or C-C atomic pairs in the supercell, and l is the length of a GB contained within supercell.

3.3 Structure and Energetics

In this section, we present detailed atomic structure of interfaces in 2-D lattices. There are many ways to construct interfaces [33, 66, 86, 87] which are classified into two types: (i) a stacking fault, in which a semi-infinite half of the 2-D lattice is in misregistry with the other half, and (ii) a growth fault, which is associated with removal of a line of atoms (missed during the growth of the lattice), as reported earlier for graphene [33]. They are essentially the inversion domain boundaries and 60 ° GBs. The construction of their structure in h-BN and graphene, is discussed below.

3.3.1 Stacking fault

A pure h-BN lattice with armchair edges along $\vec{a}$ or $\hat{x}$ is divided into two semi-infinite sheets by a slip line (see Figure 3.1a) parallel to $\vec{a}$. A misregistry (or slip) vector, $\vec{v} = 1.5b\hat{x}$ (where, b = bond length) gives a displacement of the upper half of the sheet with respect to the lower half. With introduction of this fault, the neighbouring atoms across the GB form homopolar (B-B and N-N) bonds, which are chemically and energetically not favourable (Figure 3.1b). Hence, a 180° rotation of the upper half lattice around the y-axis ('twist') (Figure 3.1c) is performed, so that the bonds across the GB line are heteropolar (B-N) and energetically more favourable. [93] As a result, a pair of one rectangular (B-N-B-N) ring and one octagonal ring forms, and this structure is labelled as a '4:8' GB. Because of the periodic boundary conditions, two such 4:8 GBs are generated, one at the center of the periodic supercell and

another at its edge. Recently, a similar GB has been reported theoretically, [87] in which 4:8 GB is created when two asymmetrical grains join with tilt angles of 0 °, 120 ° and 240 °. However, the resulting atomistic structural changes at the

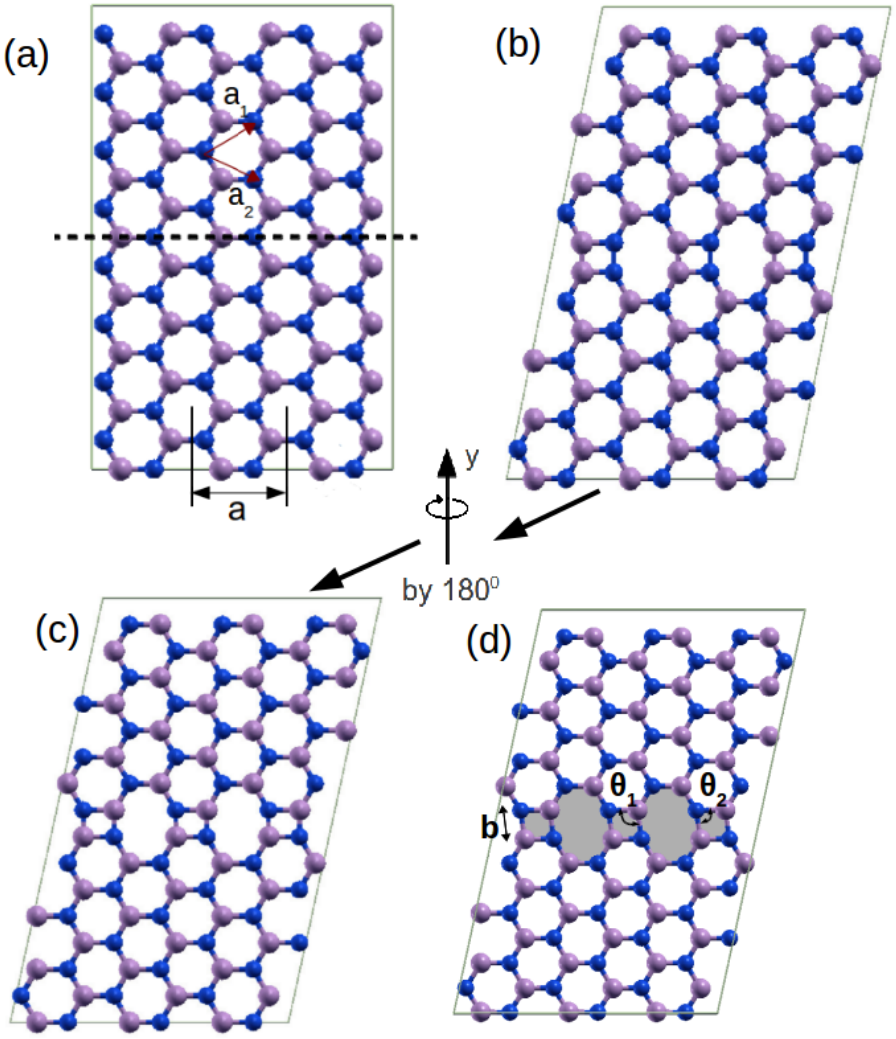

Figure 3.1: Construction of 4:8 GB in h-BN (a) Pure BN lattice (pristine) (b) BN lattice with stacking fault (c) BN lattice with GB twisting and (d) Ground state structure of BN with 4:8 GB (grey shadow shows the GB with octagons and rhombii). The bond length (b) and angles ∠NBN (θ_1) and ∠ BNB (θ_2) are 1.45Å, 98 ° and 82 ° respectively after relaxation. Boron (B) atoms are shown in pink and nitrogen (N) in blue.

GB have not been discussed. We present a detailed account of how its structure and energetics evolve upon relaxation. We find that the structure at the interface

evolves to interlinked rhombal and irregular octagonal rings, whose opposite sides are equal. The B-N bonds elongate from 1.44 Å (bulk h-BN) to 1.46 Å (perpendicular to GB). The bond angles θ_1 and θ_2 of rhombii are 82° and 98° respectively as shown in Figure 3.1d. The stress on the system is zero (after complete structural relaxation) for a defect concentration of 0.2/Å (no. of GB per supercell/distance between two GBs). Stretching of bonds perpendicular to the GBs causes a slight compression of hexagonal rings in the perfect honeycomb region connecting two GBs. The calculated energy of the 4:8 GB is 0.48 eV/Å, in good agreement with earlier estimates (0.4-0.5 eV/Å [87]).

Similarly, the 4:8 GB in graphene is introduced with a misregistry vector $\vec{v} = 1.5b\hat{x}$, which has energy of 0.74 eV/Å for defect concentration of 0.2/Å. Upon structural relaxation, we find that bond angles θ_1 and θ_2 are of 90° but the C-C bond perpendicular to the GB weakens from 1.42 Å (in pristine graphene) to 1.47 Å. As a result, we get interlinked rectangular and irregular octagonal rings at the interface. The 4:8 GB is more stable in h-BN than in graphene because the hetero-elemental sub-lattices facilitate formation of stable bonds at the interface (which comes from the twist of a grain) in contrast to those in graphene.

3.3.2 Growth fault

In construction of a growth fault, we consider two grains of a pure h-BN lattice obtained by cutting across a dashed line along zigzag direction as shown in Figure 3.2a, where grains or flakes are marked as 1 and 2.

The two grains are anti-symmetric across the dashed line. In grain 2, each B atom is replaced by N atom and N atom is replaced by B atom, such that a symmetric grains with the same polar edges facing each other (Figure 3.2b). To introduce a growth fault, we (i) move grain 1 along x-direction such that boron atoms at the edges of the two grains overlap along the dashed line, and (ii) remove one set of

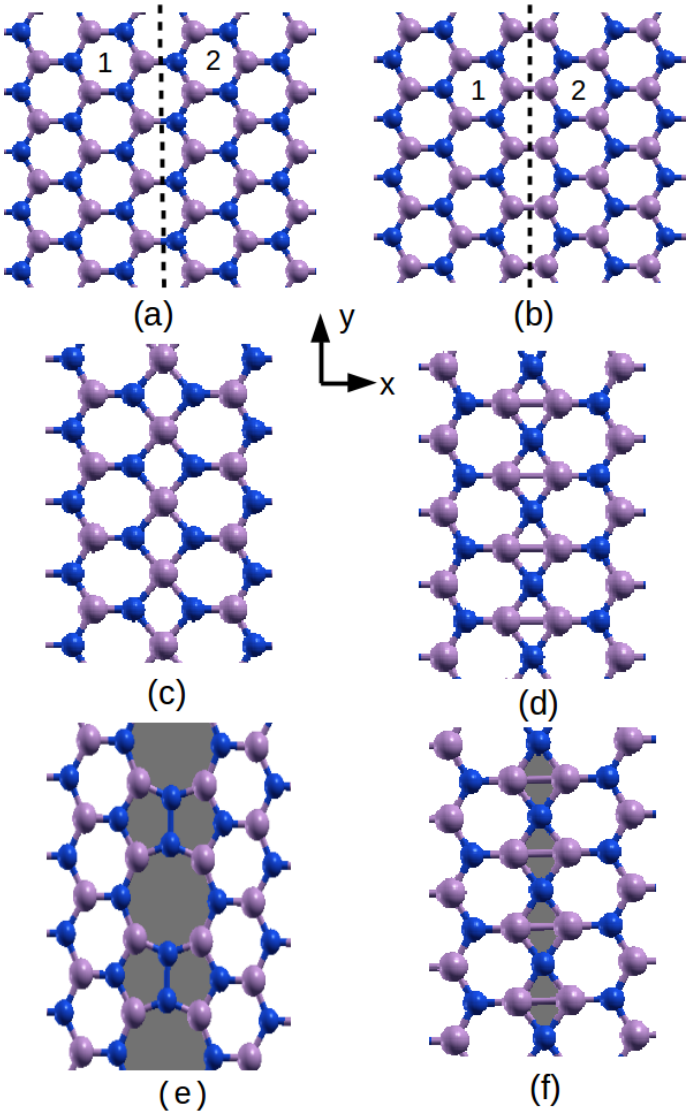

Figure 3.2: Construction of growth fault in h-BN (a) Pure BN lattice (pristine) which can be thought as two grains are connected perfectly along the dashed line (symmetrical grain boundaries with opposite polarity grains). Grain 1 and grain 2 are marked by 1 and 2. (b) Grain 2 is rotated by 180° along z-axis (tilt) with respect to grain 1 such that B-B bond forms perpendicular to dashed line (symmetrical grain boundaries with same polarity grains). (c) Grain 1 is moved along x-direction such that boron atoms perpendicular to dashed line overlap with each other (one layer of boron atoms is removed). A defect created at the GBs before relaxation (at the center of supercell) (d) Chain of rhombii, GB generated at the edge of the supercell (before relaxation). GBs are marked in shadow in (e) and (f), which show structural modifications after relaxation. Boron (B) atoms are shown in pink and nitrogen (N) in blue.

boron atoms on this line. This results in a linear chain of rhombii (Figure 3.2c) at the interface with B atoms occupying sites at the GB. We ensure equal number of B and N atoms in the supercell, by removing a line of N atoms from the edge of the supercell. Because of the periodic boundary conditions, another GB is thus generated at the boundary of the supercell involving a chain of rhombii with N atoms occupying sites at the GB (Figure 3.2d). The relaxation of this structure leads to the formation of a pair of two irregular pentagonal rings with apex angles of 111 ° and one irregular octagonal (with opposite sides of equal length) rings at the GB (Figure 3.2e). Thus, we label this as a '5:5:8' GB.

The interfaces with N-N and B-B bonds along the GB will be referred to as '5:5:8 N-N' and '5:5:8 B-B' GBs respectively. While the GB at the edge of the supercell is naively expected to transform into a 5:5:8 B-B GB, it retains its initial structure with rhombii (Figure 3.2f), confirming the feasibility of its occurrence in h-BN at 0 K. We label this GB constituted purely of rhombii as a '4:4' GB. This GB transforms into 5:5:8 B-B GB at 1000 K as discussed theoretically by X. Li *et al.* [66]. Along the line of 4:4 GB at the boundary, N-atoms are coordinated with four B-atoms saturating all its valence electrons (energetically favourable), in contrast to B-atoms coordinated with four N-atoms at the center of supercell. Hence, 4:4 GB with B atoms at GB transforms into N-N dimer along the GB (see Figure 3.2e). To determine energy of each of these GBs, we simulated BN ribbons containing these GBs at the center running along the length. From these simulations, the estimates of energies of the 5:5:8 N-N and 4:4 GBs in h-BN are 0.77 eV/Å and 1.87 eV/Å respectively. To determine energy of a 5:5:8 B-B GB, we interchange the B atoms and the N atoms in the 5:5:8 N-N structure. The calculated energy of the 5:5:8 B-B GB is 0.65 eV/Å, from which it is clear that the 5:5:8 B-B GB is more stable than the other two (5:5:8 N-N and 4:4) GBs in h-BN.

Similarly, a 5:5:8 GB can be created in graphene by the introduction of a growth

fault [33]. We have repeated the calculations of these GBs in graphene with the same type of supercell as h-BN to facilitate direct comparison of energetics. Similar to h-BN, there are two GBs: one at the edge and another at the center of the supercell (chain of rhombii). However, they evolve differently upon structural relaxation. The GB at the center of the graphene supercell evolves into a GB with a set of 2 irregular pentagonal rings with apex angles, 112 ° and an irregular octagonal ring (Figure 3.3a) *i.e.*, the 5:5:8 GB.

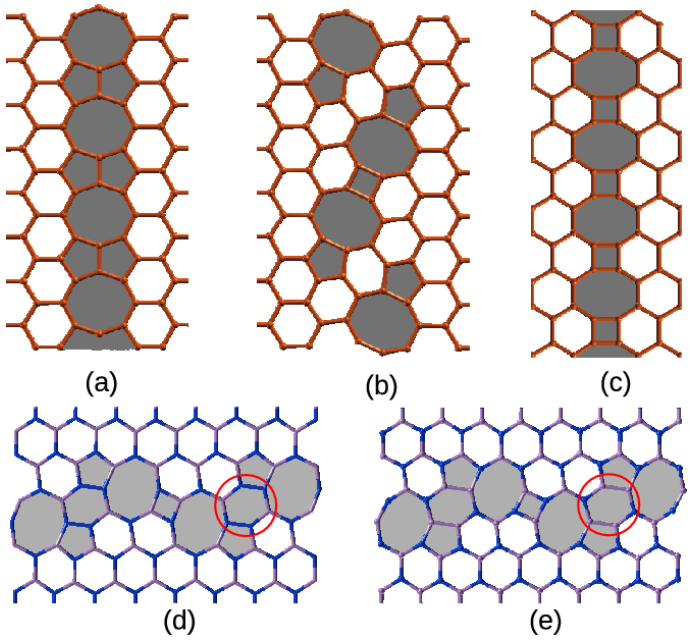

Figure 3.3: Different GBs in graphene and h-BN (a) Structure of 5:5:8 GB in graphene. (a chain of a set of 2 pentagon and octagon falls along the GB) (b) Structure of 6:5:8:4:8:5 GB in graphene (two set of one pentagon and octagon oriented oppositely are connected by a rectangle along the GB). (c) Structure of 4:8 GB in graphene (a chain of a set of 1 octagon and rectangle). (d) Structure of 6:5:8:4:8:5 N-N GB in h-BN (two set of one pentagon and octagon oppositely are connected by a rhombus along the GB). (e) Structure of 6:5:8:4:8:5 B-B GB in h-BN (two set of one pentagon and octagon oppositely are connected by a rhombus along the GB). Note that in 6:5:8:4:8:5 N-N and 6:5:8:4:8:5 B-B two set of 5-8-4-8-5 polygons are connected by a distorted hexagon whose opposite sides are B-B/N-N as highlighted in (d) and (e) by red circle. GBs are shown by shadows. Boron (B) atoms are shown in pink and nitrogen (N) in blue.

Interestingly at the boundary of the supercell, we find a new type of GB with

two oppositely oriented pentagon-octagon pairs linked with a rectangular ring (Figure 3.3b). This GB is named as the '6:5:8:4:8:5' GB, in which we get irregular pentagonal ring with apex angle 109 ° and irregular octagonal ring. The energies of 5:5:8 and 6:5:8:4:8:5 GBs (using simulations of ribbon) are 0.52 eV/Å and 0.73 eV/Å respectively (we note that these estimates of energies include the energy cost associated with dangling bonds formed at edge of ribbon). We find that the 5:5:8 GB is lower in energy than the 6:5:8:4:8:5 GB indicating its greater stability in graphene. Our analysis also shows that the 5:5:8 GB is more stable in graphene than h-BN (see Table 3.1). The reason for this is the extra energy required for the formation of homo-elemental bonds at the GB in h-BN. We explored the feasibility of 6:5:8:4:8:5 GB in h-BN and found two new types of GB structures (6:5:8:4:8:5 B-B and 6:5:8:4:8:5 N-N). The structures of these GBs involve a pair of pentagons and an octagon oppositely oriented, connected by a rhombus and two sets of 5-8-4-8-5 polygons that are connected by a deformed hexagon with B-B/N-N bonds at the opposite sides (see Figure 3.3d and e). The energies of 6:5:8:4:8:5 B-B and 6:5:8:4:8:5 N-N GBs are 0.79 eV/Å and 1.10 eV/Å respectively, comparable to energy of other interfaces.

3.3.3 Relative stability of faults or grain boundaries

We now discuss the relative stability of GBs in h-BN and graphene, by comparing the energies of the same GB in these materials. It is clear from our results (Table 3.1) that 4:8 GB (stacking fault) is more stable in h-BN (Figure 3.1d) than in graphene (Figure 3.3c), and it has the lowest energy, due to formation of the hetero-polar bond at the GB in h-BN. In contrast, a growth fault (5:5:8 GB) is the most stable GB in graphene with energy 0.52 eV/Å. Similarly, the 5:5:8 B-B GB (growth fault) is the most stable GB among all the growth faults in h-BN studied here. While studying growth and stacking faults in h-BN and graphene, we find four new GBs,

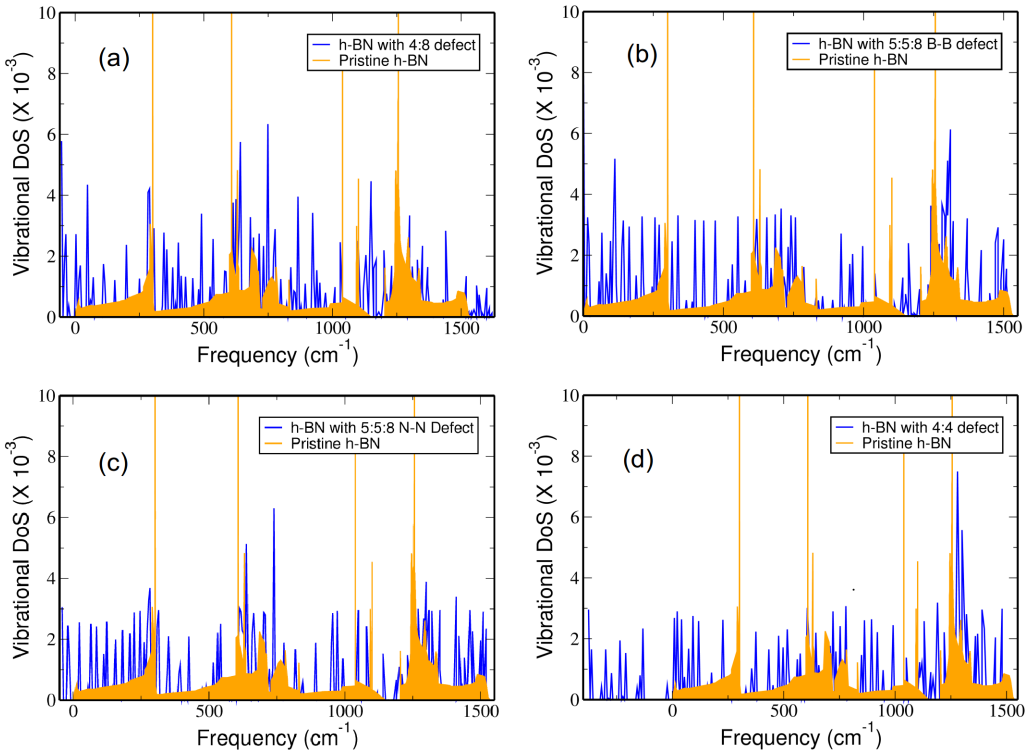

Figure 3.4: Vibrational density of states (Vdos) of perfect BN and BN with GBs. (a) Vdos of pristine and h-BN with 4:8 GB. (b) Vdos of pristine and h-BN with 5:5:8 B-B GB. (c) Vdos of pristine and h-BN with 5:5:8 N-N GB. (d) Vdos of pristine and h-BN with 4:4 GB. Light brown (orange) and blue denote the phonon density of states for pristine h-BN and h-BN with GB respectively.

which have not been reported yet. The 6:8:5:4:8:5 GB in graphene has an energy of 0.73 eV/Å, whereas 4:4, 6:8:5:4:8:5 B-B and 6:8:5:4:8:5 N-N GBs in h-BN have energies of 1.87 eV/Å, 0.79 eV/Å and 1.10 eV/Å respectively. The 6:8:5:4:8:5 GB is energetically more stable in graphene than in h-BN, and 6:8:5:4:8:5 B-B is more stable than the other two GBs in h-BN (6:8:5:4:8:5 B-B and 6:8:5:4:8:5 N-N). The 4:4 GB is relatively higher in energy than any other GB in h-BN, suggesting low likelihood of its occurrence.

Table 3.1: Energies for different grain boundaries (4:8, 5:5:8, 4:4 and 6:5:8:4:8:5 GBs) in h-BN and graphene

Type of GBs	System	Energy (eV/Å)
4:8	h-BN	0.48
4:8	graphene	0.74
5:5:8 N-N	h-BN	0.77
5:5:8 B-B	h-BN	0.65
4:4*	h-BN	1.87
6:5:8:4:8:5 N-N*	h-BN	1.10
6:5:8:4:8:5 B-B*	h-BN	0.79
5:5:8	graphene	0.52
6:5:8:4:8:5*	graphene	0.73

*novel GBs

3.4 Structural Instabilities

Structural stability can be affirmed by showing that the structure is a local minimum of energy w.r.t. all structural distortions. To this end, we determine long wavelength phonons of the supercell (at Γ-point). Vibrational density of states (Figure 3.4) of h-BN with 4:8, 4:4 and 5:5:8 N-N GBs, reveal the presence of unstable modes (*i.e.* imaginary frequencies), whereas 5:5:8 B-B does not have any unstable modes, implying the structure of h-BN with 5:5:8 B-B GB is stable, *i.e.* local minimum of energy. On the other hand, these unstable modes conclusively show that the structure is not a local minimum of energy, but is a saddle point. Eigen-modes of phonons with imaginary frequencies in the vibrational spectrum of defective h-BN involve atomic displacements that lead to out-of-plane deformation along these interfaces (see Figure 3.5a, b and Figure 3.6a, b).

We distort the structure by freezing in small atomic displacements corresponding to eigen modes of the lowest energy unstable modes (strongest instability) (which are 53 cm^{-1}, 375 cm^{-1} and 40 cm^{-1} for 4:8, 4:4 and 5:5:8 N-N GBs respectively).

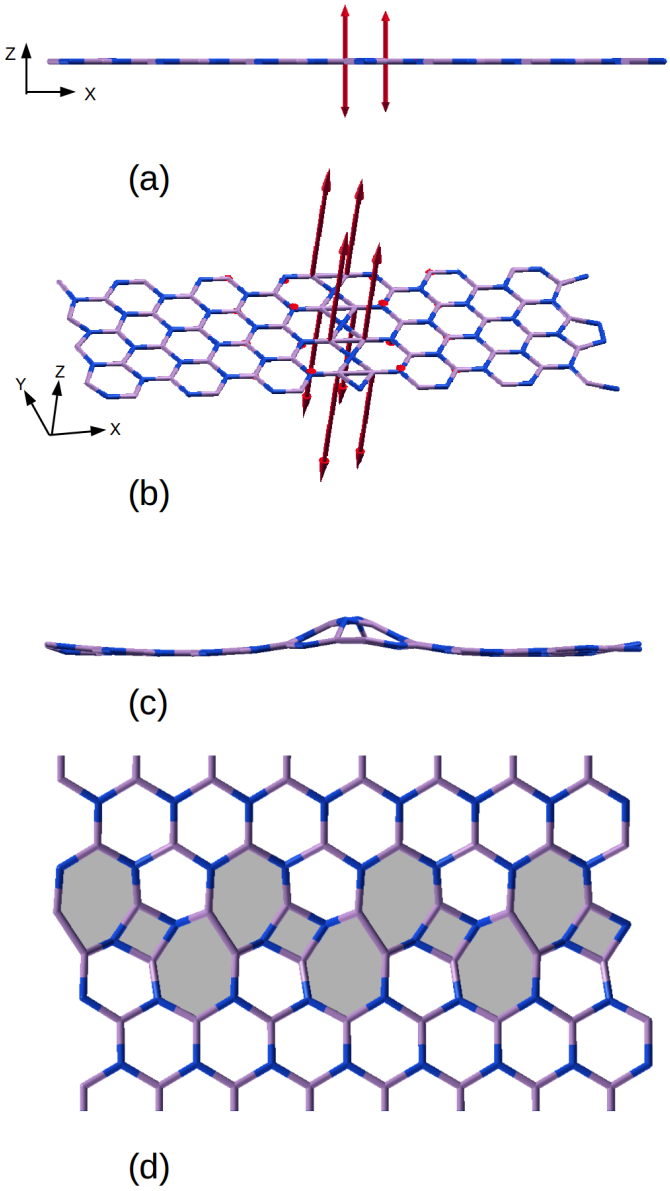

Figure 3.5: Phonon modes constituting the structural instability of h-BN with 4:4 GB (a), (b) Two views of atomic displacements of the mode with a frequency ≈375i cm^{-1} (wave like deformat ion at GB). (c) Freezing in the same mode leads to buckling of the sheet which is centered at GB (side view of the sheet). (d) Top view of 4:4 GB (which evolves on relaxation), which has two heptagons sharing a B-B bond side connected with a rhombus. Boron (B) atoms are shown in pink and nitrogen (N) in blue.

The unstable modes of 4:8 and 4:4 GBs have oscillatory deformation localized (like a wave) along the GB (Figure 3.5a, b and Figure 3.6a, b), whereas the unstable

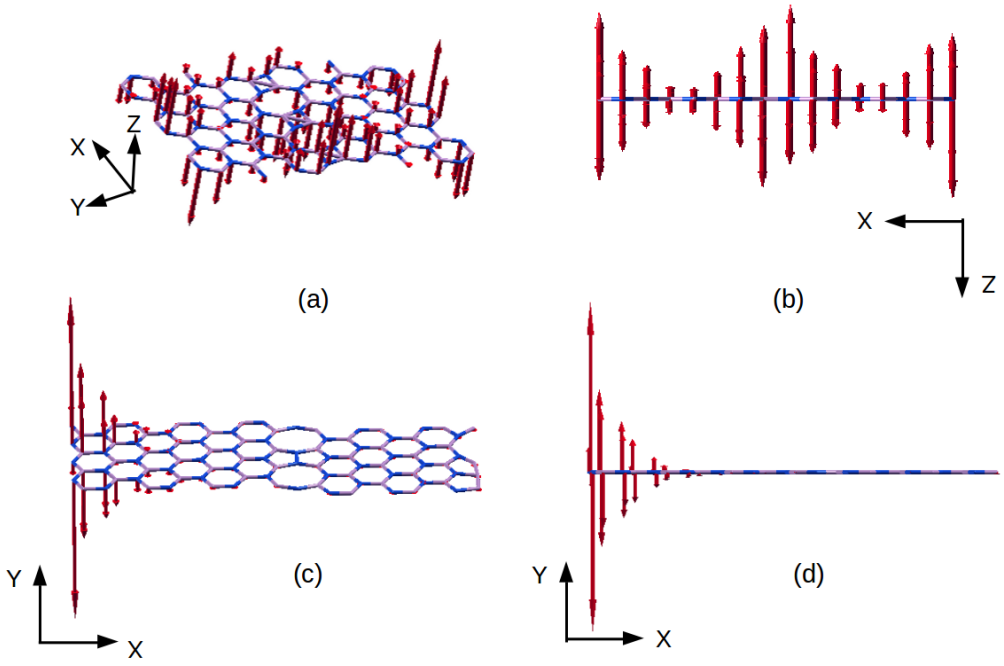

Figure 3.6: Phonon mode which constitutes the structural instability of h-BN with 4:8 GB, two views of atomic displacements of the mode with a frequency ≈53i cm^{-1} (wave propagates along th e GB) as shown (a) and (b). Phonon modes constitutes the structural instability of h-BN with 5:5:8 N-N GB, two views of atomic displacements of the mode with a frequency ≈40i cm^{-1} as shown in (c) and (d). Boron (B) atoms are shown in pink and nitrogen (N) in blue.

mode of 5:5:8 N-N has deformation wave running along the edge of the ribbon (not at the GB) (see Figure 3.6c and d).

In the 4:4 GB, N-atom is coordinated with four boron atoms through sp^3 bonding, hence it tries to deviate from planar to tetrahedral structure. A set of two B-atoms placed opposite to N atom tries to move in opposite direction to achieve tetrahedral structure (see Figure 3.5b). Upon structural relaxation, the h-BN sheet with these GBs buckle, *i.e.*, becomes non-planar. Such buckling of the sheet reduces the energy of 4:8 GB by 19.5%. For this GB, the rippling amplitude (the difference along the z-axis of the highest and lowest atom) is ∼ 0.35 Å, which is quite sizable and should be readily observable. There is not a considerable change in energy of 5:5:8 N-N GB due to buckling even though its rippled structure has an amplitude of 0.42

Å, suggesting a rather flat energy landscape of rippling. Structural relaxation of h-BN with a 4:4 GB after freezing in the displacements of lowest energy unstable mode, lowers its energy by 39.5%. The resulting structure exhibits a wrinkle (short length-scale deformation) at the interface (Figure 3.5b). Its structure (a chain of rhombii) evolves to a completely different structure (a chain of two heptagons and a rhombus). In this transformed structure, the two heptagons share a B-B bond as one of its sides (Figure 3.5d) and the rippling amplitude (1.6 Å) is quite significant. This deformation structure involving large displacement of most of the atoms at the GB constitute a wrinkle (see Figure 3.5c). Liu *et. al* [87] have studied similar defect as 4:8 GB, but missed the deviation from planarity of asym-0 ° (120 ° and 240 °) [87] GBs (4:8 GB in our case). In contrast we find that h-BN with a 4:8 GB does show buckling and there is noticeable reduction in energy by huge amount (19.5%).

3.5 Vibrational and Electronic Signatures

3.5.1 Vibrational signatures

The structural changes associated with these interfaces in h-BN are responsible for the changes in vibrational spectra, which can be identified in Raman and IR spectra. The unit cell of 2-D h-BN contains two atoms, and belongs to the point group D_{3h} and space group ($P\bar{6}2m$). Its optical phonon modes are categorized into $A_2'' + 2E'$ modes, where mode A_2'' is IR active and an E' mode is both IR and Raman active (E' is a doubly degenerate in-plane bond stretching mode) [94]. Our estimates of frequencies of A_2'' and E' modes are 791 cm^{-1} and 1382 cm^{-1} respectively, which agree well (within 1%) with experimental values reported earlier. [95] The frequency and eigen displacement of A_2'' and E' modes are modified by these interfaces, due to structural modifications at their GB. To identify A_2'' and E' modes of the h-BN supercell with a 4:8 GB, we project its normal modes (e'_ν) onto those of pristine

h-BN (e_μ), by calculating an overlap matrix ($S_{\mu\nu}$) given by,

$$S_{\mu\nu} = \langle e_\mu | e'_\nu \rangle \tag{3.2}$$

The A_2'' and E' modes of the defective h-BN are identified as those having the largest overlap ($|S_{\mu\nu}|$) with the A_2'' and E' eigenvectors of pristine h-BN.

Due to the GB, the symmetry equivalence between x and y directions in the hexagonal lattice is broken, and hence the degeneracy of E' mode is lifted. The A_2'' mode softens by 14 cm^{-1}, 10 cm^{-1} and 14 cm^{-1} due to 4:8 , 5:5:8 N-N and 4:4 GBs respectively (see Table 3.2). In presence of 5:5:8 B-B GB, the A_2'' mode hardens by 38 cm^{-1}. The E' mode softens by 21 cm^{-1} and 25 cm^{-1}, and hardens by 5 cm^{-1} and 10 cm^{-1} due to 5:5:8 N-N, 5:5:8 B-B, 4:8 and 4:4 GBs respectively for the vibration (in xy-plane) along the GB. The another in-plane E' mode softens by 26 cm^{-1} and 3 cm^{-1} (not significant) and hardens by 12 cm^{-1} and 106 cm^{-1} (significant) for 5:5:8 N-N, 4:4, 4:8 and 5:5:8 B-B GBs respectively for vibrations in the xy-plane involving displacements perpendicular to the GB (refer Table 3.2). Such shifts in frequencies can be observed experimentally with IR and Raman spectroscopies. The softening (hardening) of these modes is readily understood in terms of stretching (contraction) of the in-plane (out-of-plane) bonds.

3.5.2 Electronic signatures

We now identify electronic signatures of the lowest energy GB (4:8 GB) in h-BN through comparison with pristine h-BN. Its electronic density of states (DoS) reveals two extra peaks (Figure 3.7a) at the valence band maximum (VBM) and the conduction band minimum (CBM). Further analysis of the charge density of these states indicates that these electronic states are localized at the GBs, confirming

Table 3.2: Vibrational spectroscopic signatures in the Raman and IR active modes of h-BN with different GBs (4:8, 5:5:8, 4:4) and shifts in frequencies ($\Delta\omega$ in cm^{-1}) w.r.t. pristine h-BN.

Pristine (h-BN) (cm^{-1})	h-BN with 4:8 GB (cm^{-1})	h-BN with 5:5:8 B-B GB (cm^{-1})	h-BN with 5:5:8 N-N GB (cm^{-1})	h-BN with 4:4 GB (cm^{-1})
791 (IR active)	777 ($\Delta\omega$= -14)	829 ($\Delta\omega$= +38)	781 ($\Delta\omega$= -10)	778 ($\Delta\omega$= -14)
1382 (Raman and IR active)	1389 ($\Delta\omega$= +5)	1392 ($\Delta\omega$= +10)	1361 ($\Delta\omega$= -21)	1357 ($\Delta\omega$= -25)
1382 (Raman and IR active)	1394 ($\Delta\omega$= +12)	1379 ($\Delta\omega$= -3)	1356 ($\Delta\omega$= -26)	1488 ($\Delta\omega$= +106)

these extra peaks constitute characteristic signatures of the 4:8 GB. From the comparison of the electronic DoS of planar and non-planar GB structures, a few extra peaks are evident in the DoS of the non-planar structure, indicating a redistribution of localized electronic states upon buckling.

To facilitate experimental observations and verification, we obtain simulated scanning tunneling microscopy (STM) [96] images. They were obtained keeping the tip at a constant height of 1Å above the surface of h-BN with a positive sample bias of 0.8V with respect to the CBM. For a positive sample bias, induced charge accumulation is observed at B atoms whose orbitals constitute the conduction band. Simulated STM images (Figure 3.7c and d) highlight the difference between electronic structure of the planar and non-planar structures of the defective h-BN. We notice that the bright features in the bulk planar structure weaken upon buckling (clear from the STM image of the non-planar structure), showing that charge accumulation remains localized at the GB even after buckling.

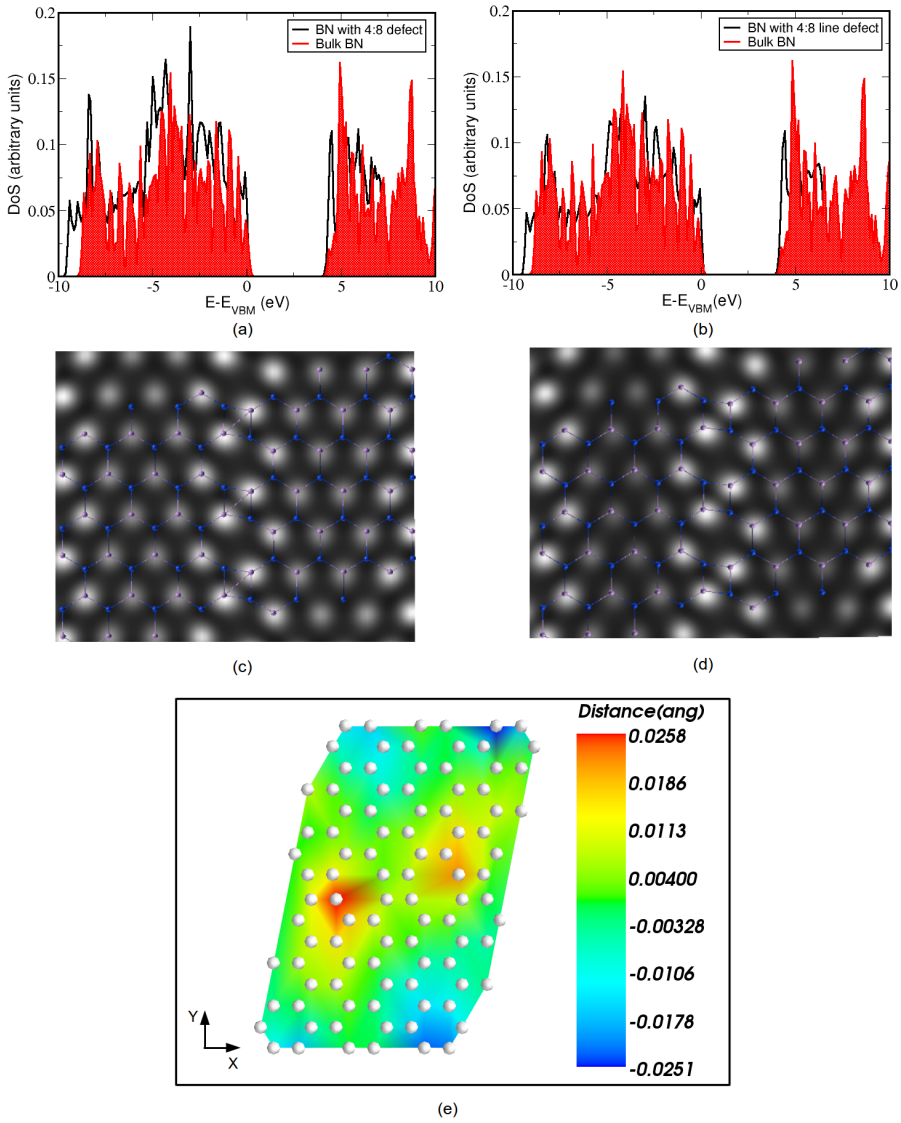

Figure 3.7: Electronic signature of 4:8 GB in h-BN seen in the density of states of (a) planar and (b) buckled (i.e. non-planar) structures (compared with pure h-BN). Atomic structures juxtaposed on simulated STM images of planar (c) and non-planar (d) h-BN with 4:8 GB. (g) Buckled h-BN sheet with different colors showing the extent to which different atoms displace out of plane.

3.6 Conclusions

We presented a comparative analysis of changes in the structure and vibrational properties associated with two types of interfaces categorized into: (i) stacking and (ii) growth faults in h-BN and graphene. We demonstrated that a 4:8 GB (stacking

fault) is more stable in h-BN, while a 5:5:8 GB (growth fault) is relatively more stable in graphene. We reported four new types of GBs: 6:5:8:4:8:5 GB in graphene and 4:4, 6:5:8:4:8:5 N-N and 6:5:8:4:8:5 B-B GBs in h-BN. The 6:5:8:4:8:5 GB in graphene, which is not reported so far, has the lowest energy among all the four GBs, and should therefore be common and relevant to experiment. Our work highlights the remarkable diversity in the structures of grain boundaries even when the angle between the grains is fixed at 60 °.

Furthermore, our analysis of the lattice dynamical (phonon) spectrum of the planar structure with these GBs (4:8, 5:5:8 N-N and 4:8) revealed unstable modes, *i.e.* structural instabilities with respect to buckling initiated at the interface. These lead to formation of wrinkles (short length scale buckling) at the interfaces and associated rippling (long length scale buckling) of the structure, which are relevant to the evolution of nano-forms to 3-D frameworks. Vibrational signatures identified here, specifically hardening and softening (frequency shifts) of A_2'' and E' modes, will be useful in characterization of these interfaces with IR and Raman spectroscopies. Electronic signature of the lowest energy 4:8 GB of h-BN is identified in the additional peaks at the VBM and the CBM that are associated with charge accumulation localized at the interface, and is accessible to STM.

Part II

Group VI Transition Metal Dichalcogenide

Chapter 4

1H and *1T* polymorphs, structural transitions and catalytic activity towards hydrogen evolution reaction

4.1 Polymorphs of 2-D Group VI TMDCs (Mo, W)(S, Se)$_2$*

4.1.1 Introduction

In recent years, there has been a renewed interest in Transition Metal (group *VI*) Dichalcogenides (TMDCs) due to their applications in varied areas such as lubrication [97,98], photocatalysis [99], field effect transistors [20], sensors [100] and battery cathodes [101–103]. TMDCs are layered materials with strong intra-layer and relatively weaker inter-layer bonding. With advances in synthesis techniques and device

*This work has been published in *2D Materials*, 2015 [4]. Reproduced with permission of Institute of Physics (IOP), URL: *http* : *//iopscience.iop.org*/2053 − 1583/2/3/035013.

fabrication, these structures can be exfoliated into 2-D monolayers from their bulk form. We follow the same nomenclature for polymorphs of monolayer MX_2 as used (*1H* and *1T*) in recent review on 2-D TMDCs by Chhowalla *et al.* [104]. Monolayers of these 2D-TMDCs (*e.g.* MoS_2, $MoSe_2$, WS_2 and WSe_2), in their most common *1H* structure, exhibit non-vanishing direct band gaps, and are suitable for applications such as transistors (with high on-off ratios [20]) photodetectors [105, 106], electroluminescent [107, 108] devices, electrode for Li-ion batteries [104] and supercapacitors [104].

Tunability of properties of a material is important to its applications, and the variation in its chemistry and structure are fundamental to such tunability. In the 2D-TMDCs, variety in cations (Mo, W) and anions (S, Se) can be effective in achieving some degree of tunability in their properties such as electronic band gap. Similarly, strain is known to alter their electronic properties [109–111]. A possibility of polymorphism involving variation in the stacking sequence of their atomic planes, can effectively modify electrical, thermal and mechanical properties without changing the chemistry and straining the lattice. Indeed, the *1T* structure was stabilized experimentally through Re substitution [112], and the atomic mechanism of *1H*-*1T* transformation was uncovered through a careful electron microscopy.

The *1H* structure consists of three X-M-X triangular planar atomic lattices, stacked in the *ABA* sequence. It effectively has a honeycomb lattice structure, with every alternate site occupied by a metal atom M, and the rest of the sites occupied by a pair of chalcogenide atoms X. The *1H* polymorphic [113] form of 2D-TMDCs exhibits a sizable band gap (*e.g.* 1.9 eV for MoS_2 [114]). In the *1T* polymorph of MX_2, the X-M-X triangular planar atomic lattices are stacked in the *ABC* sequence such that each M atom is octahedrally coordinated with six X atoms, and is at the centre of inversion. Monolayers of the centrosymmetric *1T* polymorph of TMDCs are metallic, and have been reported recently to show extraordinary

hydrogen evolution reaction activity (for *1T* MoS_2) [99, 115], with promise for a cost-effective replacement of platinum in hydrogen generation.

Recently, the $1T$ form of MoS_2 was predicted to be ferroelectric (broken inversion symmetry) with a semiconducting electronic band gap [5]. This is in contrast to the *1H* structure, which has a vanishing polarization in spite of its non-centrosymmetric structure due to other structural symmetries. The prediction of 2-D ferroelectricity in MoS_2 (and related monolayers) is striking because it is contraindicative due to effects of depolarizing fields which suppress the out-of-plane electric polarization. Its origin was traced to the strong electron-phonon coupling in MoS_2 associated with nesting of the Fermi surface of $1T$ polymorph. Based on this, Shirodkar *et al.* [5] proposed a novel class of *dipolectronic* devices, in which an electric field perpendicular to the layer is used to control the dipolar structure which influences the transport of carriers through the strong electron-phonon (dipole) coupling. Specifically, they proposed XNOR, NAND and OR logic gates within a single transistor structure. For such exciting technology and *dipolectronics* based on these TMDCs, it is very crucial to be able to synthesize them in the $1T$ polymorphic structure, and requires special considerations [116].

Lin *et al.* [112] have successfully triggered the *1H* to *1T* by accumulation of negative charge, and have studied the triggers and phases that act as precursors during this phase transformation. However, it is also important to understand the origin of their stability through determination of energetics and the precise structure of intermediate phases involved in it. For simple scheme of experimental characterization of these phases, it is desirable to obtain their spectroscopic signatures. At the fundamental level, the transitions between the polymorphic structures of MX_2 compounds are expected to result in anomalies in their response to external fields, which are yet to be identified.

In this paper, we determine the pathways in the configuration space of the monolayered MX_2 (M= Mo, W and X= S, Se) that connect the *1H* polymorph with the *1T* polymorph by estimating lowest energy barriers of their transformation. We also assess in detail the local stability and electronic structure of the *1H* and *1T* polymorphs, and provide the electronic and vibrational signatures that distinguish between the different polymorphs and the different compounds in group *VI* TMDCs. A deeper analysis of the switchability of ferroelectric polarization in the $1T$ structure [5] of these compounds is studied through their electronic structure and the stability of their dipolar domain structure. Finally, we uncover interesting anomalies in the response of semiconducting forms of MX_2 monolayers to electric field.

4.1.2 Methods

Our first-principles calculations are based on density functional theory as implemented in Quantum ESPRESSO package [41], and ultrasoft pseudopotentials [40] to model the interactions between valence electrons and ionic cores. The exchange-correlation energy of electrons is treated within a Generalized Gradient Approximation (GGA) functional as parametrized by Perdew, Burke and Ernzerhof (1996) [36] (use of LDA is known not to alter the results significantly for MoS_2 [5]). We use an energy cutoff of 35 Ry to truncate the plane wave basis used in representing Kohn-Sham wave functions, and an energy cutoff of 280 Ry to represent charge density. Structures are relaxed till the Hellman-Feynman force on each atom is less than 0.02 eV/Å. We have used a periodic supercell to simulate a 2D MX_2 sheet, with a vacuum of 10 Å to separate its adjacent periodic images. Integrations over the Brillouin Zone (BZ) are sampled on a 21x21x1 uniform mesh of k-points. We determine dynamical matrices and phonons at wavevectors on a 3x3x1 mesh in the BZ using DFT linear response (Quantum ESPRESSO implementation based on Green's function). From

these, dynamical matrices and phonons at arbitrary wave vectors are obtained using Fourier interpolation. For configurations of the 1T structure with $\sqrt{3}$x$\sqrt{3}$ and $\sqrt{3}$x1 periodic supercells, our self-consistent Kohn-Sham calculations are based on BZ sampling with 7x7x1 and 7x12x1 meshes of k-points respectively. The Raman cross-section of all the modes of the MX_2 compounds were calculated using second-order response as implemented in the Quantum ESPRESSO package [117] using norm-conserving pseudopotentials with the exchange correlation energy of electrons treated within the Local Density Approximation (LDA) functional as parametrized by Perdew-Zunger [37].

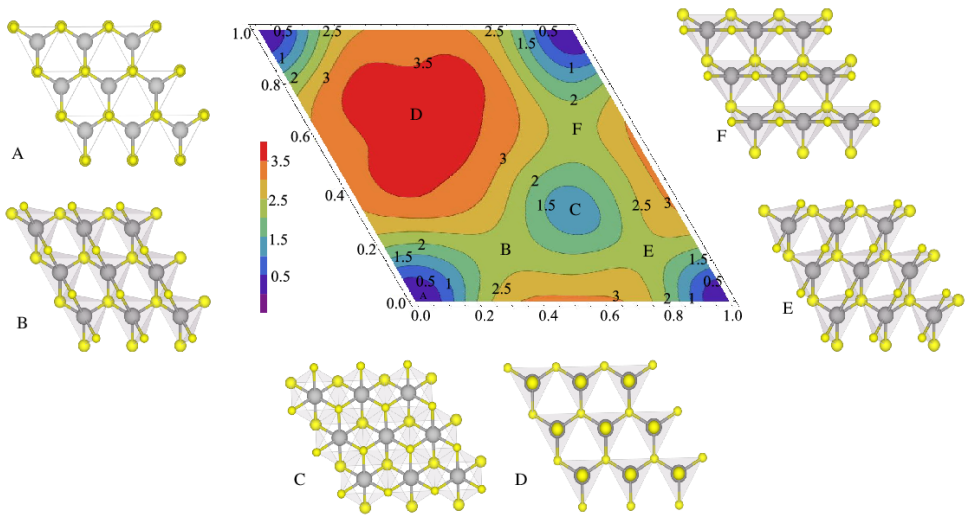

Figure 4.1: Contour plot of the γ-surface associated with glide of a Se-plane of $MoSe_2$ monolayer and top view of the structure at different configurations of γ-surface. Here, A is *1H* polymorph, B, E, F are symmetry equivalent transition states, C is the structure of c*1T* polymorph and D is the structure at highest point at energy surface (where Se-atom is sitting on the top of Mo-atom) of $MoSe_2$ structure . Se-atoms are denoted by yellow (small) spheres and Mo-atoms by grey (large) spheres. To distinguish between two Se planes, the top Se atoms are shown with circles of smaller radii than the bottom ones.

4.1.3 Paths of transition from *1H* to *1T* structure

Energy landscape

To determine the energy landscape for a transformation between *1H* and *1T* polymorphs, we consider different configurations obtained by displacing (or sliding) one of the X-atomic sublattice planes (e.g. top layer, X_{top}) with respect to the M-atom layer of the *1H* structure. This slip or the glide is a vector ($\vec{d}$) in the plane of the 2D MX_2:

$$\vec{d} = x\vec{a} + y\vec{b}, \tag{4.1}$$

where $\vec{a}$ and $\vec{b}$ are the unit cell vectors, and the atomic planes of metal and other X-atom are kept fixed. We consider x and y $\in$ [0,1), as the points on a 6x6 mesh in the unit cell of real-space lattice in fractional coordinates. The chalcogen atoms (X) are allowed to relax only in the direction perpendicular to sheet (*i.e.* z-axis). By Fourier interpolating the energies obtained for (x,y) points on a 6x6 mesh using DFT calculations, we construct the energy-surface (γ):

$$\begin{aligned} \gamma(x,y) &= \frac{E(x,y) - E(0,0)}{A} \\ &= \frac{1}{\sqrt{6}} \sum_{p=0}^{5} \frac{1}{\sqrt{6}} \sum_{q=0}^{5} A_{p,q} \exp\{i(2\pi k_p x + 2\pi k_q y)\}, \end{aligned} \tag{4.2}$$

where $E(x,y)$ is energy of a configuration $\vec{d}(x,y)$ relative to the *1H* structure, and A is the area of the unit cell. $k_{p,q} \in \{0,1,2,3,-2,-1\}$ and $A_{p,q}$ are the coefficients obtained from discrete Fourier transform of energies of configurations $\vec{d}(x,y)$ corresponding to points on a 6x6 grid in real space. The coefficients $A_{p,q}$ possess the symmetry of the crystal, and we note that the γ-surface (see Figure 4.1) exhibits a reflection symmetry about ($\bar{1}$, 1) direction (see direction $\vec{p_3}$ in Figure 4.1 and Figure 4.2), which is used to reduce the number of configurations simulated.

A local minimum of the γ-surface (denoted as γ_C) located at the slip (glide) of

$(\frac{2}{3},\frac{1}{3})$ corresponds to the *1T* polymorph. *1T* polymorph of MX_2 has ABC stacking of the X-M-X planes of atoms, and close packed network of MX_6 octahedra with M-atom at the site of inversion symmetry makes it metallic (see Figure 4.3). Our estimate of the energy of *1T* structure of MX_2 compounds is in the range of 1.18 to 1.51 J/m^2 (0.7-0.8 eV/f.u.) (see Table 4.1, Figure 4.1 and Figure 4.2), and comparable to the surface energy of metals like copper ($\approx$ 1.73 J/m^2) and gold ($\approx$ 1.48 J/m^2) [118]. We note that the relative energies of *1T* polymorphs of MSe_2 (w.r.t. the *1H* form) are generally smaller than those of MS_2, and we expect that the *1T* polymorph is expected to be more stable in the selenides than in sulphides.

From Figure 4.1, we see that a MX_2 monolayer needs to overcome an energy barrier when it transforms from the *1H* to the *1T* structure. A configuration at the energy barrier *i.e.* the transition state is a point in γ-surface (denoted as $\gamma_B = \gamma_E = \gamma_F$) representing an unstable equilibrium, and occurs at slips of $(\frac{5}{6},\frac{1}{6})$, $(\frac{5}{6},\frac{2}{3})$ and $(\frac{1}{3},\frac{1}{6})$. The estimated energies of the transition state of the four MX_2 compounds are in the range of 2.47-3.01 J/m^2 (1.5-1.7 eV/f.u.) (see Table 4.1 and Figure 4.1). In these structures (see B, E and F in Figure 4.1), the X-atom lies on top of the midpoint of the bond connecting two nearest M atoms in the hexagonal lattice. These three configurations are symmetry-equivalent (hence of same energies), and have been indicated in the contour plot of γ-surface (see Figure 4.1 and Figure 4.2). This implies that there are three equivalent paths (along $\vec{p_1}$, $\vec{p_2}$ and $\vec{p_3}$, where $\vec{p_1}$ and $\vec{p_2}$ are related by reflection symmetry) of transformation of the ideal *1H* structure to the *1T* configuration, that involve the barriers of same energy (see Figure 4.2).

The maximum energy on the γ-surface (denoted as γ_D) occurs at a slip of $\vec{d} = (\frac{1}{3},\frac{2}{3})$, and it ranges from 3.81 to 4.51 J/m^2 (2.3-2.5 eV/f.u.) (see Table 4.1) for different MX_2 compounds. This configuration in which the top X sublattice plane is on the top of the M atom (Figure 4.1A) is unstable w.r.t. x and y-directions. The other set of calculations in which the top X-atom was allowed to relax in all the

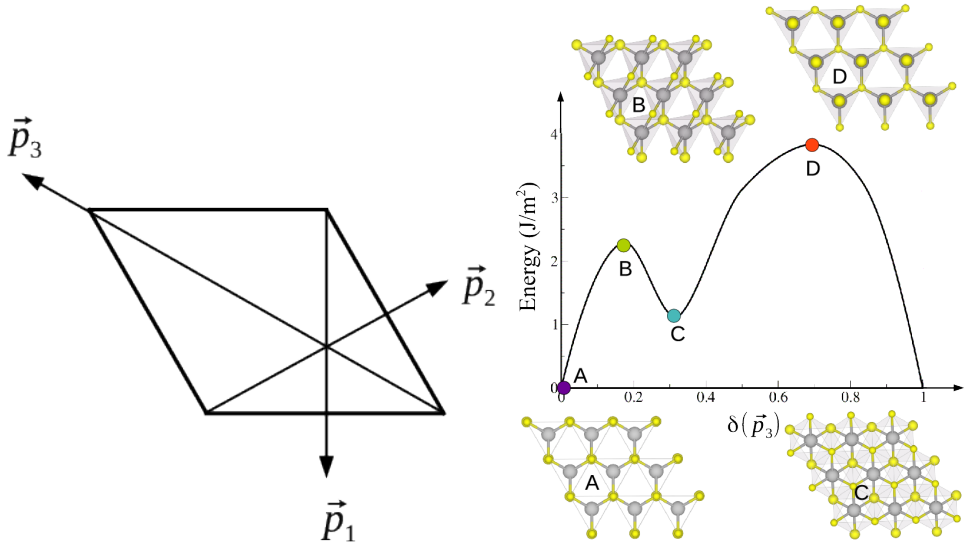

(a) (b)

Figure 4.2: Unit cell with three symmetry directions forming the transition paths, section of the γ-surface along one of these directions and atomic structures of the extremum points along such a path. (a) Unit cell of MX_2 and the three directions denoted by arrows $\vec{p_1}$, $\vec{p_2}$ and $\vec{p_3}$ (where $\vec{p_1}$ and $\vec{p_2}$ are equivalent directions). (b) shows the sections of γ-surface along the $\vec{p_3}$ direction. Top view of the structures of monolayer of MX_2 at extreme points of the γ-surface is shown in (b). X-atoms are denoted by yellow (small) spheres and Mo-atoms by grey spheres. To distinguish between two X planes, the top X atoms are denoted by smaller radii than the bottom ones.

directions, showed that the energies of the local minima remain unchanged. Also, the energy of the transition state (*i.e.* γ_B) reduces by $\approx 0.03\ J/m^2$.

Table 4.1: Energies of local minima (γ_C), minimum energy barrier (γ_B) and maximum energy barrier (γ_D) w.r.t. *1H* structure, of energy surface for MX_2 (M= Mo, W and X= S, Se).

	γ_C, (x,y = $\frac{2}{3}$,$\frac{1}{3}$)		γ_B, (x,y = $\frac{5}{6}$,$\frac{1}{6}$; $\frac{5}{6}$, $\frac{2}{3}$; $\frac{1}{3}$,$\frac{1}{6}$)		γ_D,(x,y = $\frac{1}{3}$,$\frac{2}{3}$)	
Compound	e (J/m^2)	e (eV/fu)	e (J/m^2)	e (eV/fu)	e (J/m^2)	e (eV/fu)
MoS_2	1.51	0.83	2.80	1.54	4.37	2.40
$MoSe_2$	1.18	0.70	2.28	1.35	3.81	2.26
WS_2	1.61	0.88	3.01	1.65	4.51	2.47
WSe_2	1.29	0.77	2.47	1.47	3.94	2.35

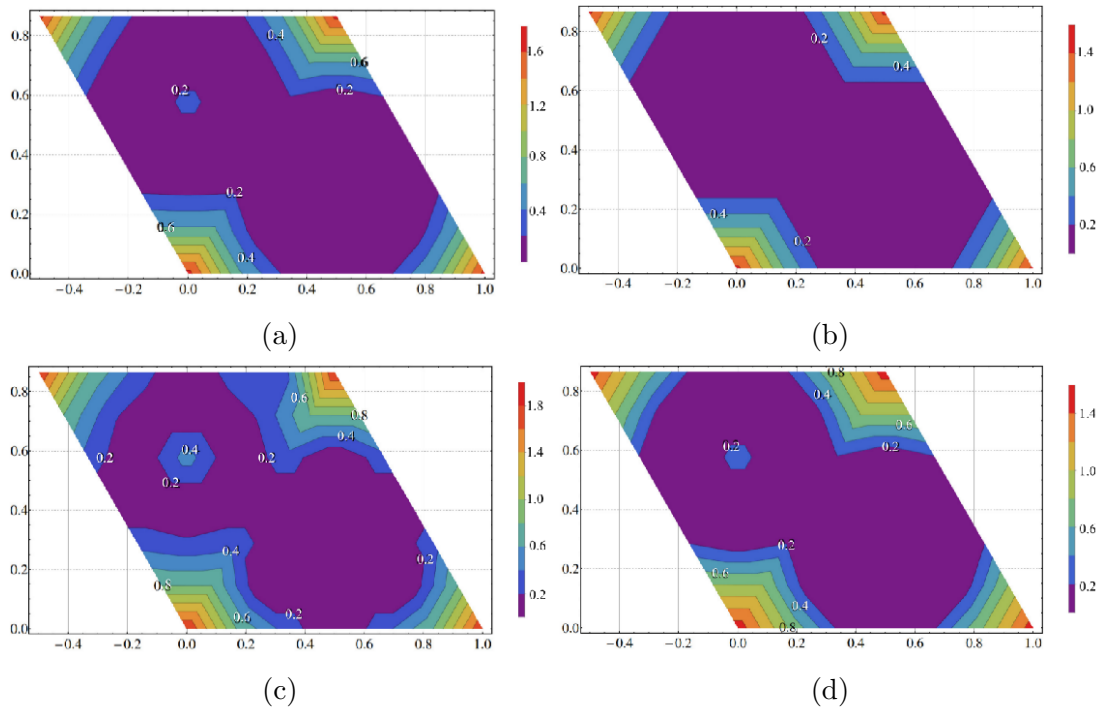

Figure 4.3: Contour plot of the band gap $E_g(x,y)$ of monolayer of MX_2 as a function of slip/glide for (a) MoS_2, (b) $MoSe_2$, (c) WS_2, and (d) WSe_2. Note the absence of island with nonzero band gap in the region of metallic states of $MoSe_2$.

Electronic structure

We now examine the electronic band gap of MX_2 monolayers in structural configurations associated with glide on the uniform 6x6 mesh in the real space unit cell, and visualize its Fourier interpolation $E_g(x,y)$ with contour plot (see Figure 4.3). We find that the band gap vanishes in most of the region $[(x,y) \in [0,1)]$ centered at *1T* structure, and is nonzero only in a tiny region centred at the *1H* structure, where MoS_2, $MoSe_2$, WS_2 and WSe_2 monolayers exhibit direct band gaps of 1.68 eV, 1.46 eV, 1.80 eV and 1.52 eV respectively. We note that Mo compounds typically have a lower band gap than the respective W compounds and, amongst Mo/W TMDCs, compounds with Se have a lower band gap than ones with S in respective metals. Lower band gaps indicate softer bonds [119], and imply that bonding in $MoSe_2$ is the weakest amongst these compounds. In the contour plot of the band gaps (refer

to Figure 4.3), we observe that only $MoSe_2$ has a vanishing gap at its γ_D configuration, and is also related to the nature of bonding *i.e.* softest bonds in $MoSe_2$. We note the pathway of the *1H* to *1T* polymorph transition invariably passes through metallic states (see Figure 4.3).

4.1.4 Vibrational spectra and stability

We now assess the structural stability of the *1H* and *1T* polymorphs of MX_2 compounds through determination of their phonon spectra. If the phonon spectrum exhibits phonon modes with imaginary frequencies, it means that the structure is locally unstable (it is a saddle point in energy landscape), else it is stable. The eigen displacements of the unstable modes give energy lowering structural distortion. Our results for phonons of the stable structural form are also useful in Raman and infra-red (IR) characterization of these structures.

1H structure

Phonon dispersions of the *1H* polymorph of each of the four compounds exhibit no unstable modes (*i.e.* imaginary frequencies), establishing that the *1H* structure is a stable polymorphic form (refer to Figure 4.4, left panel). Higher mass of Se results in lower frequencies of MSe_2 compounds than those of the respective MS_2, and the bandwidth of phonon modes of *1H* MSe_2 is typically smaller as compared to those of *1H* MS_2. Interestingly, the optical bands of WSe_2 with in-plane and out of plane atomic displacements are split, whereas they overlap in frequency forming a single band of optical phonons in the other three compounds.

The Raman active A_{1g} modes of *1H* polymorph of MoS_2, WS_2 and $MoSe_2$, WSe_2 are at 388 cm^{-1}, 398 cm^{-1} and 285 cm^{-1}, 392 cm^{-1} respectively, whereas, the doubly degenerate E^1_{2g} Raman active mode is at 375 cm^{-1}, 344 cm^{-1} and 292 cm^{-1}, 258 cm^{-1} for MoS_2, WS_2, $MoSe_2$ and WSe_2 respectively (refer Table 4.3). Note that

the A_{1g} mode of $MoSe_2$ (285 cm^{-1}) is softer than the E^1_{2g} mode, in contrast to the trend seen in other compounds and in agreement with previous report by Sugai *et al.* [120]. This change in the trend in $MoSe_2$ can be traced back to its force constants relevant to shear and compressive deformations [120].

1T structure

Our analysis of the vibrational spectra of the c*1T* polymorph reveals that all the four MX_2 compounds studied here are structurally unstable, and exhibit structural instabilities with imaginary frequencies in the range of 100i cm^{-1} to 200i cm^{-1} (refer to Figure 4.4, right panel). The unstable modes are doubly degenerate at the high symmetry K-point of the BZ, and singly degenerate at the M-point of the BZ. We discuss the K-point instability and its consequences to the structure of the *1T* form in subsection (a), followed by similar analysis of the M-point instability in subsection (b).

Table 4.2: Energetics, metal-metal bond lengths, polarization and domain wall energies of *1T* polymorph of MX_2 compound. $\Delta E' = E_{c1T}$ - E_{1H} and $\Delta E = E_{d1T}$ - E_{c1T} are given in eV per formula unit (distorted *IT* (d*1T*) structures: $\sqrt{3}$x$\sqrt{3}$ and $\sqrt{3}$x1 superstructure). b_{d1T} and b_{c1T} are the bond lengths of metal-metal bond of d*1T* and c*1T* structures respectively. E_R is relative energy of $\sqrt{3}$x1 w.r.t. $\sqrt{3}$x$\sqrt{3}$. P_z is the polarization of *1T* polymorph of MX_2 in the direction perpendicular to sheet (z-direction). D_W is formation energy of the domain walls separating domains of opposite polarization.

Compound	$\Delta E'$ (eV/fu)	b_{c1T} (Å)	b_{d1T} ($\sqrt{3}$x1) (Å)	ΔE ($\sqrt{3}$x1) (eV/fu)	b_{d1T} ($\sqrt{3}$x$\sqrt{3}$) (Å)	ΔE ($\sqrt{3}$x$\sqrt{3}$) (eV/fu)	E_R (eV/fu)	P_z ($\sqrt{3}$x$\sqrt{3}$) (μC/cm^2)	D_W ($\sqrt{3}$x$\sqrt{3}$) (eV/Å)
MoS_2	0.82	3.2	2.7	-0.28	3.0	-0.28	0.004	0.27	0.004
$MoSe_2$	0.70	3.3	2.8	-0.34	3.1	-0.28	-0.072	0.26	-0.003
WS_2	0.89	3.2	2.7	-0.35	3.0	-0.31	-0.052	0.25	-0.002
WSe_2	0.76	3.3	2.8	-0.47	3.1	-0.32	-0.146	0.25	-0.02

(a) K-point instability: $\sqrt{3} \times \sqrt{3}$ superstructure

We first note that the degeneracy of the K-point instability is lifted at wavevector q in the neighborhood of K (*i.e.* q = K + δ k, refer to Figure 4.4 right panels).

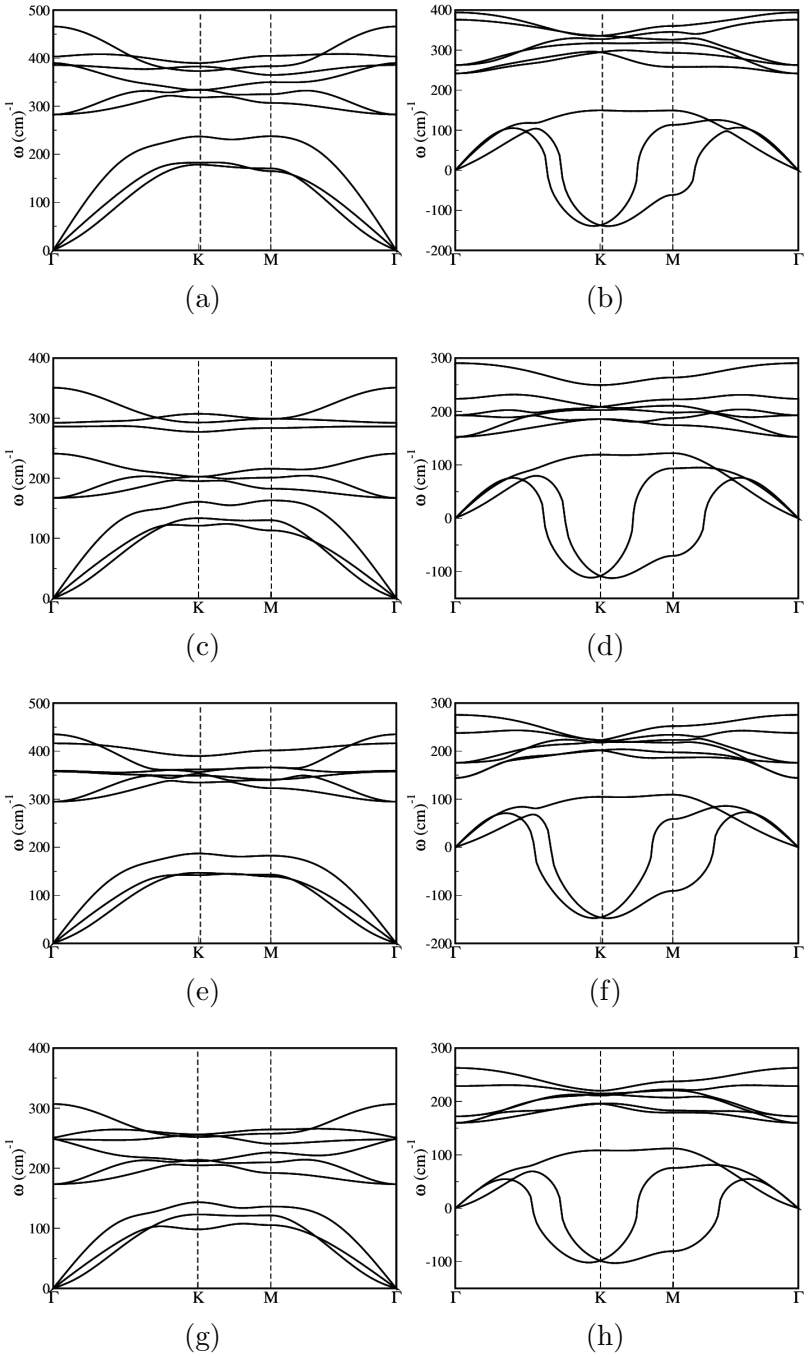

Figure 4.4: Phonon dispersion of monolayered of MX_2 with *1H* structure (left panel) and c*1T* structure (right panel), MoS_2 in (a) and (b), $MoSe_2$ in (c) and (d), WS_2 (e) and (f), and WSe_2 in (g) and (h). Note that the instability at the K-point in *1T* MX_2 is doubly degenerate, and the degeneracy is split at points away from K. The instability at M-point is singly degenerate.

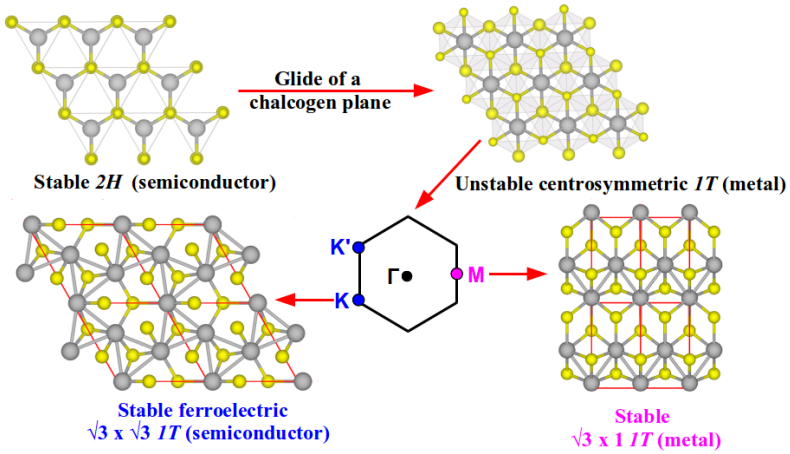

Figure 4.5: Top view of 1H, c1T, $\sqrt{3}\times\sqrt{3}$ 1T and $\sqrt{3}\times 1$ 1T structures. A schematic diagram showing systematic transition of 1T stucture (unstable) to stable structures $\sqrt{3}\times\sqrt{3}$ 1T structure and $\sqrt{3}\times 1$ 1T structure which is lead by K-point and M point instabilities.

This evolves into two singly degenerate unstable modes, one of which constitutes a slightly stronger instability than that at K-point. Since there are two equally unstable modes at the K-point that can lower the energy through distortion of the *1T* polymorph as opposed to a single strongly unstable mode at K + δ k, we expect the lowest energy structure to arise from freezing of the K-point instability. The structural distortion associated with atomic displacements of the K_3 mode leads to a cell tripled ($\sqrt{3}$x$\sqrt{3}$) superstructure with trimerization of metal atoms [121,122] (see Figure 4.5). The trimerization of metal atoms which involves bonding through the d^2 electronic states of transition metals these MX_2 compounds, lowers the energy of the *1T* polymorph by $\approx$ 0.28 to 0.32 eV/f.u. (refer to Table 4.2). It leads to reduction in M-M bond lengths by 0.2 Å (refer to Table 4.2) and is accompanied by the opening of a band gap $\approx$ 0.6 to 0.8 eV marking a metal-semiconductor transition. Along with this, we perform full (atomic and cell) relaxation of $\sqrt{3}$x$\sqrt{3}$ structure as stresses on the unit cell ($\sigma_{xx} = \sigma_{yy} \sim$ 12 kbar to 24 kbar) are bit large due to trimerization of metal atoms. The lattice constants (a=b) of $\sqrt{3}\times\sqrt{3}$ structure of MoS_2, $MoSe_2$, WS_2 and WSe_2 change by 1.8% 1.2%, 2.2% and 1.5% respectively

w.r.t. the lattice parameters of c*1T* structure.

Phonon dispersion of the $\sqrt{3}$x$\sqrt{3}$ *1T* structure of each of the four compounds exhibits no unstable modes, confirming its metastability (Figure 4.6). The signatures of the $\sqrt{3}$x$\sqrt{3}$ superstructure can also be seen in its Raman spectra. The E_{1g} and A_{1g} Raman active modes of MoS_2 (WS_2) are at 292 cm^{-1} (292 cm^{-1}) and 402 cm^{-1} (411 cm^{-1}) respectively. In comparison, the E_{1g} and A_{1g} modes of $MoSe_2$ (WSe_2) are at 148 cm^{-1} (152 cm^{-1}) and 227 cm^{-1} (257 cm^{-1}) respectively. Along with E_{1g} and A_{1g} modes, we find that there exist four additional Raman active modes (which we name as J_1, J_2, J_3 and J_4) in all the MX_2 compounds. These modes (refer to Table 4.3) are the Raman signatures that can be used to clearly detect the $\sqrt{3}$x$\sqrt{3}$ superstructure of these materials. We note that the Raman active modes of MoS_2 and WS_2 (refer to Table 4.3) lie in the same range of frequencies, and the same holds for $MoSe_2$ and WSe_2.

Table 4.3: Raman active modes of *1H* and *1T* ($\sqrt{3}$x$\sqrt{3}$ and $\sqrt{3}$x1 superstructures) polymorphs of MX_2.

Structure	Raman Modes	MoS_2 (cm^{-1})	$MoSe_2$ (cm^{-1})	WS_2 (cm^{-1})	WSe_2 (cm^{-1})
1H	A_{1g}	388	285	398	392
	E^1_{2g}	375	292	344	258
	A_{1g}	402	227	411	257
	E_{1g}	292	148	292	152
1T	J_1	178	127	156	132
($\sqrt{3}$x$\sqrt{3}$)	J_2	203	159	150	128
	J_3	270	180	260	175
	J_4	376	319	360	273
1T	A_{1g}	391	222	391	254
($\sqrt{3}$x1)	E_{1g}	268	139,143	258,268	141,147

(b) M-point instability: $\sqrt{3} \times 1$ superstructure

On freezing in the eigen-displacements of the unstable mode at M-point of the *1T* polymorph, we obtain a $\sqrt{3}$x1 superstructure (see Figure 4.5) with zigzag chains

of metal atoms. Our analysis shows that the $\sqrt{3}$x1 superstructure is same as the precursor (α phase) observed in the *1H* to *1T* phase transformation by Lin *et al.* [112]. This distorted structure involving dimerization of metal atoms (where the M-M bonds are contracted by 0.5 Å (refer to Table 4.2)) is metallic (see Figure 4.7), and a better candidate for HER activity than $\sqrt{3}$x$\sqrt{3}$ *1T* and *1H* polytypes [99]. Along with this, we perform full relaxation of of $\sqrt{3}$x1 structure as the stresses along y-direction are large ($\sigma_{yy} \sim$ 30 kbar to 34 kbar) due to dimerization of metal atoms. The lattice constants b (a) of $\sqrt{3} \times 1$ structure of MoS_2, $MoSe_2$, WS_2 and WSe_2 vary by 3.7% (-0.2%), 4.0% (-1.1%), +3.7% (-0.4%) and 3.6% (-0.4%) respectively w.r.t. the lattice parameters of c*1T* structure.

Phonon dispersion of the $\sqrt{3}\times 1$ *1T* superstructure of each of the four compounds (see Figure 4.6) exhibits no unstable modes, hence confirming its metastability. Spectroscopic signatures of the $\sqrt{3}$x1 superstructure can be identified in the E_{1g} and A_{1g} Raman active modes. Due to lower symmetry of the dimerized structure, the degeneracy of E_{1g} mode is split. We find that for MoS_2 (WS_2) the E_{1g} and A_{1g} modes are at 268 cm^{-1} (258 cm^{-1} and 268 cm^{-1}) and 391 cm^{-1} (391 cm^{-1}) respectively. Similarly, the E_{1g} and A_{1g} modes of $MoSe_2$ (WSe_2) are at 139 cm^{-1} and 143 cm^{-1} (141 cm^{-1} and 147 cm^{-1}) and 222 cm^{-1} (254 cm^{-1}) respectively (refer Table 4.3).

We find that the $\sqrt{3}$x$\sqrt{3}$ superstructure is energetically more stable than the $\sqrt{3}$x1 superstructure in MoS_2, which is in contrast to the other MX_2 compounds where the $\sqrt{3}$x1 superstructure is more stable (refer to ΔE in Table 4.2). These two superstructures can be differentiated experimentally from the signatures in the Raman spectra of MX_2 compounds. In contrast, change in frequency for the A_{1g} and E_{1g} modes are softer in $\sqrt{3}$x1 than in $\sqrt{3}$x$\sqrt{3}$ superstructure. The E_{1g} mode of $\sqrt{3}$x1 superstructure of MoS_2 (WS_2) and $MoSe_2$ (WSe_2) are softer by $\approx$ 25 cm^{-1} (9 cm^{-1}) and 34 cm^{-1} (11 cm^{-1}) respectively. For the A_{1g} mode in contrast, the

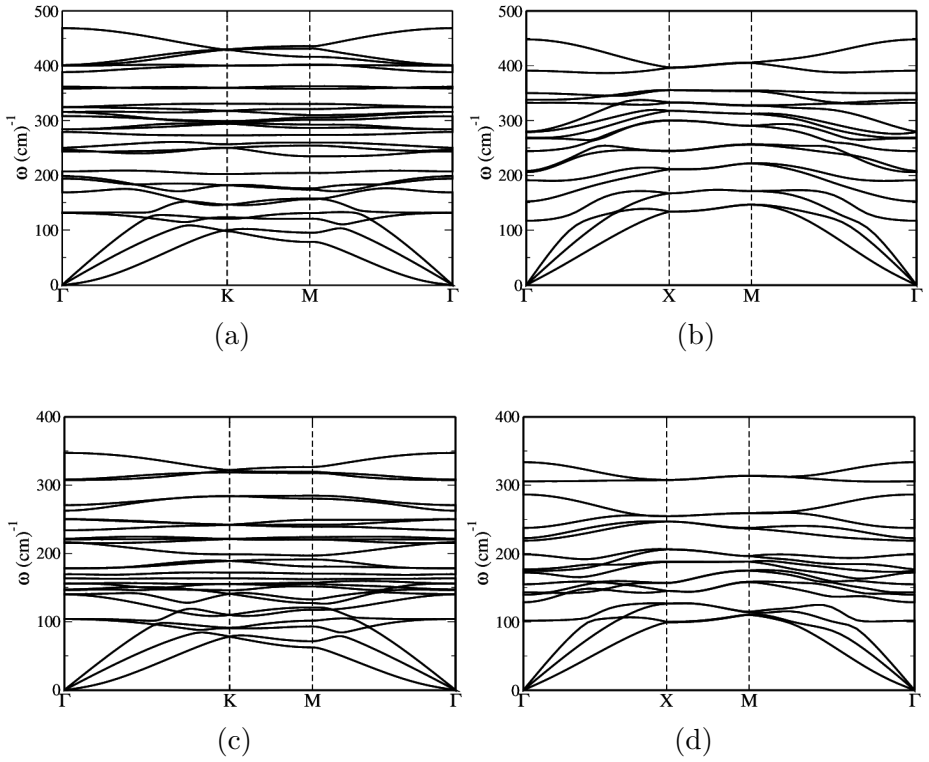

Figure 4.6: Phonon dispersion of monolayered of MX_2 with $\sqrt{3}$x$\sqrt{3}$ *1T* structure (left panel) and $\sqrt{3}$x1 *1T* structure (right panel), MoS_2 in (a) and (b), and $MoSe_2$ in (c) and (d).

changes in frequency are 11 cm^{-1} (20 cm^{-1}) and 5 cm^{-1} (3 cm^{-1}) for MoS_2 (WS_2) and $MoSe_2$ (WSe_2) respectively in the two superstructures. We see that the change in the frequency of the A_{1g} mode is not as significant as the E_{1g} mode for all the compounds. Secondly, the shift in the frequency of E_{1g} mode is more pronounced for MS_2 compounds than in the MSe_2 compounds. Hence, the Raman signatures can be used to distinguish between the $\sqrt{3}$x1 and $\sqrt{3}$x$\sqrt{3}$ superstructures of MS_2 compounds experimentally.

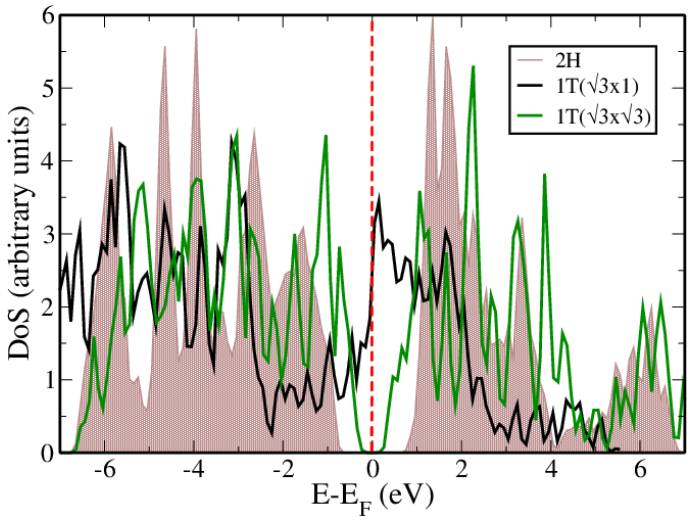

Figure 4.7: Electronic density of states (DoS) of MoS_2 in its *1H* and *1T* ($\sqrt{3}$x$\sqrt{3}$ and $\sqrt{3}$x1 superstructure) polymorphs.

4.1.5 Transition pathways from $\sqrt{3}\times\sqrt{3}$ to *1H*, $\sqrt{3}\times 1$ to *1H* and $\sqrt{3}\times 1$ to $\sqrt{3}\times\sqrt{3}$

To estimate energy barriers relevant to the transitions from $\sqrt{3}\times\sqrt{3}$ to *1H*, $\sqrt{3}\times 1$ to *1H* and $\sqrt{3}\times 1$ to $\sqrt{3}\times\sqrt{3}$ structures, we determine the transition using nudged elastic band method [123] as implemented in Quantum ESPRESSO package [41]. From Table 4.4, we record that energy barriers for the transitions from $\sqrt{3}\times\sqrt{3}$ to *1H* structure are 1.06 eV/fu, 0.96 eV/fu, 1.20 eV/fu and 1.10 eV/fu for MoS_2, $MoSe_2$, WS_2 and WSe_2 respectively. Similarly, energy barriers for a transition from $\sqrt{3}\times 1$ to *1H* structure are much smaller 0.75 eV/fu, 0.70 eV/fu, 0.60 eV/fu and 0.80 eV/fu for MoS_2, $MoSe_2$, WS_2 and WSe_2 respectively. Finally, the energy barriers for a transition from $\sqrt{3}\times 1$ to $\sqrt{3}\times\sqrt{3}$ structure are even smaller 0.025 eV/fu, 0.085 eV/fu, 0.078 eV/fu and 0.163 eV/fu for MoS_2, $MoSe_2$, WS_2 and WSe_2 respectively (refer Table 4.4). We find that the *1H* to $\sqrt{3}\times 1$ structural transition is an easier transformation than the one from *1H* to $\sqrt{3}\times\sqrt{3}$ structure in all the 4 compounds. To stabilize $\sqrt{3}\times\sqrt{3}$ structure in MoS_2, we need to stabilize $\sqrt{3}\times 1$ structure first.

Table 4.4: Energy barriers for the transition from (a) $\sqrt{3}$x$\sqrt{3}$ to *1H* (b) $\sqrt{3}$x1 to *1H* and (c) $\sqrt{3}$x1 to $\sqrt{3}$x$\sqrt{3}$ structure of MX_2 compounds.

Compound	E (eV/fu) ($\sqrt{3}$x$\sqrt{3}$ to *1H*)	E (eV/fu) ($\sqrt{3}$x1 to *1H*)	E (eV/fu) ($\sqrt{3}$x1 to $\sqrt{3}$x$\sqrt{3}$)
MoS_2	1.06	0.75	0.025
$MoSe_2$	0.96	0.70	0.085
WS_2	1.20	0.60	0.078
WSe_2	1.10	0.80	0.163

The transition path calculations show that the $\sqrt{3} \times 1$ and $\sqrt{3} \times \sqrt{3}$ structures are quite comparable in energy and the barriers along the path between them are also quite small (refer Table 4.4, Figure 4.8). Notably, the intermediate structures (refer Figure 4.8) have lower energy than $\sqrt{3} \times \sqrt{3}$ structure in $MoSe_2$, WS_2 and WSe_2. A careful examination of these structures reveals that these structures are a strained $\sqrt{3} \times 1$ structure. Hence, $\sqrt{3} \times 1$ structure is more stable than the $\sqrt{3} \times \sqrt{3}$ structure in $MoSe_2$, WS_2 and WSe_2 whereas $\sqrt{3} \times \sqrt{3}$ structure is more stable than $\sqrt{3} \times 1$ structure in MoS_2 (refer to Figure 4.8). Our analysis confirms why the $\sqrt{3} \times 1$ structure [116] is more commonly observed than the $\sqrt{3} \times \sqrt{3}$ structure [116].

4.1.6 Ferroelectricity of the $\sqrt{3} \times \sqrt{3}$ *1T* polymorph

Based on the prediction of ferroelectricity the $\sqrt{3}$x$\sqrt{3}$ superstructure of MoS_2 [5], we now investigate ferroelectric properties and domains in $\sqrt{3}$x$\sqrt{3}$ superstructure of the MX_2 compounds, (the metallic $\sqrt{3}$x1 phase does not exhibit ferroelectricity). The inversion symmetry in the cell tripled ($\sqrt{3}$x$\sqrt{3}$) structure [5] is broken because of the anharmonic coupling of the K-point unstable mode (K_3) with a stable polar mode (Γ_2^-). Once the ordering driven by the primary instability K_3 sets in, this coupling leads to condensation of the polar mode in the structure, and hence to a spontaneous polarization perpendicular to the plane of the MX_2 sheet ranging from $\approx$ 0.25 to 0.27 μC/cm^2 (refer to Table 4.2). Since ferroelectricity in the $\sqrt{3} \times \sqrt{3}$

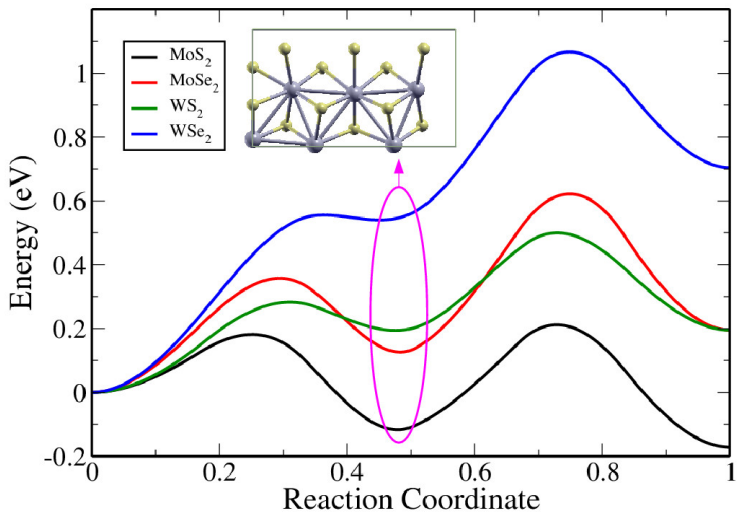

Figure 4.8: Transition pathways from $\sqrt{3}$x1 to $\sqrt{3}$x$\sqrt{3}$ superstructure of all the MX_2 compounds. Initial and final images are $\sqrt{3}$x1 and $\sqrt{3}$x$\sqrt{3}$ structures respectively. Structure of intermediate image is shown, where M atoms are denoted by grey spheres and X atoms are denoted by yellow spheres.

1T structure results from trimerization of M atoms that induce polar distortion of the centrosymmetric *1T* phase of MX_2, it is certain that $\sqrt{3} \times \sqrt{3}$ *1T*-MoX_2 is a ferroelectric [124]. This is based on symmetry argument and is robust. Thus, we demonstrate that the $\sqrt{3}$x$\sqrt{3}$ *1T* superstructure of $MoSe_2$, WS_2 and WSe_2 compounds too exhibit ferroelectricity, in agreement with the predictions of Shirodkar *et al.* [5]. However, based on our results in Sec. IV, it will quickly transform to $\sqrt{3} \times 1$ structure.

Domains of different orientations of polarization are crucial to its switching with electric field, which is relevant to application of a ferroelectric in memory devices. Unrealistically large electric field (coercive field) is required to switch polarization through *homogeneous* nucleation of domains of P with opposite orientation. It is reduced considerably in practice due to the presence of heterogeneously distributed defects, which facilitate nucleation of ferroelectric domains [5] at lower electric field.

Applications of these MX_2 compounds as ferroelectric semiconductors in the dipolectronic devices requires them to exhibit a stable ferroelectric dipolar domain structure. We estimate stability of domains through simulation to calculate domain wall energy as:

$$D_w = \frac{E(180^\circ\ domains) - E_{FE}}{A} \tag{4.3}$$

where, $E(180^\circ\ domains)$ and E_{FE} are the energies of a configuration with 180° (up and down) polarized domains and bulk ferroelectric (with uniform polarization) respectively. The area (A) is calculated as a product of length of domain wall and d (thickness of the 2-D sheet of MX_2). We note that stable domain wall configuration indicates (positive energy) that the monolayer can support 180° domains of opposite polarization, which is necessary for polarization switching, a defining property of ferroelectrics. Secondly, the size of these domains is much larger than the periodicity of a typical antiferroelectric phase. To this end, we obtained the minimum energy structure starting with two domain walls (per supercell) separating the domains with opposite polarization (refer to Table 4.2). Except for MoS_2, we find that none of the other compounds ($MoSe_2$, WS_2 and WSe_2) exhibit stable domain walls: our estimates of negative domain wall energy in the latter indicate their natural instability (refer to Table 4.2) and the fact that the structural relaxation of these configurations with domain walls leads to formation of the $\sqrt{3}$x1 superstructure, which is lower in energy. Thus, the relative stability between $\sqrt{3}$x1 and $\sqrt{3}$x$\sqrt{3}$ superstructures is essentially reflected in the negative domain wall energies given in Table 4.2. The ferroelectric domain walls are thus topological structural excitations that may drive the $\sqrt{3}$x$\sqrt{3}$ to $\sqrt{3}$x1 structural transformation in $MoSe_2$, WS_2 and WSe_2 due to applied electric field.

While the ferroelectric semiconducting $\sqrt{3}$x$\sqrt{3}$ superstructure of *1T* polymorphic phase is locally stable in all the compounds, it is more stable than the $\sqrt{3}$x1 *1T* phase

only in MoS_2. Thus, only MoS_2 has the potential to be used as a semiconducting ferroelectric in the dipolectronic devices proposed in Ref. [5].

4.1.7 Anomalous response to electric field

Response of an insulating single crystal to electric field is through redistribution of its electronic charge and ionic positions. Dielectric constant is a measure of the strength of screening of electric fields in a material. In 2-D materials like MoS_2, dielectric constant has been shown to be crucial in changes in its optical properties that involve formation of excitons and trions [125] due to external electrostatic environment. Here, we highlight certain anomalous aspects of ionic response of MX_2 monolayers to electric field, which reflect the fact that they are sensitive to external fields and can readily undergo metal-semiconductor phase transitions discussed earlier in Section 3.

Table 4.5: Born effective charges (Z^*) and electronic dielectric constants (ϵ^∞) for *1H* and *1T* ($\sqrt{3}$x$\sqrt{3}$ superstructure) polymorphs of MX_2.

Structure	*1H*					*1T*($\sqrt{3}$x$\sqrt{3}$)
	Z^*_{xx}		Z^*_{yy}		ϵ^∞_{xx}=ϵ^∞_{yy}	ϵ^∞_{xx}=ϵ^∞_{yy}
Compound	M	X	M	X		
MoS_2	-1.0	0.5	-1.2	0.5	7.6	11.3
$MoSe_2$	-1.9	0.9	-2.0	0.9	8.5	11.5
WS_2	-0.4	0.2	-0.5	0.2	7.0	11.7
WSe_2	-1.2	0.5	-1.3	0.5	7.9	11.7

We first determine the dielectric properties of both the semiconducting forms (*1H* and $\sqrt{3}$x$\sqrt{3}$ *1T*) of MX_2 compounds. Due to a smaller band gap in the $\sqrt{3}$x$\sqrt{3}$ superstructure, its electronic contribution to dielectric constant ϵ^∞ (optical dielectric constant) is significantly (by $\approx$ 50 %) larger than that of the *1H* polymorph. While ϵ^∞_{xx}=ϵ^∞_{yy} is in the range of 7 to 8.5 for the *1H* polymorph, it ranges from 11 to

12 for the $\sqrt{3}$x$\sqrt{3}$ superstructure (refer to Table 4.5) of *1T* polymorph. These dielectric constants are relevant to electronic, excitonic and trionic properties of these materials.

The lower (THz) frequency dielectric response has contributions from phonons as well, which is proportional to squared mode (Born) effective charges and depends inversely on the square of their frequencies [126]. Born effective charge ($Z^*_{i,\alpha,\beta}$) gives the force acting on an ion (i) in the 'α' direction when an electric field is applied in the 'β' direction (E_β). An anomalously large Z^* is often an indicator of the tendency of a material to undergo a ferroelectric distortion, or its vicinity to metallicity of the compound [127]. Increase in metallicity or covalency is reflected in the increase in anomalous nature of Z* measured by the deviation from the nominal charge. Due to strong screening of electric field by conduction electrons in the metallic $\sqrt{3}$x1 superstructures, the dielectric constant or Born effective charges are not physically meaningful.

Since the *1H* polymorph of MX_2 compounds is a relatively a wider band gap semiconductor, the in-plane Born effective charges are expected to be closer to their nominal charges (*i.e.* +4 for M and -2 for X). However, we find that the values and even the sign of Z^* are counter-intuitive, where Z^* of M atoms is in the range from -0.5 to -2 (see Table 4.5) and that of X atom is in that of +0.2 to +0.9. Anomalous values of Z^* are due to strong covalency in these materials, and the opposite sign of Z^* arises from the contribution of the d-states of M atoms constituting the top most valence band just below the Fermi level. The $\sqrt{3}$x$\sqrt{3}$ *1T* form exhibits an even stronger anomaly (see Table 4.5) and, its Z^* is larger in magnitude by a factor of 2.5 than of *1H* due to a smaller band gap. We find that the in-plane Born effective charges for the M atoms are in the range of +0.7 to -5, and +2 to -2 for X atoms. Such anomalous Z^* is due to its vicinity primarily to a metal to semiconductor transition of the c*1T* polymorph, and associated electron phonon coupling [5].

4.1.8 Conclusions

Using first-principles density functional theoretical calculations, we have determined the energies and electronic structure of the states along the transition pathway connecting $1H$ and c$1T$ structures of monolayers of MX_2 (M= Mo, W and X= S, Se). We find that the c$1T$ structure is typically higher in energy by 0.7-0.9 eV/f.u. than the $1H$ structure. Secondly, an energy barrier associated with this transition through glide of a plane of X atom is about 1.5 to 1.7 eV. We have shown that the c*1T* polymorphic structure is unstable, exhibiting instabilities at the valley point K and zone boundary point M. These structural instabilities lead to symmetry and energy lowering distortions of the $c1T$ structure to form $\sqrt{3}$x$\sqrt{3}$ (for K-point) and $\sqrt{3}$x1 (for M-point) stable superstructures respectively. The $\sqrt{3}$x1 superstructure associated with dimerization of metal atoms remains metallic, while the $\sqrt{3}$x$\sqrt{3}$ superstructure exhibit a nonzero electronic band gap arising from trimerization of metal atoms. We find a considerable softening of A_{1g} and E_{1g} modes in the $\sqrt{3}$x1 superstructure as compared to the $\sqrt{3}$x$\sqrt{3}$ structure, which can be used as the Raman signatures to distinguish between the two. These, along with four new Raman modes of the semiconducting $\sqrt{3}$x$\sqrt{3}$ superstructure, will be useful in experimental verification of these subtle features of the *1T* structural form.

Finally, the $\sqrt{3}$x$\sqrt{3}$ structure of (Mo,W)$(S,Se)_2$ exhibits a spontaneous polarization (0.25-0.3μC/cm^2) along the direction perpendicular to the sheet, making it the thinnest known ferroelectric. However, the $\sqrt{3}$x$\sqrt{3}$ structure is (a) more stable than the $\sqrt{3}$x1 structure, and (b) exhibits a stable dipolar domain structure *only* in MoS_2. Thus, MoS_2 is the only suitable candidate for use in the *dipolectronic* devices proposed earlier [5]. As a result of vicinity of these compounds to metal-semiconductor and ferroelectric transitions, all of them exhibits anomalous response to electric field.

4.2 Nuances in electronic structure of 1T-phases of MoS_2

4.2.1 Introduction

MoS_2 is undoubtedly important member of the TMDCs family for applications in transparent and flexible electronics due to its finite bandgap and extraordinary electrostatic gate coupling properties at lower dimension [16, 20, 100, 128, 129]. While MoS_2 is stable in 1H structure, it exhibits various trigonal polymorphic forms [130,131] such as 1T, 1T′, 1T″ and 1T‴. These structural forms are metastable and can be kinetically formed as small patches embedded in the majority 1H form during chemical exfoliation [132]. The electronic properties of stable 1H form has been extensively studied as a wide direct band gap (1.9 eV) semiconductor. Whereas other polymorphic forms of MoS_2 are less explored experimentally, which may potentially limit or enhance the application of 2D MoS_2 devices by its presence within 1H-MoS_2 samples. It has been assumed that metastable phase is the 1T phase and it is metallic in nature [112, 122, 133–135]. Due to its metallic nature, 1T-MoS_2 is considered suitable for novel devices such as *i.e* supercapacitors [133], catalyst for hydrogen evolution reaction [134], ultrathin transistors [135].

In this section, we used self-energy corrected first-principles calculations to determine the electronic nature of metastable form present in the experimental samples synthesized by Prof. D. D. Sarma's group, IISc.

4.2.2 Computational Details

We have used first-principles calculations based on density functional theory as implemented in Vienna ab initio package (VASP) [136, 137]. Core and valence electrons are treated using the projected-augmented wave (PAW) method [138, 139]. We

used the GW version of PAW potentials available with VASP, which are expected to provide improved scattering properties at higher energies [140]. The exchange-correlation of electrons is treated using a generalized gradient approximation with functional parameterized by Perdew, Burke, and Ernzerhof (PBE) [36]. We use an energy cutoff of 380 eV to truncate the plane wave basis used in representing Kohn-Sham wave functions. We relaxed the structures to minimize energy until the Hellman-Feynman force on each atom is less than 0.01 eV/Å. We have used a periodic supercell to simulate a 2D MoS_2 sheet, with a vacuum of 10 Å to separate the periodic images. Integrations over the Brillouin zone (BZ) were sampled on 24x24x1 and 12x24x1 uniform meshes of k-points (Γ-centered) for 2H and 1T′ (2axa) respectively. Converged PBE eigenvalues and wave functions were used subsequently to calculate quasiparticle energies in the non-self-consistent GW (G0W0) approximation. DFT eigenvalues were corrected with electron self-energy obtained within a GW approximation. Calculations of RPA-based dielectric response function were carried out with energy cut-offs of 186.7 eV. We added 63, 126, 252, 189 empty conduction bands in G0W0 calculations of 1H, 1T′, 1T″ and 1T‴ structures respectively. We have performed some of the test calculations with exchange correlation energy functional treated within the framework of a local density approximation (LDA) and Hubbard U parameter of 1 eV to include on-site correlations of d-electrons of Mo atom, which constitute the valence and conduction bands lining the gap.

4.2.3 Results and Discussion

The crystal structure of metastable patches of MoS_2 was originally proposed to be of 1T form with an ideal octahedral configuration [122, 141]. However, some of the X-ray diffraction and STM based investigation show that chemical exfoliation of MoS_2 leads to formation of distorted 1T″ structure with 2ax2a superstructure [142, 143] involving tetramerization of Mo atoms (Figure 4.9). The 1T′ structure with a zigzag

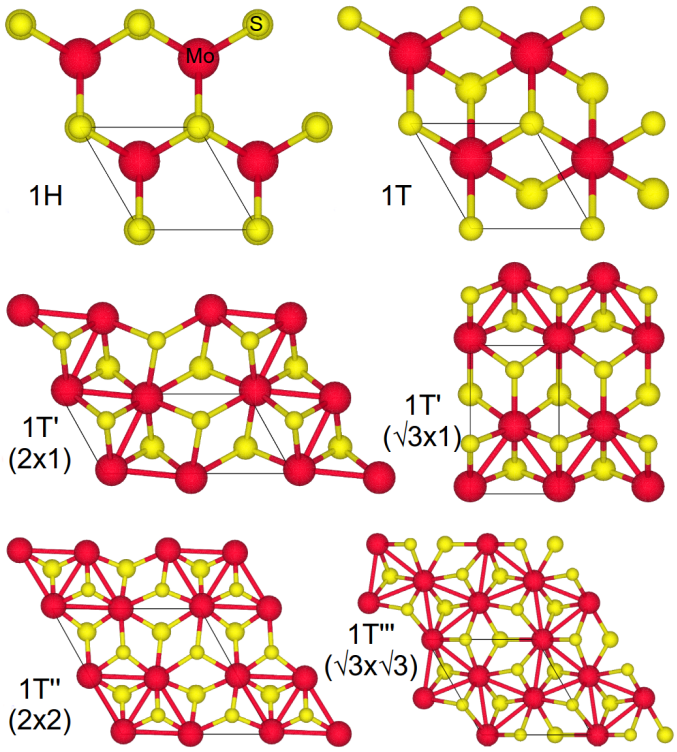

Figure 4.9: Top view of different forms of MoS_2 1H, 1T and various distorted 1T structures (1T′, 1T″ and 1T‴). 1T′ can be described in terms of two different unit cells corresponding to 2axa and $\sqrt{3}$axa superstructures, while 1T″ and 1T‴ correspond to 2ax2a and $\sqrt{3}$ax$\sqrt{3}$a superstructures obtained by trigonal 1T MoS_2 distortion. The unit cells are enclosed by solid lines.

chain-like clustering of Mo atoms or dimerization of Mo atoms [116, 144] is observed using transmission electron microscopy (TEM). Some groups have reported that the oxidation of MoS_2 leads to formation of 1T‴ ($\sqrt{3} \times \sqrt{3}$ superstructure) with trimerization of Mo atoms (see Figure 4.9). The electronic structure of these structural forms depend on their structure such as centrosymmetric-1T is metallic whereas 1T′, 1T″ and 1T‴ known as distorted 1T-forms are semiconductor with a gap of 90 meV, 200 meV and 500 meV respectively. Based on total energy calculations, it is difficult to find most stable 1T structural form as 1T′ and 1T″ MoS_2 are degenerate in energy. The energy difference of these structural form is 4 meV/f.u. which is within the error limits of DFT.

Photoemission spectroscopy (PES) is the only direct method to probe electronic structure experimentally. It is well known that density functional theory (DFT) is ill equipped to describe photoemission as the Kohn-Sham energies do not formally correspond to quasiparticle energies, which are required to correctly describe electron addition or removal events [145]. A widely-employed and efficient means to overcome this problem is the GW approximation [140, 146–148], which goes beyond the mean-field, independent-particle DFT approach and properly accounts for many-body electron-electron interactions. Therefore, this quasiparticle picture is generally sufficient to obtain accurate photoemission spectra. Hence, we have calculated electronic structure of MoS_2 in 1T forms within GW approximation and compared it with PES valence band spectra to find out which structural form is present in the experimental sample and it's nature (semiconducting or metallic).

We compared the calculated density of states of 1H phase with the valence band spectrum of 1H phase obtained experimentally. Due to hybridized Mo $4d$ and S $3p$ states, there are features appearing at 1.8, 3.3, 5.2 and 6.5 eV in valence band spectrum of 1H MoS_2 (Figure 4.10a). To compare the calculated DOS to the experimental spectrum, experimentalist took into account the relative cross-sectio of Mo $4d$ and S $3p$ states at the photon energy used. The sum of these cross-section weighted partial DoS after broadening with a Lorentzian with an energy dependent width and a Gaussian of fixed width to account for the life-time and resolution broadening (see Figure 4.10a). The agreement between the calculated and experimentally obtained spectrum is remarkable (refer 4.10a), establishing the potency of the GW calculation scheme in capturing the electronic structure of MoS_2. Calculated results based on local density approximation (LDA) with and without spin-orbit coupling did not provide an accurate description of our experimental results, significantly underestimating the energy separation between Mo $4d$ and S $3p$ dominant peaks observed at 1.8 and 3.3 eV. We have also checked the inclusion of on-site Coulomb

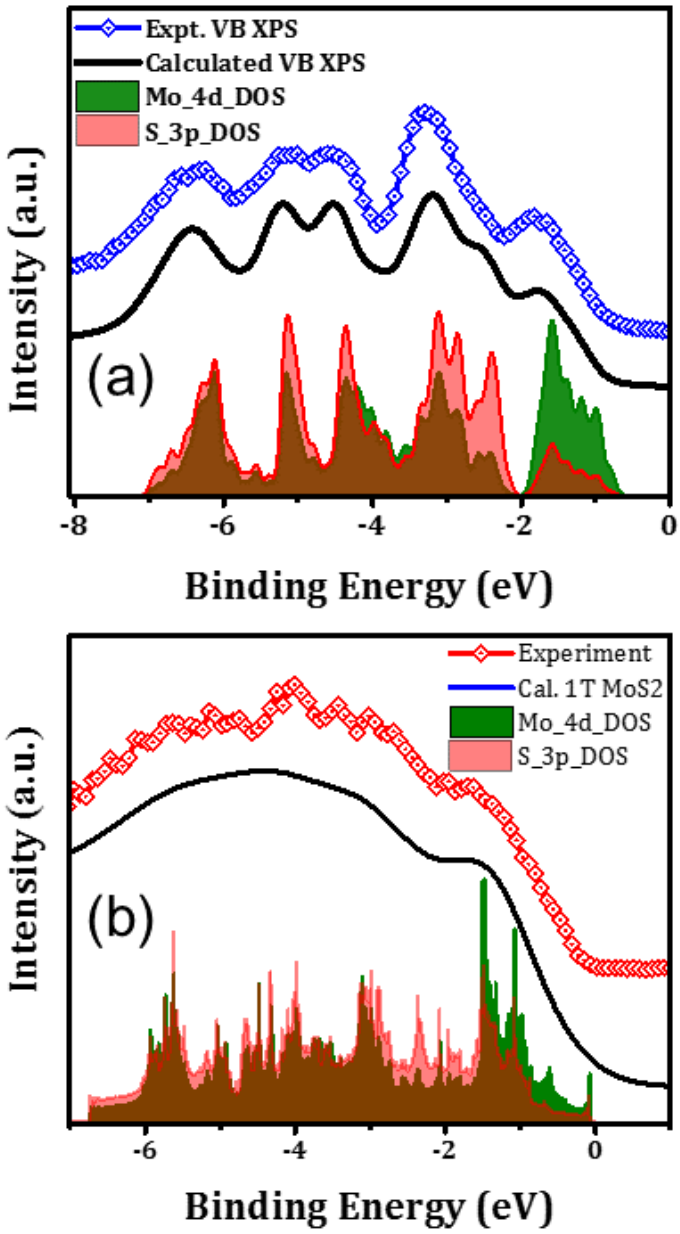

Figure 4.10: (a) Experimental (open circle) and calculated (solid line) valence band spectra of pure 1H sample along with partial density of states of Mo $4d$ and S $3p$. (b) Experimentally obtained spectral features of the metastable phase (open circle) compared with that obtained from the calculation of the electronic structure of the metastable 1T′ phase of MoS_2 (solid line) along with partial density of states of Mo $4d$ and S $3p$.

interaction of Mo $4d$ states within the LDA+U approach, which even worsen the agreement with experimental data. We have compared the valence band spectrum

of metastable patches obtained experimentally with 1T′, 1T″ and 1T‴ DoS (refer Figure 4.10b) and find that the metastable MoS_2 phase generated by the chemical exfoliation of 1H MoS_2 is a semiconductor (1T′) with a gap $\sim$ 90 meV in contrast to the assumption of it being the metallic 1T phase.

4.2.4 Conclusions

We unravel the mystery of precise atomic and electronic structures of the 1T phase of 2D MoS_2, which is known to have properties that are relevant to its applications. This meta-stable phase is known to occur in nano-scale regions of commonly grown samples of 2D MoS_2. Self-energy corrected first-principles calculations of electronicstructure to determine its electronic nature, which along with the experiments by Prof. D. D. Sarma show that 1T phaseof 2-D MoS2 has a $2a \times a$ super-structure with Mo dimerization, and exhibits a band-gap of 90 meV.

4.3 Superior performance of 1T-$MoSe_2$ in visible light induced hydrogen evolution reaction[†]

4.3.1 Introduction

The global energy crisis, which results from exponentially increasing energy demands and harvesting of nonrenewable energy resources in unsystematic way, has befallen mankind. In pursuit of renewable and environmentally friendly energy sources, much research has been conducted to achieve energy sustainability. Superior energy density, sustainable energy production techniques proposed hydrogen as a feasible storage and source of green energy. To this end, efficient catalysts are required for the hydrogen evolution reaction (HER), where protons from solution combine with

[†]A part of this work has been published in *APL Materials*, 2014 [99]. Reproduced by permission of Creative Commons Attribution, URL: *http* : *//dx.doi.org*/10.1063/1.4892976.

electrons at the electrode to form H_2 gas. The expensive Pt-group metals are still the most active catalysts for HER, so efficient, abundant, and low-cost alternatives are needed. Hence, alternatives to Pt have been suggested; of these, a class of materials that features promising qualities, such as low cost and favorable energy barrier to hydrogen adsorption [149] is that of Group VI TMDCs. MoS_2 has been widely used as a catalyst for electrochemical, photo-electrochemical and photo-catalytic H_2 generation from water [150–152]. The metallic nature of 1T MoS_2 is expected to be responsible for H_2 evolution [115, 134, 153]. 2H-$MoTe_2$ with an indirect bandgap of 1.05 eV has its conduction band minimum at 0.37 eV higher than 1H-MoS_2, and well above the water reduction potential [154,155], making it an ideal catalyst for H_2 evolution. The 1T form of $MoSe_2$ is also metallic and could be expected to be better catalyst than its 2H analogue for water reduction. In this section, we explain that why $MoSe_2$ has superior catalytic activity compared to MoS_2 in both 1H and 1T structures towards hydrogen evolution reaction (HER) as observed in experiments by Prof. CNR Rao.

4.3.2 Computational Details

We have used first-principles calculations based on density functional theory (DFT) as implemented in Quantum ESPRESSO package [41], in which the ionic and core-valence electron interactions are modeled with ultrasoft pseudopotentials [40]. The exchange-correlation energy of electrons is treated within a Generalized Gradient Approximation (GGA) functional as parametrized by Perdew, Burke and Ernzerhof (1996) [36]. We use an energy cutoff of 35 Ry to truncate the plane wave basis used in representing Kohn-Sham wave functions, and energy cutoff of 280 Ry to represent charge density. Structures are relaxed till the Hellman-Feynman forces on each atom are less than 0.02 eV/Å. We have used a periodic supercell geometry to simulate a 2D sheet, including vacuum of 15 Å to separate the adjacent periodic images of the

sheet. In self-consistent Kohn-Sham (KS) calculations of configurations of with 1x1, $\sqrt{3}$x$\sqrt{3}$ and $\sqrt{3}$x1 supercells, the Brillouin zone (BZ) integrations are sampled over uniform meshes of 21x21x1, 7x7x1 and 12x7x1 k-points respectively.

Since KS-DFT typically underestimates electronic band gaps (a known limitation), we employ hybrid functional based on Hartree-Fock-Exchange (HSE) [46] with screened Coulomb potential to estimate band gaps more accurately. These calculations are based on first-principles DFT using Projector Augmented Wave (PAW) method [138,139] as implemented in the VASP (Vienna Ab-initio Simulations Package) [136,137].

4.3.3 Results and Discussion

Experimental results show that the catalytic activity of the 1T form of $MoSe_2$ is nearly few hundred times higher than that of the 2H form. Interestingly, the yield of H_2 and turn on frequencies (TOF) with 1T-$MoSe_2$ is superior even to those found with 1T MoS_2. The 1H form of $MoSe_2$ too shows better activity than that of 2H MoS_2 (yield of 0.05 $mmolg^{-1}h^{-1}$ and TOF of 0.008 h^{-1}). For more details of experimental results, refer Gupta *et al.*, APL Materials **2**, 092802 (2014) [99].

1T structure with 1x1 periodic cell is metallic [4,5]. We have studied two superstructures of 1T-MoX_2 (where X = S and Se), $\sqrt{3}$x$\sqrt{3}$ and $\sqrt{3}$x1 [156] (see Figure 4.9). Amongst these two superstructures, $\sqrt{3}$x1 is metallic and shows dimerization of Mo atoms, and $\sqrt{3}$x$\sqrt{3}$ is semiconducting with trimerized Mo atoms. From the calculated phonon dispersion, we find that both MoS_2 and $MoSe_2$ are stable (structures are at local minima of energy) in the $\sqrt{3}$x$\sqrt{3}$ and $\sqrt{3}$x1 superstructures as shown is Section 4.1. However, $\sqrt{3}$x$\sqrt{3}$ structure of 1T-MoS_2 is energetically more stable than the $\sqrt{3}$x1 by 27 meV/f.u., while the $\sqrt{3}$x1 super-structure of $MoSe_2$ is energetically more stable than the $\sqrt{3}$x$\sqrt{3}$ super-structure by 33 meV/f.u. Experimentally, $MoSe_2$ is indeed seen to be in $\sqrt{3}$x1 super-structure [99], in agreement

with our first-principles results. In the further analysis, we consider the $\sqrt{3}$x$\sqrt{3}$ superstructure for MoS_2 and $\sqrt{3}$x1 superstructure for $MoSe_2$.

To determine the efficiency of MoX_2 (X= S, Se) in reducing a proton to hydrogen as observed in experiments here, we have estimated their electron affinities (EA) and work function (ϕ). For the metallic states, the relevant property here is the work function. The work function is calculated as $\phi = E_{vac}$ - E_F, where E_F is the Fermi energy. For semiconductors, the EA is estimated as the difference between the vacuum potential (E_{vac}) and the lowest energy conduction band (E_{CB}). As DFT is a ground state theory, estimation of band gap and hence of the location of CB, E_{CB} is not accurate. We replace the E_{CB} with E_{VB} + E_g, where E_{VB} is the energy of the highest valance band (occupied states) and E_g is the band gap. We use the HSE corrections (using VASP) to determine E_g accurately. For the monolayered MoS_2, experimental value of electronic bandgap (1.8 eV [114]) is available. Comparison of the experimental bandgap with our estimates of bandgaps for 2H-MoS_2 reveals that Kohn-Sham bandgap is underestimated by 7.2%, while HSE bandgap is overestimated by 17.7% (see Table 4.6), the latter is in agreement with Ahuja *et al.* [157]. Thus it is clear that the HSE method overestimates the experimental bandgap of 2H-MoS_2, whereas KS-DFT calculation (GGA) yields a better estimation, and we use estimates of E_g obtained from KS-DFT calculations in this work.

We find that the 2H and 1T-polytypes of MoS_2 have a greater work function than that of the respective structure of $MoSe_2$ (refer to Table 4.7). Thus, it is easier to extract an electron from $MoSe_2$ as compared to that from MoS_2 in both 1T and 2H polytypes. Secondly the 1T polytype has a lower work function than the 2H, which means that its easier for the 1T polytype to donate electron as compared to the 2H-structure. This explains why 1T-polytype of $MoSe_2$ is more effective in producing hydrogen than the 2H-polytype as observed in experiments. Electron affinities of

both 1T and 2H polytypes (see Table 4.7) indicate that MoS_2 has a stronger electron affinity (indicating a higher tendency to attract electrons) than that of $MoSe_2$, but its work function is also larger. Thus, though MoS_2 more readily attracts/accepts electrons, it does not donate it easily. Hence, $MoSe_2$ is more efficient in hydrogen evolution as compared to that of MoS_2 as observed in experiments here.

Table 4.6: Calculated and experimental values of bandgaps for 2H and 1T ($\sqrt{3}$x$\sqrt{3}$ superstructure) structures of MoX_2. HSE and KS-DFT bandgaps are calculated using VASP.

Compounds	Bandgap (eV)		
	KS-DFT (VASP)	HSE (VASP)	Exp.
2H-MoS_2	1.67	2.12	1.8 [114]
2H-$MoSe_2$	1.45	1.88	–
1T-MoS_2 ($\sqrt{3}$x$\sqrt{3}$)	0.76	1.28	–
1T-$MoSe_2$ ($\sqrt{3}$x$\sqrt{3}$)	0.64	1.16	–

Table 4.7: Calculated values of electron affinity (EA) and work function (WF) for 1T (for both $\sqrt{3}$x$\sqrt{3}$ and $\sqrt{3}$x1 superstructures) and 2H structures of MoX_2 (MoS_2 and $MoSe_2$)

	1T-form				2H-form	
Superstructure	$\sqrt{3}$ x $\sqrt{3}$		$\sqrt{3}$ x 1		–	
Compound	MoS_2	$MoSe_2$	MoS_2	$MoSe_2$	MoS_2	$MoSe_2$
EA(eV)	4.95	4.42	–	–	4.22	3.78
WF(eV)	5.68	5.20	5.63	5.00	5.86	5.35

In addition, we have determined the energy of binding of hydrogen (H) to $\sqrt{3}$x1 *1T* superstructure of MoS_2 and $MoSe_2$, which is relevant to the experiments reported here and has the lowest work function. The hydrogen binding energy is calculated as

$$E_{ads} = \frac{1}{n}[E(slab + nH) - E(slab) - \frac{n}{2}E(H_2)], \tag{4.4}$$

where n is the number of H atoms considered in the simulation. We find that bulk metal dichalcogenides (MoS_2 and $MoSe_2$) do not absorb hydrogen ($E_{ads} > 0$).

However, it has been previously reported that their edges are catalytically active in hydrogen adsorption [153]. Hence, we have simulated ribbons of MoX_2 with two different types of edges (Mo terminated edge and X terminated edge) and their interaction with H (with 100% hydrogen coverage at the edges). The hydrogen binding energies at Mo sites at the edges of MoS_2 and $MoSe_2$ are -33.8 meV/f.u. and -32.3 meV/f.u. respectively. The respective Mo-H bond lengths are 1.72 Å and 1.73 Å. Whereas, the hydrogen binding energies at the X (S/Se) edges of MoS_2 and $MoSe_2$ are -34.6 meV/f.u. and -13.1 meV/f.u. respectively. The corresponding X-H bond lengths are 1.35 Å and 1.48 Å. The binding energy of hydrogen at the metal edge is about the same in the two compounds but the Se edge shows weaker binding with hydrogen than of the S edge. According to the volcano plot [158], this suggests a higher exchange current for hydrogen evolution over $MoSe_2$ than that over MoS_2, consistent with our analysis based on the work functions. Since $MoSe_2$ has a lower work function than of MoS_2, its Fermi energy (E_F) lies closer to the normal hydrogen electrode (E_{NHE}), which makes easy exchange of an electron with $MoSe_2$ (H atom has a weaker binding at Se edge) as compared to MoS_2. Hence, $MoSe_2$ is relatively more efficient in facilitating hydrogen evolution reaction.

4.3.4 Conclusions

Our first-principles analysis reveals that (a) $MoSe_2$ has a lower work function in each of the 1T and 2H structures as compared to MoS_2, and (b) 1T-structure exhibits lower work function than the 2H-structure for each MoX_2 (X= S and Se). This results in easy transfer of electron from the $MoSe_2$ substrate to reduce proton, and hence $MoSe_2$ is more efficient for hydrogen evolution reaction as compared to MoS_2, which is also reflected in our analysis of binding energies of H at $MoSe_2$ edges.

Chapter 5

Properties of 2H-$MoTe_2$: Effect of pressure and Te-vacancies

5.1 Pressure-dependent phase transition in 2H-$MoTe_2$

5.1.1 Introduction

The electronic topological transition [161, 162] or Lifshitz [163] transition are observed when the van Hove singularity associated with the band extrema approaches the Fermi level and passes through it. It effects the distribution of carriers and hence changes the Fermi surface topology. The minute changes in the electronic band and Fermi surface topology is caused by external parameters, that can be reflected in the anomalies of the measurable quantities and, are mainly of two types: (a) the appearance or disappearance of electron and hole pockets, and (b) the rupturing of necks connecting Fermi-arcs. In this work, we observe Lifshitz transition due to the appearance or disappearance of electron and hole pockets. Raman studies have

been shown to be useful to capture the phonon signatures associated with the subtle modifications in the Fermi surface topology, evident in the changes in pressure coefficients [164] or in the integrated area ratios [165] of the Raman modes.

Mechanical deformation or strain is one of the way to switch among different thermodynamically stable structural polytypes for TMDCs without adding impurities. According to recent studies on high pressure Raman of 2H-MoS_2 [159, 160], a lateral shift of adjacent S-Mo-S layers around $\sim$ 20 GPa is observed. This phase is a mixed phase of $2H_c$ (2H) and $2H_a$ (1T) structures with the $2H_c$-phase being the dominant one [159], hence changes the pressure coefficients of Raman modes [159]. A metallic phase appears at $\sim$ 40 GPa [159], as a result of completion of layer sliding transition from $2H_c$ to $2H_a$. In this section, we are interested to study the effect of external pressure on electronic and vibrational properties of 2H-$MoTe_2$.

In the section 5.1, we present Raman studies of bulk 2H-$MoTe_2$ as a function of pressure. Experiments by Prof. A. K. Sood's group show considerable change in the pressure coefficients of the frequencies of first order (E_{2g} and A_{1g}) phonon modes at $\sim$ 6 GPa. This transition is identified as semiconductor to semimetal as shown by first-principles study. Experimentally, a decrease of pressure coefficient of the A_{1g} mode from 2.2 to 1.7 cm^{-1}/GPa around $\sim$ 16.5 GPa is observed. Theoretically, this transition is marked as Lifshifz transition. Our theoretical calculations confirm that there is no structural transition in 2H-$MoTe_2$ throughout the whole pressure range upto 30 GPa. This is consistent with Raman experiments, where no new Raman modes appeared for a lower symmetry structure [166]. Our findings is quite similar to the cousin material $MoSe_2$, where no structural transition is observed upto the maximum pressure of $\sim$ 60 GPa and it shows a metallic nature around 41 GPa [167]. Pressure dependent Raman experiments of 2H-$MoTe_2$ presented in the Section 5.1, are performed by Prof. A. K. Sood's group (IISc).

5.1.2 Computational Details

Our first-principles calculations are based on density functional theory as implemented in Quantum ESPRESSO package [41], in which the interaction between ionic core and valence electrons is modelled by norm-conserving pseudopotentials [168, 169]. The exchange-correlation energy of electrons is treated within a Local Density Approximation (LDA) with a functional form parametrized by Perdew-Zunger [37]. We use an energy cutoff of 80 Ry to truncate the plane wave basis used in representing Kohn-Sham wave functions, and energy cutoff of 320 Ry for the basis set to represent charge density. Self-consistent solutrion to the Kohn-Sham equations was obtained until the total energy converges numerically to less than 10^{-8} Ry. Structures are relaxed to minimize the energy till the magnitude of Hellman-Feynman force on each atom is less than 0.001 Ry/bohr. We include van der Waals (vdW) interaction with the parametrization given in Grimme scheme [56]. In self-consistent Kohn-Sham (KS) calculations of configurations of bulk 2H-$MoTe_2$ unit cell, the Brillouin zone (BZ) integrations are sampled on 12x12x3 and 24x24x6 uniform meshes of k-points in determination of total energy and electron-phonon coupling respectively. For bulk 2H-$MoTe_2$ at zero pressure, we determine electronic structure by including the spin-orbit coupling (SOC) through use of relativistic pseudopotentials using a second variational procedure [170]. Phonon and dynamical matrices at Γ-point (q= (0, 0, 0)) were determined using density functional linear response as implemented in Quantum ESPRESSO(QE) [41], which employs the Green's function method to avoid explicit use of unoccupied Khon-Sham states. Since DFT typically underestimates the bandgap, we have used HSE functional as implemented in QE to estimate the gaps accurately. The mixing parameter is equal to 0.15 in these calculations. The reciprocal space integration is performed using 108 k-points in each direction for a 6x6x3 uniform mesh.

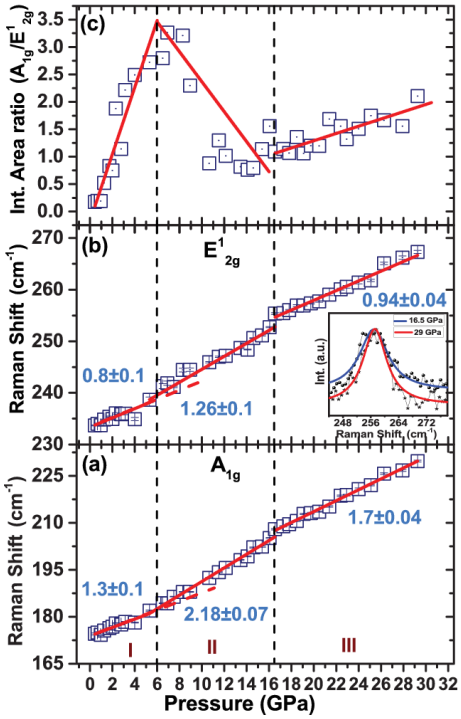

Figure 5.1: The phonon frequencies of (a) A_{1g}, (b) E^1_{2g} and (c) the integrated area ratio of A_{1g} to E^1_{2g} versus pressure plot. The solid lines are linear fits $[\omega_p = \omega_0 + (\frac{d\omega}{dP})P]$ to the observed frequencies (solid symbols) and the corresponding slope values are shown. The inset of (b) shows Raman spectra at P= 16.5 and 29 GPa, where the spectra are laterally shifted to match the frequency and also normalized. Error bars (obtained from the fitting procedure) are also shown. The black dashed lines mark the phase transitions and the red dashed lines are guide to the eye.

5.1.3 Experimental Observations

In this subsection, we show the experimental results obtained by Prof. A. K. Sood's group on pressure dependent Raman experiments of 2H-$MoTe_2$. The Raman measurements show a change in slope (S= dω/dP) (Figures 5.1a, b) of the phonon modes A_{1g} and E^1_{2g} at $\sim$ 6 GPa. The change in S across the transition pressure for the out-of-plane A_{1g} mode (0.9 cm^{-1}/GPa) is about twice that of the in-plane E^1_{2g} mode (0.4 cm^{-1}/GPa)(see Figure 5.1c). We also observe a maximum in the integrated area ratio of the A_{1g} mode to the E^1_{2g} mode around 6 GPa (see Figure 5.1c). They also suggests another transition at $\sim$ 16.5 GPa (Figure 5.1c). Across this pressure

range, the value of S for the A_{1g} mode and E^1_{2g} mode decreases. We are interested to understand the orgin of these anomalies observed in phonons with pressure.

5.1.4 Atomic and electronic structure

The structure of 2H-$MoTe_2$ consists of layers Te-Mo-Te, with a unit cell characterized by a stacking sequence AbABaB, where A, B label Te atomic layers and a,b label Mo atomic layers with triangular lattices (see Figure 5.2a). 2H-$MoTe_2$ is an indirect band gap semiconductor with valence band maximum (VBM) at Γ and conduction band minimum (CBM) at K_2 point (K_2 point is a mid point of Γ-K path) with a gap 0.57 eV (refer to Figure 5.2b). The VBM and CBM constitute of 4d orbital of Mo and 5p orbital of Te (see Figure 5.2c). Inclusion of the SOC reduces the indirect gap by 30 meV. The splitting of bands due to SOC is relatively smaller at Γ point than at K and M points. Since the change in band gap due to inclusion of SOC is small, we have not included the SOC in pressure dependent studies.

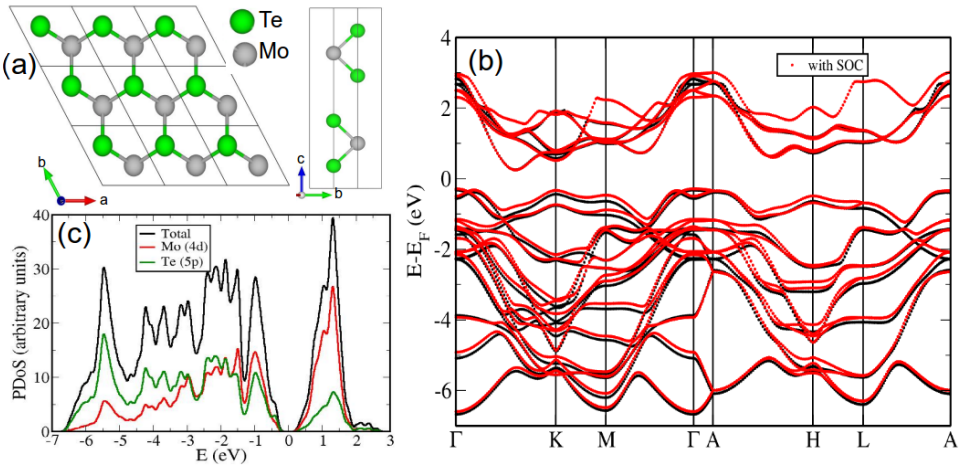

Figure 5.2: (a) Crystal structure, (b) electronic structure and (c) projected density of states of 2H-$MoTe_2$. Electronic structure determined with (red color lines) and without (black color lines) effects of the spin-orbit coupling (SOC); the effect of SOC are particularly evident in the states lining the gap.

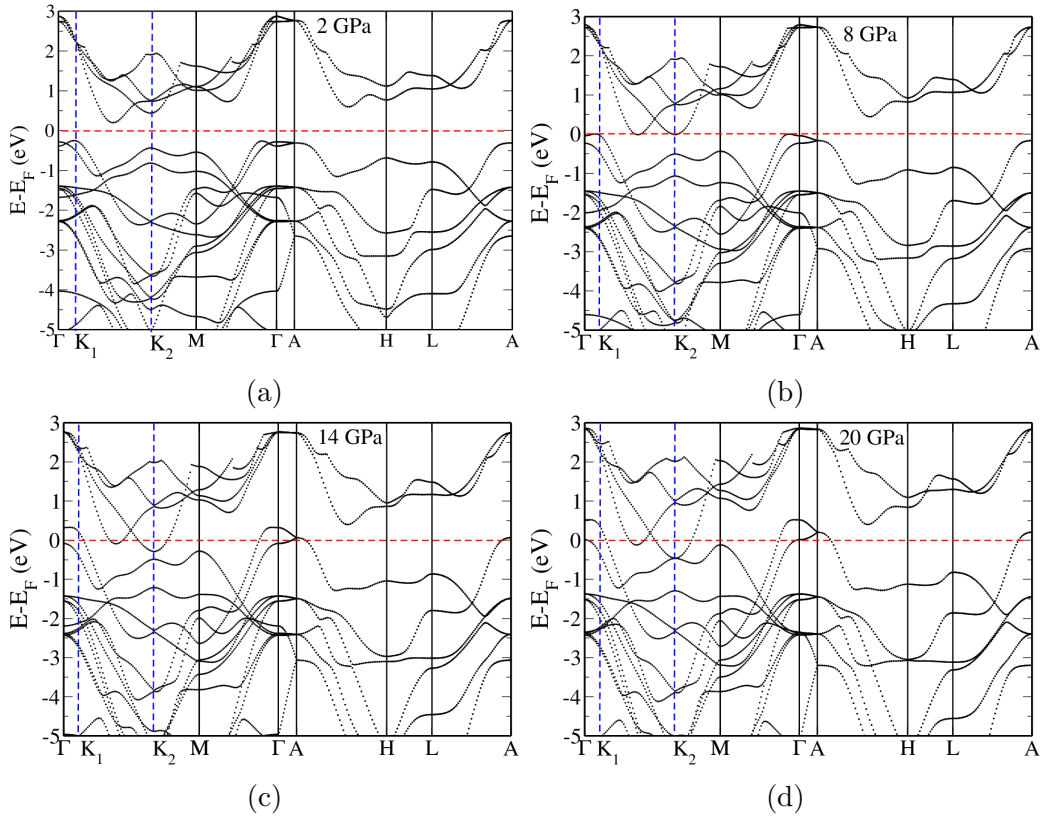

Figure 5.3: Electronic structure of 2H-$MoTe_2$ at (a) 2 GPa, (b) 8 GPa, (c) 14 GPa, (d) 20 GPa.

5.1.5 Pressure dependent electronic transitions

We present theoretical calculations to understand the two transitions at 6 GPa and 24 GPa observed in the experiments. We find that the structure of 2H-$MoTe_2$ remains stable upto the highest pressure, but its indirect band gap reduces and VBM shifts to K_1 point (q= (1/14, 1/14, 0), near Γ-point) (see Figure 5.3a). We clearly observe (see Figure 5.4b) that the VBM (at K_1-point) and the CBM (at K_2-points) cross the Fermi level at 8 GPa. In addition, the CBM at K-point and VBM at Γ-point also cross Fermi level (see Figures 5.3b, 5.4a and 5.4c). At 8 GPa, there are very few states at the Fermi level and hence $MoTe_2$ is semi-metallic, in agreement with the previous calculations [171]. At 8 GPa, the indirect band gap with VBM at K_1 and CBM at K_2 (mid point of Γ-K path) as well as at K-point (see Figure 5.3b) closes. We note that

Rifliková et al [171] have predicted semiconductor to metallic transition in between 10 to 13 GPa. The inclusion of van der Waal's interactions in our calculations perhaps result in reduction of the predicted transition pressure. The transition observed in our experiment at $\sim$ 6 GPa which is identified as a semiconductor to semimetal transition, is seen to occur at 8 GPa in our calculations. This difference between the observed and calculated transition pressures is partly due to errors in the calculated equilibrium lattice constants.

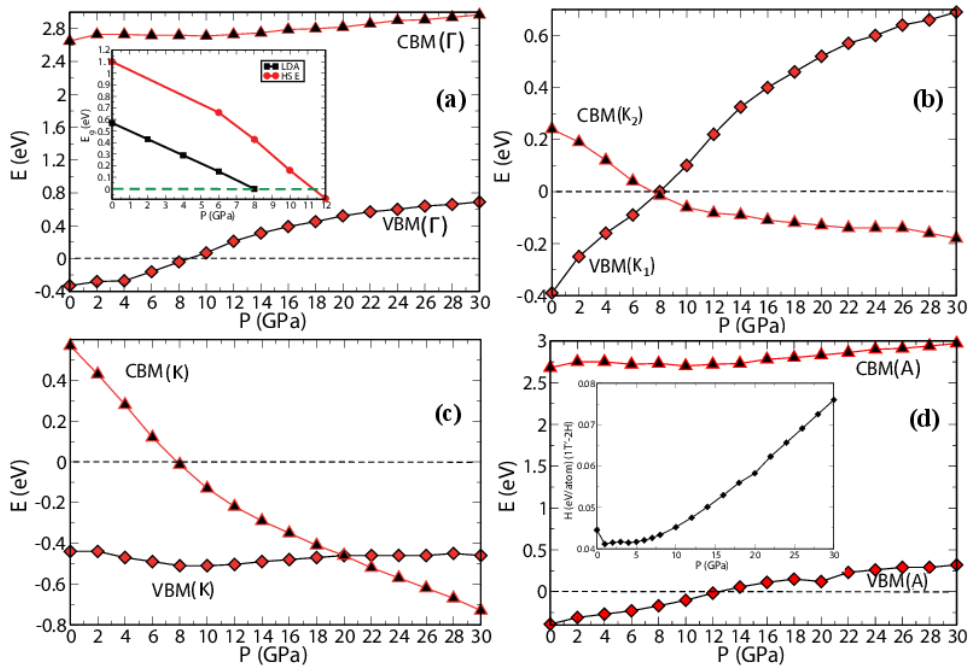

Figure 5.4: Variation in VBM and CBM with pressure at different high symmetry points of BZ (a) Γ, (b) K_1(VBM; near Γ point), K_2 (CBM; mid point of Γ-K path), (c) K and (d) A point. The inset in (a) shows the estimates of band gaps with HSE and LDA functionals with pressure. The difference in enthalpy of 2H and 1T′-$MoTe_2$ with pressure is shown in inset of (a). Note that 2H-$MoTe_2$ stability increases with pressure.

Furthermore, we determine the band gap of $MoTe_2$ using HSE calculations to estimate the accurate transition pressure of semiconductor to semimetal transition. The HSE based estimates of the band gap at 0 GPa is 1.1 eV, while the gap estimated with LDA is 0.57 eV. We note that the former is in good agreement with experiment at P = 0 GPa, whereas the latter is an underestimate by 0.4 eV, with respect to

the experimental value (1.1 eV). Thus, the pressure of semiconductor to semimetal transition is expected to be underestimated with LDA calculation. P_c obtained with HSE calculation is 12 GPa (see inset of Figure 5.4a). However, this is expected to be also off-set by the errors in the lattice constants calculated by LDA, and a precise comparison of these results with experiment on this anisotropic materials is tricky. The motivation behind our calculations is to understand the nature of transition rather than predicting the precise transition pressure, and the link demonstrated between the Raman anomaly and the electronic transition is physically reasonable.

An increase in the pressure beyond 8 GPa creates new extrema in electronic dispersion with electron pockets (valleys) at K_2 and K points, and hole pockets at Γ and A points (see Figure 5.3c). This emergence of hole and electron pockets seen clearly in Figures 5.4a, b and d where the VBMs at Γ, K_1 and A points cross Fermi level at 10 GPa, 8 GPa and 12 GPa respectively, leading to formation of hole pockets. Similarly, CBMs at K_2 at 8 GPa and K points at 20 GPa cross Fermi level leading to the formation of electron pockets. As the hydrostatic pressure does not alter the symmetry of the crystal, energy levels do not split, but those near the Fermi energy change notably giving rise to pressure induced transfer of electrons from one pocket to another in order to maintain the number of carriers. Interestingly at 20 GPa, the gap at K-point closes (see Figure 5.4c), which within errors of our calculation, corresponds to the second transition experimentally seen at 16.5 GPa. To probe this further, we monitored the evolution of Fermi surface with pressure. At 20 GPa, we visualize Fermi surfaces associated with all the bands which cross Fermi level and find electron pockets at K-point and at K_2 along the path Γ to K (see Figure 5.5a, green color surfaces). In Figure 5.5a (red and blue surfaces), at Γ and A points, we observe hole pockets (see Figures 5.3a and d). We find the Fermi surface associated with the bands at Γ and A points changes significantly at pressure of $\sim$ 20 GPa (see Figures 5.5b-d). Since, the Fermi surface changes with applied pressure

without breaking the structural symmetry, we assign a Lifshitz transition at $\sim$ 20 GPa.

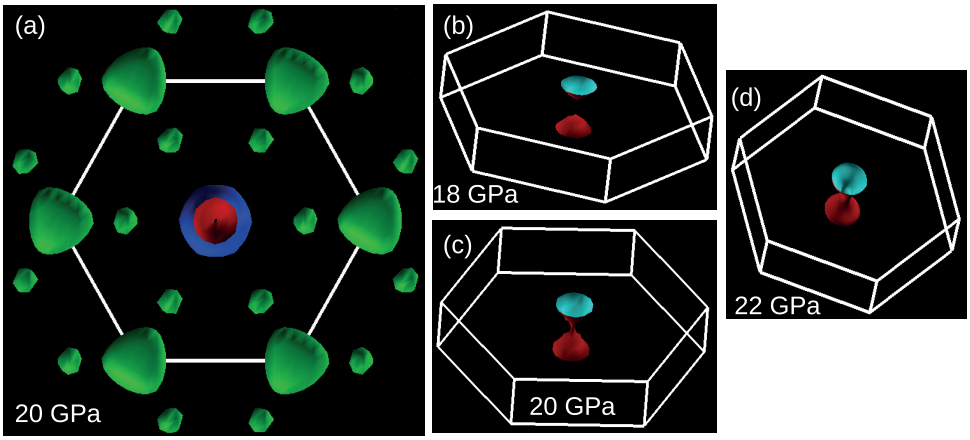

Figure 5.5: Fermi surfaces at (a) 20 GPa of merged bands (all the bands crossing the Fermi levels). Panels (b), (c) and (d) show the specific hole like part of Fermi surface changing with pressure at P= 18 GPa, 20 GPa and 22 GPa respectively. Note that (b), (c) and (d) show the hole pockets at Γ and A points with pressure. Green color shows electron pockets whereas blue and red (at the center of the hexagon) show hole pockets.

5.1.6 Investigation of structural phase transition from 2H to 1T′ phase

To investigate the pressure dependent phase transition from 2H to 1T′ phases of $MoTe_2$, we study the changes in enthalpy of these structures, and did not observe any phase transition from 2H to 1T′ phase. In fact, $MoTe_2$ in 2H form indicates increased stability with pressure (inset of Figure 5.4d). We investigated the phase transition only between 2H and 1T′ phase as 1T′ is the phase that is second lowest in energy. The energies of 1T′-$MoTe_2$ and 1T-$MoTe_2$ are 133 meV/f.u. and 544 meV/f.u. with respect to 2H-$MoTe_2$, respectively. 1T-$MoTe_2$ is also locally unstable and exhibit structural instabilities with imaginary frequencies at K and M-points of BZ whereas $MoTe_2$ is stable in the 1T′ form. The 1T′ phase has a monoclinic lattice which is a distorted form of 1T phase. However, this structural distortion of

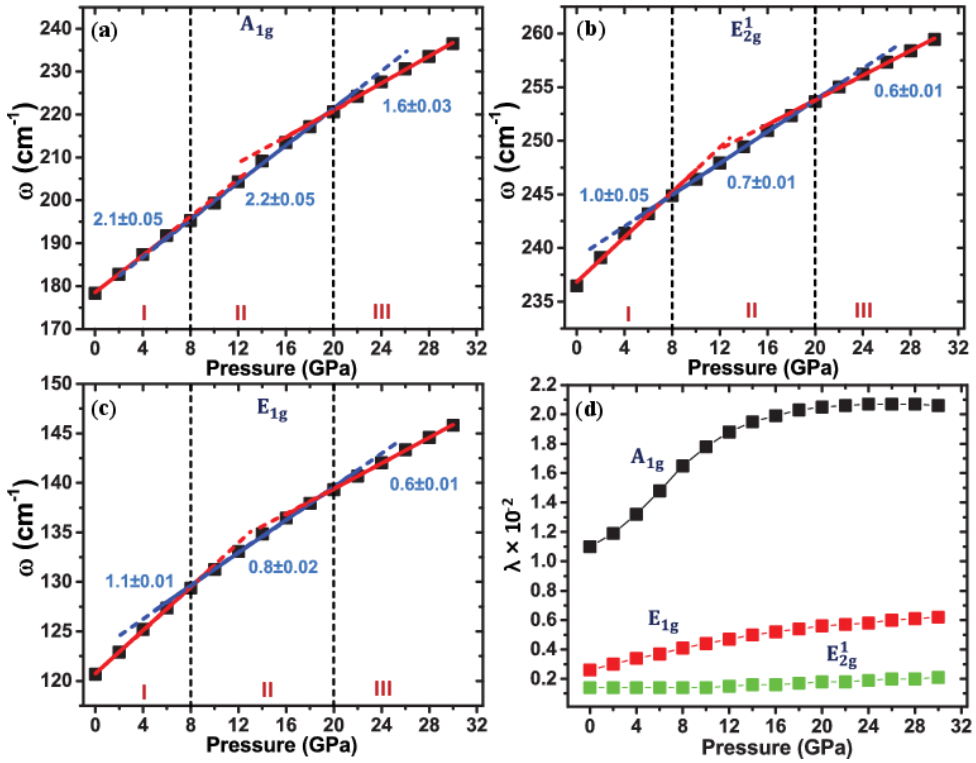

Figure 5.6: The pressure coefficients of Raman active phonon modes obtained using first-principles calculations. Changes in slopes (expressed in cm^{-1}/GPa) of A_{1g}, E^1_{2g} and E_{1g} are shown by vertical dashed lines in (a), (b) and (c) respectively. The changes in electron-phonon coupling of those modes are shown in (d).

1T phase results in formation of weak in-plane metal-metal bonds in the pseudo-hexagonal layers with zigzag metal chains [172].

5.1.7 Signatures of electronic transition in vibrational spectrum

The space group of 2H-$MoTe_2$ is D^4_{6h} with unit cell containing two formula units. The optically active modes at the BZ centre (Γ point) are classified into following irreducible representation as $A_{1g} + A_{2u} + B_{1u} + 2B_{2g} + E_{1g} + E_{1u} + 2E_{2g} + E_{2u}$. Out of these A_{2u} and E_{1u} modes are infrared active whereas A_{1g}, E_{1g} and E_{2g} modes are Raman active. We determined the effects of hydrostatic pressure on the Raman active modes. A compression of the unit cell leads to hardening of all the three

modes A_{1g}, E^1_{2g} and E_{1g} (see Figures 5.6a, b and c). Here, the calculated pressure coefficients for all the Raman modes decrease after the SMT except for A_{1g} mode, whereas the pressure coefficients for both the modes (A_{1g} and E^1_{2g}) increase (see Figure 5.6a and Figure 5.1a) in experiments. This increase in the pressure coefficient may be further amplified possibly due to chalcogen vacancies present in the system which can influence its properties notably [104, 173–175]. While the difference in the magnitude of slopes of A_{1g} of region I (0-6 GPa) and region II (6-16.5 GPa) in experiment is approximately 1 cm^{-1}/GPa (Figure 5.1a), it is underestimated in theory to be 0.1 cm^{-1}/GPa (Figure 5.6a). Similarly, we find difference in magnitudes of the calculated slopes of E_{1g} and E^1_{2g} from experimental slopes (see Figure 5.1 and Figure 5.6). To explain this, we have examined the effects of anharmonic interactions between phonons. We froze A_{1g} mode atomic displacements by 0.04 Å, and determined the changes in E^1_{2g} frequencies as a function of pressure. We find that the frequencies of E^1_{2g} mode change by approximately 12-13 cm^{-1}, revealing that there is a relatively strong coupling between A_{1g} and E^1_{2g} modes. This anharmonic (phonon-phonon) coupling is not included in our analysis, may be responsible for difference in the slopes of A_{1g} mode in region I and region II as a function of pressure in experiment and in theory.

We note that there are changes in slope ($= d\omega/\mathrm{dP}$) of pressure dependence of all the Raman active phonon modes at 8 GPa and 20 GPa (From Figure 5.6 a, b and c). A careful examination of the evolution of electronic structure with pressure indeed show the pressure induced semiconductor to semimetal transition at 8 GPa and a Lifshitz transition at 20 GPa. Thus, there is a clear correlation between the slope changes of Raman active modes and electronic phase transitions, obtained within the same theoretical framework. The electron-phonon coupling (EPC) of a phonon mode ν at wavevector q (frequency ω) is

$$\lambda_{\boldsymbol{q}\nu} = \frac{2}{\hbar\omega_{\boldsymbol{q}\nu}N(\epsilon_F)}\sum_{\boldsymbol{k}}\sum_{ij}|g^{\boldsymbol{q}\nu,ij}_{\boldsymbol{k}+\boldsymbol{q},\boldsymbol{k}}|^2 \times \delta(\epsilon_{\boldsymbol{k}+\boldsymbol{q},i}-\epsilon_F) \times \delta(\epsilon_{\boldsymbol{k},j}-\epsilon_F), \quad (5.1)$$

where $N(\epsilon_F)$ is the density of states at Fermi energy. The electron-phonon coupling matrix element is

$$g^{\boldsymbol{q}\nu,ij}_{\boldsymbol{k}+\boldsymbol{q},\boldsymbol{k}} = \left(\frac{\hbar}{2M\omega_{\boldsymbol{q}\nu}}\right)^{\frac{1}{2}}\langle\psi_{\boldsymbol{k}+\boldsymbol{q},i}|\triangle V_{\boldsymbol{q}\nu}|\psi_{\boldsymbol{k},j}\rangle, \quad (5.2)$$

where $\psi_{k,j}$ is electronic wavefunction of j^{th} band at wavevector k, M is the effective mass associated with the phonon, and $\triangle V_{\boldsymbol{q}\nu} = \frac{\partial V}{\partial u^{\nu}(q)}$ is the change in the self-consistent potential associated with atomic displacements of phonon qν.

Figure 5.6(d) shows that the A_{1g} mode couples more strongly with electrons than E_{1g} and E^1_{2g} modes (see Figure 5.6d). The size of electron pockets in the Fermi surface centered at K increases with pressure. This also can be understood with the help of group theoretical analysis of symmetry. The A_{1g} mode has symmetry of the crystal (an identity representation). The electron phonon coupling (EPC) of A_{1g} is large due to non-zero matrix element in Eq. 5.2 for the perturbation A_{1g} for all the electronic states. The EPC of A_{1g} increases with pressure and gets saturated above 20 GPa (refer to Figure 5.6d). This saturation of EPC can be a result of the gap closing at K-point at 20 GPa (Figure 5.3d). In contrast, E_{1g} and E^1_{2g} couples weakly as matrix element vanishes for E_{1g} and non-zero for a few of electronic states ($i.e.$ E_{1g}) for E^1_{2g}. Hence, we do not find any significant change in EPC with pressure for E_{1g} and E^1_{2g}.

Furthermore, to explain the non-monotonous change with a peak in relative intensity of A_{1g} and E^1_{2g} Raman modes (refer to Figure 5.1c) at the semiconductor to

semimetal transition (P= 6 GPa), we estimated Raman tensors using first-principles calculations. Raman scattering intensity is proportional to square of Raman tensor and defined as,

$$I \propto |e_i.R.e_s|^2, \tag{5.3}$$

where, $e_i(e_s)$ is the polarization of incident (scattered) radiation and R is the Raman tensor. Raman tensor is defined as,

$$R_{i\alpha\beta\gamma} = \frac{\partial Z^*_{i\alpha\beta}}{\partial E_\gamma} = -\frac{\partial}{\partial u_{i\alpha}}\left(\frac{\partial^2 E_{tot}}{\partial E_\alpha \partial E_\beta}\right) = -\frac{\partial \chi^\infty_{\alpha\beta}}{\partial u_{i\alpha}} \tag{5.4}$$

where, $Z^*_{i\alpha\beta}$, E_{tot} and $\chi^\infty_{\alpha\beta}$ are Born effective charges, total energy of the system and dielectric susceptibility (electronic contribution), and E_α is the applied electric field along α direction. $u_{i\alpha}$ is displacement of i^{th} atom along α direction, and we use $u_{i\alpha}$ = ± 0.04 Å in finite difference method to evaluate Raman tensor by freezing A_{1g} and E^1_{2g} modes with a magnitude $u_{A_{1g},E^1_{2g}}$ (= ± 0.04 Å), R = $\Delta\chi/\Delta u$.

Table 5.1: Components of Raman tensors of A_{1g} and E^1_{2g} modes, R (A_{1g}) and R (E^1_{2g}).

Pressure (GPa)	R_{11} (A_{1g}) = R_{22} (A_{1g})	R_{33} (A_{1g})	$\sum_{i=1}^{2} R_{ii}$ (E^1_{2g}) = R_{11} (E^1_{2g}) + R_{22} (E^1_{2g})	$\sum_{i,j=1}^{2} R_{ij}$ (E^1_{2g}) = R_{12} (E^1_{2g}) + R_{21} (E^1_{2g})	Ratio $R_{11}(A_{1g})/R_{ij}(E^1_{2g})$
4	18.8	59.9	0.0	4.4	4.27
8	23.5	131.1	0.0	0.4	58.75
12	27.7	514.7	0.0	5.0	5.54

We find that $R_{33}(A_{1g})$ increases with pressure (see Table I), though its value after the gap closing point (∼ 8 GPa) is not quite well-defined (*i.e.* at P= 12 GPa). The R_{ij} (E^1_{2g}) (= R_{12} (E^1_{2g}) + R_{21} (E^1_{2g})) has a large magnitude at P= 4 GPa, and passes through a minimum at P = 8 GPa and then rises again. These elements do not change much above the pressure of the gap closing point (Table 5.1). As a result, the relative intensity ratio of A_{1g} to E^1_{2g} modes will exhibit a maximum at 8 GPa. Thus, the peak in Figure 5.1c arises primarily from non-monotonous change

in Raman tensor of E^1_{2g}mode (Table 5.1).

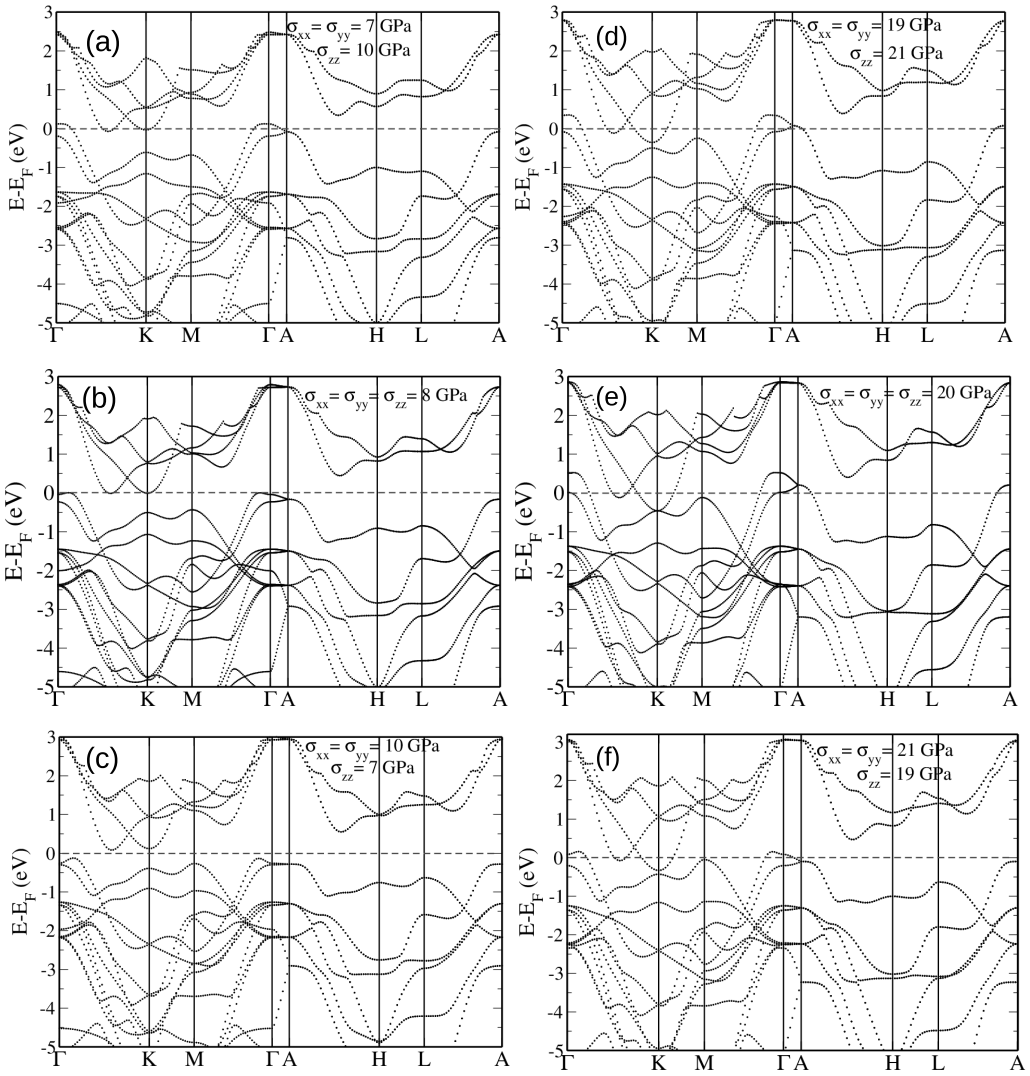

Figure 5.7: Electronic structure of 2H-$MoTe_2$ at non-hydrostatic pressure, (a) σ_{xx} (=σ_{yy}) = 7 GPa and σ_{zz} = 10 GPa, (c) σ_{xx} (=σ_{yy}) = 10 GPa and σ_{zz} = 7 GPa, (d) σ_{xx} (= σ_{yy}) = 19 GPa and σ_{zz} = 21 GPa, and (f) σ_{xx} (= σ_{yy}) = 19 GPa and σ_{zz} = 21 GPa and at hydrostatic pressure (b) σ_{xx} (= σ_{yy} = σ_{zz}) = 8 GPa and (e) σ_{xx} (= σ_{yy} = σ_{zz}) = 20 GPa.

It is known that the KBr pressure medium does not provide hydrostatic conditions above 3-5 GPa in experiments [176]. However, there are technical limitations in using other pressure transmitting media and hence we address this issue theoretically. For this, we compute the electronic structure of 2H-$MoTe_2$ at non-hydrostatic

pressures near the transition pressures 8 GPa and 20 GPa, using first-principles calculations. At P = 8 GPa, 2H-$MoTe_2$ shows semiconductor to semimetal transition whereas Lifshifz transition takes place at P= 20 GPa. We consider two different non-hydrostatic conditions of pressure near 8 GPa (σ_{xx} (=σ_{yy}), σ_{zz}) = (7, 10) and (10, 7) GPa. From our calculations, it is clear that 2H-$MoTe_2$ is semimetal at (7, 10) GPa (see Figure 5.7a) whereas it is semiconductor at (10, 7) GPa (see Figure 5.7c). Comparison of electronic structure of states at (8, 8) GPa and (7, 10) GPa reveals that density of states near Fermi energy is higher in the latter (Figures 5.7a and b). On the other hand, we find an opposite behavior at (10, 7) GPa, the density of states near Fermi energy decreases and a small gap opens up. Thus $\sigma_{zz} > \sigma_{xx} = \sigma_{yy}$ favors the transition at lower pressure, while $\sigma_{zz} < \sigma_{xx} = \sigma_{yy}$ pushes the transition to higher pressures. Thus, we conclude that (a) the character of the transition is preserved even when the pressure is non-hydrostatic, and (b) the transition pressure may change by a few GPa.

We perform similar calculations near second transition (P= 20 GPa) at (19, 21) GPa and (21, 19) GPa (see Figures 5.7d, e and f), and find that small gap opens up at K point (Figures 5.7d and f), but it is well below the Fermi level. Clearly, there is no notable change in the states near Fermi energy. Thus, deviation from hydrostatic pressure should not affect the behavior of this higher pressure electronic transition, as much as it affects the lower pressure transition.

5.1.8 Conclusions

We have analyzed the pressure induced semiconductor to semi-metal transition at $\sim$ 8 GPa and a Lifshitz transition at $\sim$ 20 GPa in 2H-$MoTe_2$ by first-principles density functional theoretical calculations (in complement with Raman experiments by Prof. Sood's group). The signatures of semiconductor to semimetal and the Lifshitz transitions are carried by the frequencies of the first order A_{1g} and E^1_{2g} Raman modes.

The occurrence of a maximum in the integrated ratio of the A_{1g} and E^1_{2g} modes is mainly due to non-monotonous change in Raman tensor of E^1_{2g} mode with pressure. We calculated the effect of pressure on Raman active modes, and find that pressure influences the EPC of A_{1g} most strongly. All the Raman active modes harden with increasing pressure, and electron phonon coupling increases under compression due to changes in the Fermi surface. We hope that our findings will stimulate further study of high pressure and low temperature resistivity experiments to capture the anomalies near the Lifshitz transition.

5.2 Te-deficient 2H-$MoTe_2$: Electronic and Thermoelectric properties

5.2.1 Introduction

Group VI transition metal dichalcogenides (TMDCs) are materials of composition MX_2 where M is a transition metal (Mo, W) and X is a chalcogen atom (Se, S, or Te). They form layered structures where covalent bonding binds atoms strongly within the layers, while van der Waals interaction provides a weak bonding between the layers. They usually have hexagonal or rhombohedral symmetry with the metal atoms coordinated in either octahedral or trigonal prismatic environment. A remarkable contrast in the properties these *polymorphs* of TMDCs create possibilities of various electronic devices [16, 104, 109].

Molybdenum ditelluride $MoTe_2$ a member of this family, is an interesting compound which exhibits electronic structure with signatures of a strong spin-orbit interaction, and has the lowest band-gap ($\sim$ 1 eV) among MX_2 compounds, which makes it useful in the making of tunneling field effect transistors (TFETs) in addition to its other applications [177]. It occurs in three structures: (a) trigonal prismatic

($2H$-$MoTe_2$), (b) monoclinic structure (β-$MoTe_2$), (c) distorted octahedral structure (Td-$MoTe_2$). The 2H or $2H$-$MoTe_2$ has a layered structure of the form Te-Mo-Te which is characterized by a stacking sequence AbABaB, where A, B are Te atom layers and a, b are Mo atom layers with triangular lattices (Figure 5.8a). The Te atoms in the two hexagonal planes are separated by a plane of metal atoms. The number of atoms in a unit cell of this form is 6, with each Mo atom trigonal prismatically coordinated by 6 Te atoms (see Figure 5.8a and d). When a metal atom is displaced from the central position of the 2H hexagonal layered structure, the coordination around the metal atom becomes a slightly distorted octahedron, making the coordination number of Mo atom 8. This leads to the formation of monoclinic β-form of $MoTe_2$ which is stable at temperatures above 900 °C [178] and contains 12 atoms per unit cell (see Figures 5.8b and e). The β-form shows an interesting phase transition on cooling where the layers shift quasi-continuously giving an orthorhombic crystal. With decreasing temperature, the c lattice parameter increases, and then decreases as the layers lock into the new orientation wherein the monoclinic angle of 93° reduces to orthorhombic 90° [178]. The T_d structure of $MoTe_2$ has layered structure where each of the layer consists of Te-Mo-Te atomic planes, stacked along c axis through weak van der Waals interaction where each Mo atom is surrounded by eight neighbours (Figure 5.8) [178]. Among the three forms of $MoTe_2$, $2H$-$MoTe_2$ has been extensively studied since it is the most stable form at room temperature. This form with strong spin orbit coupling and an indirect band-gap of 1 eV, is a semiconductor with diverse applications in logic transistors, charge density waves, superconductors, spintronics and valley optoelectronics [179]. The β phase has potential applications in a novel type of device: topological field-effect transistors based on quantum spin Hall (QSH) insulators [179].

In general, electronic transport properties of a solid are determined mainly by the electronic states near the band gap. These states are easily influenced by possible

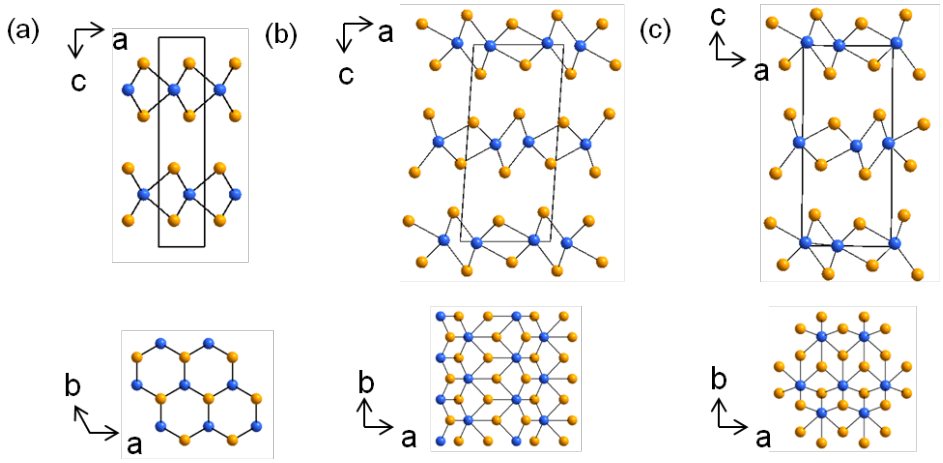

Figure 5.8: Side and top views of crystal structure of (a) 2H-$MoTe_2$, (b) 1T′-$MoTe_2$ and (c) Td-$MoTe_2$.

defects in the system or any pertubation, and hence the defects play an important role in the performance of a material as a semiconductor, metal or insulator. Extensive studies have been conducted on the effects of defects on few of the TMDCs like MoS_2 crystals [180–185]. On the other hand, comparatively few studies have been conducted on the effect of point defects (vacancy of Te atom) in $MoTe_2$ [186, 187] crystals.

In the section 5.2, we have investigated the nature of the defect states in $MoTe_2$ associated with Te vacancies using the first-principles calculations based DFT. We also investigate the structure, electronic structure and transport properties of three different *polymorphs* of $MoTe_2$ in presence of Te-vacancies which are expected to have strong influence on material properties. We explain the origin of p-n crossover observed in measured Seebeck coefficients of 2H-$MoTe_2$ as shown in experiments by Prof. CNR Rao (JNCASR). We compare the calculated transport properties with experimental results and explain the trends observed as a function of temperature in experiments using Boltztrap code with input of first-principle electronic structure.

5.2.2 Computational Details

Our first-principles simulations are within the framework of density functional theory (DFT) as implemented in QUANTUM ESPRESSO (QE) [41] package, which uses a plane wave basis and pseudopotentials. Local density approximation (LDA) of the Perdew-Zunger (PZ) [37] form of the exchange correlation energy functional and norm conserving pseudo-potentials to represent the interaction between ionic cores and valence electrons were used. We include spin-orbit coupling (SOC) [170] through use of relativistic pseudopotentials using a second variational procedure, and van der Waals (vdW) interaction with the implementation of Grimme parameterized scheme [56]. The plane wave basis sets for representation of Kohn-Sham wavefunctions and charge density have been truncated with energy cut-off of 80 Ry and 320 Ry respectively. We aided the convergence to self-consistency using Fermi-Dirac distribution function to smear occupation numbers with a width of 0.003 Ry.

In structural optimization and total energy calculation of pure $MoTe_2$, we have used its conventional unit cell containing 6 atoms for $2H$-$MoTe_2$ and 12 atoms periodic cells of T_d $MoTe_2$ and $1T'$-$MoTe_2$. Integrations over Brillouin zone were sampled on grid of 12 x 12 x 3 k-points for $2H$-$MoTe_2$ and 20 x 10 x 5 k-points for T_d $MoTe_2$ and $1T'$-$MoTe_2$. To model 3% Te vacancies in $2H$-$MoTe_2$, we have constructed a 2 x 2 x 2 supercell (48 atoms) and removed one Te atom from the supercell. To simulate Te vacancies in T_d $MoTe_2$ and $1T'$-$MoTe_2$, we constructed 1 x 2 x 2 supercell with 48 atoms. We also modelled 6% Te vacancies using 1 x 2 x 2, 1 x 1 x 2 and 1 x 1 x 2 supercells of $2H$-$MoTe_2$, $1T'$-$MoTe_2$ and T_d $MoTe_2$ respectively with removal of one Te atom from the supercell.

We have used Boltztrap code [188] for calculating electronic transport (electrical and thermal conductivity) and thermoelectric (Seebeck coefficient) properties. Boltztrap is a program for calculating semi-classical transport coefficients based on smoothed Fourier interpolation of the electronic band.

5.2.3 Pristine $MoTe_2$

From structural optimization of pristine 2H-, 1T′- and Td-$MoTe_2$, our estimates of lattice parameters, a and b are 1-2% smaller than the experimental values [178] (see Table 5.2) and the c/a ratio is slightly underestimated. The little underestimation of the lattice constants (a and b) is typical of the over-binding given by the LDA, and a bit larger over-binding between the layers results (underestimation of c parameter by $\sim 5\%$ for 1T′ structure and $\sim 4.5\%$ for Td structure) after the inclusion of van der Waals (vdW) interactions. Inclusion of nonlocal vdW interactions improve these results (see below). The results obtained with the use of a generalized gradient approximation are comparable to these LDA results of the 2H, 1T′ and Td structures. From the energetics of polymorphic forms of $MoTe_2$, 2H structure is clearly its most stable form. Td-$MoTe_2$ and 1T′-$MoTe_2$ have energies of 298 meV/fu and 133 meV/fu relative to 2H-$MoTe_2$ respectively; 1T′-$MoTe_2$ is more stable than the Td-$MoTe_2$.

Table 5.2: The experimental and calculated lattice parameters of bulk pristine $MoTe_2$ (α, β and T_d).

Polymorph	Experimental Value [178]	Theoretical Value (LDA + local vdW) Å	Theoretical value (LDA + non-local vdW) Å
$2H$	$\vec{a} = \vec{b}$: 3.52	3.47	3.54
	$\vec{c}$: 13.96	13.62	14.08
$1T'$	$\vec{a}$: 6.33	6.31	–
	$\vec{b}$: 3.47	3.46	-0.2%
	$\vec{c}$: 13.86	13.13	-5.2%
Td	$\vec{a}$: 3.47	3.46	–
	$\vec{b}$: 6.33	6.30	–
	$\vec{c}$: 13.83	13.20	–

From the electronic structure and projected density of states of 2H-$MoTe_2$, 1T′-$MoTe_2$ and Td-$MoTe_2$ (Figure 5.9a-c), it is clear that the valence bands (VBs) of all the three structural forms involve strong hybridization between Te $5p$ and Mo

Table 5.3: The calculated electronic bandgap of bulk pristine and anion deficient 2H-$MoTe_2$.

2H-$MoTe_2$	E_g (eV)		
	LDA + vdW (Grimme) [56]	LDA + non-local vdW (vdw-df2-b86r) [190, 191]	LDA + non-local vdW + HSE06 [46]
Bulk	0.576	0.753	1.5
3% Te Vacancy	0.134	0.1907	0.797
6% Te Vacancy	0.099	0.1694	0.771

$4d$ states whereas peaks in the conduction band (CB) are primarily contributed by Mo $4d$ orbitals, with weaker contribution of Te $5p$ and $4d$ states as expected from the ionic charges and bonding in $MoTe_2$. Valence bands deeper in energy comprise largely of p-orbitals of Te. The electronic structure of 2H-$MoTe_2$ exhibits an indirect gap of 0.56 eV between VBM and CBM along Γ-K (Figure 5.9a) direction. Our theoretical band gap is underestimated, as typical of LDA-DFT calculations, in comparison with the experimental value of 1.1 eV [134, 192]. On the other hand, pristine 1T′-$MoTe_2$ and Td-$MoTe_2$ have semi-metallic electronic structure (Figure 5.9b). To improve the bandgap of 2H-$MoTe_2$, we have optimized the structure with non-local vdW interactions using vdw-df2-b86r functional [190, 191]. Our estimated lattice parameters agree with experiments much better than the LDA-vdW estimates (refer Table 5.2). The indirect bandgap of 2H-$MoTe_2$ is improved from 0.56 eV to 0.75 eV. We also used HSE06 functional in our calculations to estimate bandgap more accurately [46], and find an indirect bandgap of 1.5 eV (refer Table 5.3), which is overestimated by 0.4 eV with respect to experimental value.

5.2.4 Effect of Te-vacancies in $MoTe_2$

Since the measured transport properties (by Prof. Rao's group) of $MoTe_2$ cannot be rationalized with the electronic structure of pristine, stoichiometric $MoTe_2$, we

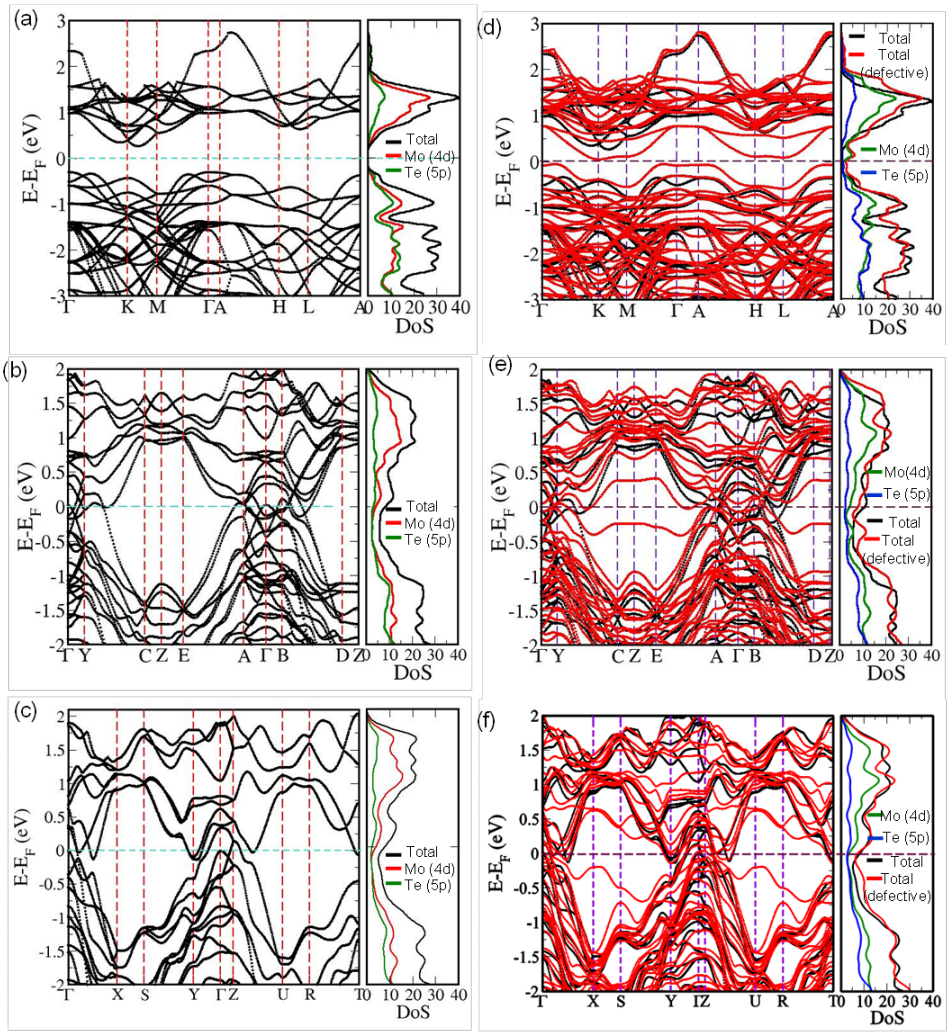

Figure 5.9: Electronic structure and projected density of states (PDoS) of pristine (a) 2H-$MoTe_2$, (b) 1T′-$MoTe_2$ and (c) Td-$MoTe_2$ and with 6% defect (d) 2H-$MoTe_{2-x}$, (e) 1T′-$MoTe_{2-x}$ and (f) Td-$MoTe_{2-x}$. Note that band structure of Te-deficient $MoTe_2$ is superimposed on electronic band structures of bulk $MoTe_2$ shown in (d), (e) and (f).

have simulated 3% and 6% Te vacancies with supercells containing 48 atoms (32 Te atoms and 16 Mo atoms) and 24 atoms (16 Te atoms and 8 Mo atoms) respectively. The defect formation energy is estimated using

$$\delta E = E_v - E_b + E_{Te} \tag{5.5}$$

where E_v, E_b and E_{Te} are the total energies of supercell containing a vacancy, bulk crystal (with the same number of atoms as in the defective structure), and an isolated Te atom respectively. Our estimates of the vacancy energies with 3% concentration of Te-vacancies in 2H-, 1T′- and Td-$MoTe_2$ are 7.18, 6.49 and 6.51 eV/vacancy respectively, while those for 6% concentration of Te vacancies in 2H-, 1T′- and Td-$MoTe_2$ are 7.18, 6.72 and 6.57 eV/vacancy respectively, reflecting relatively weak interactions between the periodic images of vacancies in 2H- and Td- forms. As the difference in energies of pristine $MoTe_2$ in 1T′ and 2H structures is 0.165 eV/cell, these results suggest that Te vacancies play an important role in their relative stability, consistent with Ref. [193]. In the electronic structure of $MoTe_2$ (with these structural forms) with Te-vacancies, bands associated with defect states appear at the top of VB and at the bottom of CB. The indirect gap for 2H-$MoTe_2$ reduces to 0.134 eV and 0.099 eV with 3% and 6% Te-vacancies respectively (Figure 5.9d). The estimate of indirect bandgap with inclusion of non-local vdW interactions are 0.19 eV and 0.16 eV at 3% and 6% concentration of Te-vacancies. As the HSE06 calculations are computationally expensive for large supercell, we used it to determine the gap at Γ-point and applied the corrections in VBM and CBM bands at other k-points to estimate the indirect bandgap values. Resulting indirect gaps with 3% and 6% Te vacancies are 0.797 eV and 0.771 eV respectively. The electronic structure of 1T′-$MoTe_2$ (Figure 5.9e) with Te-vacancies becomes more metallic in nature, with increase in the overlap between valence and conduction bands at the Fermi level (Figure 5.9e). Te vacancy related bands result in reduction of the pseudo gap between the VBs and CBs (along Y-A and B-Z directions for 1T′, and along Γ-Y and Z-T directions for Td structures) *i.e.*, density of states at Fermi level increases. From the density of states of 2H $MoTe_2$, we find a new peak on top of CBM and identify it as the defect peak. This peak is contributed by Mo $4d$ states. For 1T′ and Td $MoTe_2$, we observe a redistribution of density of states, near E_F.

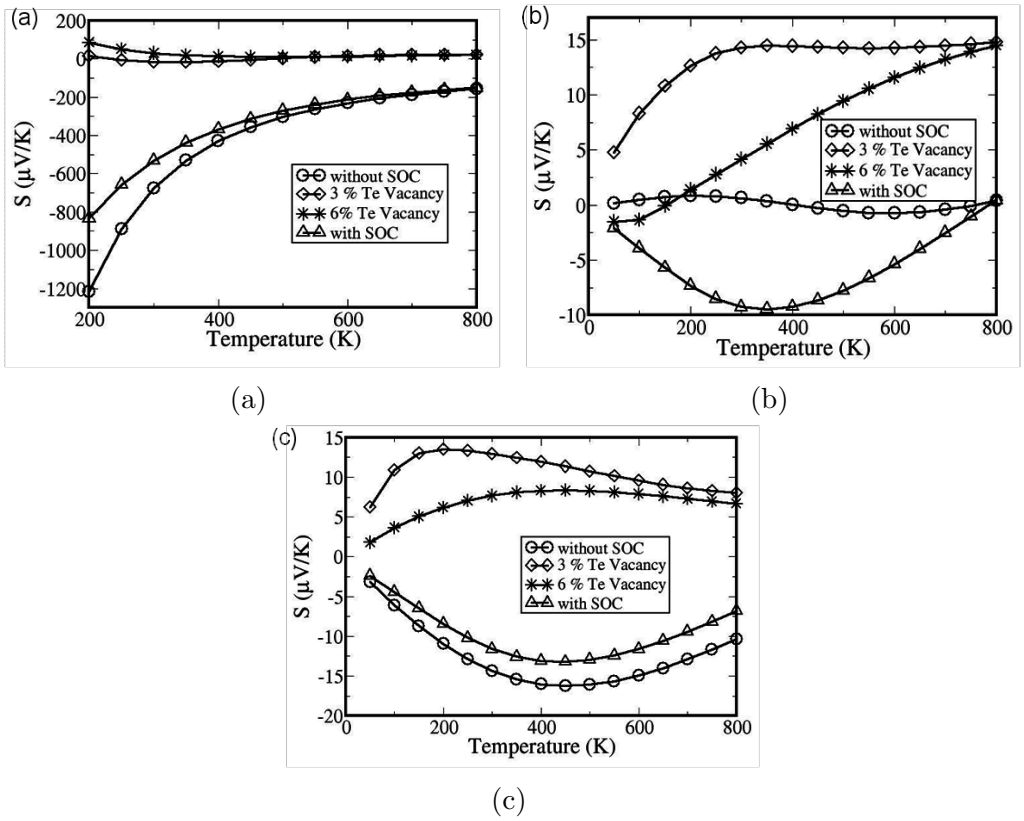

Figure 5.10: Seebeck coefficient as a function of temperature for (a) 2H-$MoTe_2$ with and without spin-orbit coupling and with Te-vacancies, (b) 1T′-$MoTe_2$ with and without spin-orbit coupling and with Te- vacancies and (c) Td-$MoTe_2$ with and without spin-orbit coupling and with Te-vacancies.

We have determined the temperature-dependence of Seebeck coefficient (S), electrical conductivity (σ) and electronic thermal conductivity (κ_{ele}) of pristine 2H-, 1T′- and Td-$MoTe_2$ within semi-classical framework using Boltztrap code with inputs from first-principles electronic structures [188, 194]. For 2H- and Td-$MoTe_2$, the Seebeck coefficient is negative in the entire temperature range studied, indicating n-type conduction in both the forms (Figures 5.10a and c). On the other hand, Seebeck coefficient of 1T′-$MoTe_2$ changes its sign from positive to negative at T= 400 K, indicating a change from p- to n- type conduction with increasing temperature (Figure 5.10b). With inclusion of spin-orbit coupling (SOC), the magnitude of Seebeck coefficient for 2H-$MoTe_2$ (Figure 5.10a) and Td-$MoTe_2$ (Figure

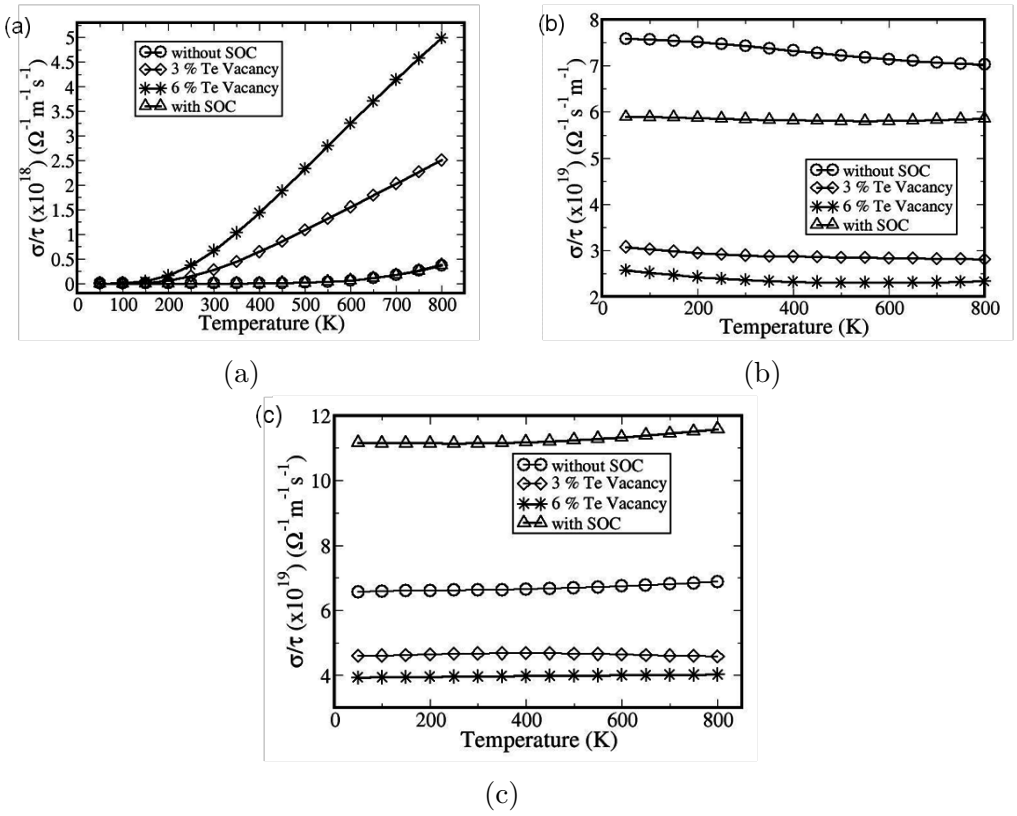

Figure 5.11: Electrical conductivity per unit time as a function temperature: with and without spin-orbit coupling and with Te-vacancies for (a) 2H $MoTe_2$, (b) 1T́$MoTe_2$ and (c) Td-$MoTe_2$.

5.10b) decreases *i.e.* S becomes less negative as the concentration of n-type carriers decreases with changes in the electronic structure near the gap. For 2H-$MoTe_2$, calculated electrical conductivity (σ/τ) and electronic thermal conductivity (κ_{ele}/τ) scaled by the relaxation time are nearly constant up to 400 K beyond which they increase steeply (Figures 5.11a and 5.12a). Inclusion of the SOC does not affect σ/τ and κ_{ele}/τ much. Estimate of σ/τ of Td-$MoTe_2$ is about 6.575 x 10^{19} ($\Omega^{-1}m^{-1}s^{-1}$) at 50 K (Figure 5.11c), which increases gradually with temperature, while κ_{ele}/τ increases monotonically with temperature from 50 K to 800 K (Figure 5.12c). Both σ/τ and κ_{ele}/τ increase in magnitude as a result of changes in electronic structure due to SOC (Figures 5.11b and 5.12b). 1T′-$MoTe_2$ exhibits a markedly contrasting behavior in comparison with the other two forms in that its σ/τ does not change

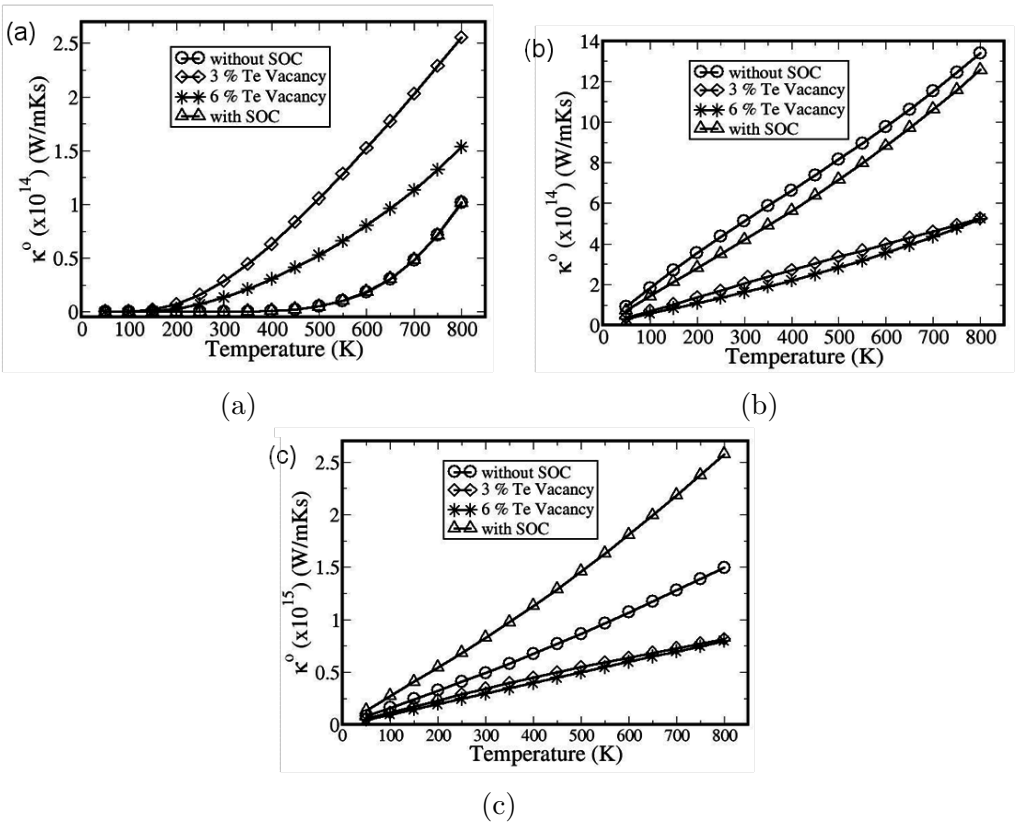

Figure 5.12: Electronic contribution of thermal conductivity as a function temperature: with and without spin- orbit coupling and with Te-vacancies for (a) 2H $MoTe_2$, (b) 1T́$MoTe_2$ and (c) Td-$MoTe_2$.

significantly with temperature (Figure 5.11b), while κ_{ele}/τ increases with temperature with and without inclusion of SOC (Figure 5.12c). SOC has a stronger effect on transport properties of 1T′ $MoTe_2$ than on those of 2H-$MoTe_2$ with its effects on S and σ/τ being stronger than those on κ_{ele}/τ. We note that calculated transport properties (σ/τ, S and κ_{ele}/τ) of pristine $MoTe_2$ do not quite agree with experiments.

We examine the effects of Te-vacancies on the transport properties in 2H-, 1T′- and Td-$MoTe_{2-x}$. The variation in S with temperature for 2H-$MoTe_{2-x}$ (Figure 5.10a) is quite different from that for the pristine 2H-$MoTe_2$ (discussed above). Te-vacancies change the character of the Seebeck coefficient of pristine 2H-$MoTe_2$ from

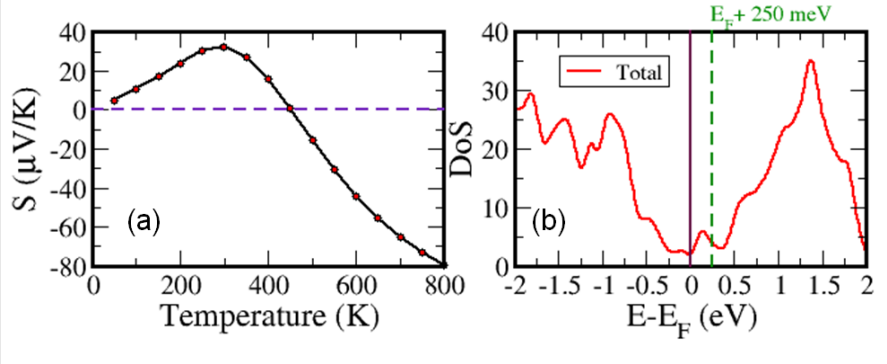

Figure 5.13: Calculated temperature-dependent Seebeck coefficient for 6% Te-deficient 2H-$MoTe_2$ with a 250 meV shift in Fermi level and (b) total density of states of 2H $MoTe_{2-x}$. Note that the green dashed line shows the Fermi level shifted by 250 meV.

n-type to p-type. With a shift in Fermi level by +250 meV of 2H-$MoTe_{2-x}$ with 6% Te-vacancies (carrier concentration corresponding to this Fermi level shift is about 10^{20} cm^{-3}), we find that the calculated temperature dependence of S (Figure 5.13) is in fairly good agreement with experiments reported here. The sign of Seebeck coefficient changes from positive to negative around 450 K indicating a transition from p-type to n-type. The maximum value of S is $\sim$ 32 μV/K, smaller than the experimental maximum value of $\sim$ 125 μV/K, which can be explained partly in terms of higher carrier concentration or doping used in our calculations, and S being inversely proportional to the carrier concentration. We note that such discrepancy in calculations and experiments can arise from the errors in band-structure (particularly associated with d-states near the Fermi energy, compounded with the errors in lattice constants), and possibly other defects in samples.

The calculated transport properties of 1T′-$MoTe_{2-x}$ (Figures 5.10b, 5.11b and 5.12b) agree well with our experimental results. The Seebeck coefficient of 1T′ $MoTe_{2-x}$ with Te-vacancies remains positive and increases with temperature up to 400 K, and attains a constant value of 15 μV/K beyond 400 K (Figure 5.10b). Experimentally too, we observe that Seebeck coefficient of 1T′-$MoTe_{2-x}$ has a positive

sign throughout the temperature range investigated. Consistent with the calculated trend, the observed Seebeck coefficient (in experiments) of 1T′-$MoTe_{2-x}$ increases with temperature and attains a constant value of 32 μV/K beyond 500 K, suggesting a weak bipolar conduction due to thermal excitation of the minority carriers at elevated temperatures. In contrast, σ/τ of 1T′ $MoTe_{2-x}$ (Figure 5.11b) decreases with T up to 400 K and then increases beyond 400 K, which also is consistent with its observed behavior in experiments. Similarly, κ_{ele}/τ of 1T′ $MoTe_{2-x}$ (Figure 5.12b) increases linearly with temperature, in qualitative agreement with experiments.

Calculated Seebeck coefficient of Td-$MoTe_{2-x}$ (Figure 5.10c) remains positive throughout the temperature range investigated in presence of Te-vacancies suggesting that p-type carries are the majority carriers. σ/τ and κ_{ele}/τ (Figures 5.11c and 5.12c) reduce in magnitude due to Te-vacancies. The effective mass of the carriers increases in the presence of defects, (due to flat bands of localized states) and hence the conductivity decreases. σ/τ remains constant with temperature whereas κ_{ele}/τ increases linearly with temperature. There is no experimental data of transport properties of Td-$MoTe_2$ present for comparison with our theoretical results.

5.2.5 Conclusions

We obtained the structural, electronic and transport properties of the three polymorphs of $MoTe_2$ and determined the effect of Te vacancies. We show that pristine 2H-$MoTe_2$ is an indirect gap semiconductor, whereas the 1T′ and Td forms of $MoTe_2$ are semi-metallic. In the presence of Te vacancies, 2H form shows reduction in the indirect semiconducting gap, whereas the other two forms become more metallic. The observed trends in transport properties can be explained with theory only by taking into account Te-vacancies and incipient electron doping. Thus, Te-vacancies in $MoTe_2$ essentially govern the trends in the observed temperature-dependent electronic transport properties of $MoTe_2$.

Chapter 6

Electronic and vibrational signatures of bulk vs. monolayer of Td-WTe_2*

6.1 Introduction

Layered transition metal dichalcogenides are of fundamental and technological importance due to their interesting electronic, optical, chemical, thermal and catalytic properties [16, 104, 196, 197]. In comparison to other Group VI TMDCs, ditellurides are less explored to date and exhibit very different structure and properties. The ditellurides deviate from a simple band model predicting a semiconducting behavior due to trigonal prismatic crystal-field splitting unlike disulfides and diselenides as discussed by Dawson and Bullet [178] based on electronic structure calculations. Tungsten ditelluride (WTe_2) crystallizes in a distorted variant of CdI_2-type structure with an octahedral coordination around the metal, referred to as Td-polytype [192]. The structure of Td-WTe_2 consists of layers of covalently bonded Te-W-Te atomic

*A part of this work has been published in *J. Phys.: Condens. Matter* [195]. Copyright (2015) by Institute of Physic (IOP), URL: *http* : *//iopscience.iop.org*/0953 − 8984/27/28/285401

planes, stacked along c-axis through weak van der Waals interactions. The WTe_6 octahedra are strongly distorted due to off-centering of W atoms as the latter move towards each other to form slightly buckled W-W zigzag chains running along the x-axis. As a result, WTe_2 forms metallic (W-W) bond of length 2.849 Å, which is about 0.13 Å longer than that in the tungsten metal [198]. The reduced Madelung energy as compared to the hypothetical 2H-WTe_2 favors Td form leading to a semimetallic ground state [178, 199].

The exact origin for the preference of the Td-structure instead of the 2H-polytype remains unclear. According to recent reports, single crystals of Td-WTe_2 shows an extremely large unidirectional (along x-axis) positive magnetoresistance [200]. Magnetoresistance in WTe_2 does not saturate even at very high applied magnetic fields, which is considered due to a perfect balanced electron-hole resonance in semimetallic WTe_2, as later complemented with high resolution angle resolved photoemission spectroscopy study of low energy electronic structure [201]. The pronounced anisotropy in magnetoresistance is assigned to the uniaxial character of the Fermi surface and the proximity of balanced electron and hole Fermi pockets aligned along WW chain direction in the k-space.

In this chapter, we study the electronic and vibrational properties of less explored Td-WTe_2 and understand the origin for stabilization of Td-polytype in WTe_2. We explain the non-monotonous transport properties seen in experiments by Prof. CNR Rao (JNCASR). We also identify the symmetry of the peaks observed in Raman spectrum of Td-WTe_2.

6.2 Computational Details

Our first-principles calculations are based on density functional theory (DFT) as implemented in Quantum ESPRESSO package [41], in which the ionic and core-valence electron interactions are modeled with ultrasoft pseudopotentials [40]. The exchange-correlation energy of electrons is treated within a Generalized Gradient Approximation (GGA) with a functional form parameterized by Perdew, Burke and Ernzerhof [36]. We use an energy cutoff of 35 Ry to truncate the plane wave basis used in representing Kohn-Sham wave functions, and energy cutoff of 280 Ry for the basis set to represent charge density. Structures are relaxed to minimize energy till the Hellman-Feynman forces on each atom are less than 0.03 eV/Å. We use a periodic supercell to simulate a 2D sheet, including vacuum of 15 Å to separate the adjacent periodic images of the sheet. In self-consistent Kohn-Sham (KS) calculations of configurations of WTe_2 with monolayered form and bulk *Td*-structure unit cell, the Brillouin zone (BZ) integrations are sampled over uniform meshes of 20x11x1 and 20x11x5 k-points respectively. Electronic structure is determined by including the spin-orbit interaction (SOI) through use of relativistic pseudopotentials using a second variational procedure [170]. To calculate Seebeck coefficient and electrical conductivity, we have used BoltTrap code [188] with input from first-principles. Dynamical matrices and phonons at wavevectors on a 3x3x1 mesh in the BZ were determined using DFT linear response (Quantum ESPRESSO implementation [41] based on Greens function method). From these, dynamical matrices and phonons at arbitrary wave vectors in the BZ are obtained using Fourier interpolation.

6.3 Electronic Structure

Our calculations reveal that bulk and monolayer of WTe_2 exhibit rather similar electronic structure (Figure 6.1), both being semimetallic in nature. This behaviour is

in contrast to other TMDCs, in which a strong dependence of their electronic structure on the number of layers is seen [197]. From the partial density of states (DoS), we see that both the valence and conduction bands near Fermi energy level (E_F) are composed of W-5d and Te-5p states indicating the covalency in W-Te bonding (Figure 6.2). Secondly, the spin-orbit coupling (SOC) included in calculations of electronic structure crucially influences even its qualitative features for example, the spin-split bands. It is clear from the crystal structure, that the dimerized chain of W atoms along X-axis (Figure 6.2d), gives a semimetallic electronic structure along Γ-X direction in the BZ. Along M-Γ path, we find an indirect band gap close to Γ-point (see the zoomed in picture in Figure 6.1). This indirect band gap increases from the bulk to monolayer by 0.1 eV. Above room temperature, thermal excitations of electrons in the partially filled valence and conduction bands are expected to result in the increase in electrical conductivity as seen in experiment at 375 K.

6.4 Vibrational Analysis

6.4.1 Structural Stability

We first note that the bulk *Td* structure of WTe_2 is (a) layered and (b) closely related to centrosymmetric 1T form (c*1T*)(Figure 6.2a) [4]. We assess the structural stability of c*1T* monolayer and *Td* (bulk and monolayer) forms of WTe_2 through determination of their phonon spectra (Figure 6.3). If a phonon spectrum exhibits phonon modes with imaginary frequencies ($\omega^2 < 0$), the structure is locally unstable (*i.e.*, it is not a local minimum, but a saddle point in the energy landscape); otherwise it is stable. The eigen displacements of the unstable modes precisely give the structural distortions that often lower the energy by lowering the symmetry. Our results for phonons of the stable structural forms are relevant and useful in Raman and infra-red (IR) characterization of these structures. Experimentally, bulk WTe_2

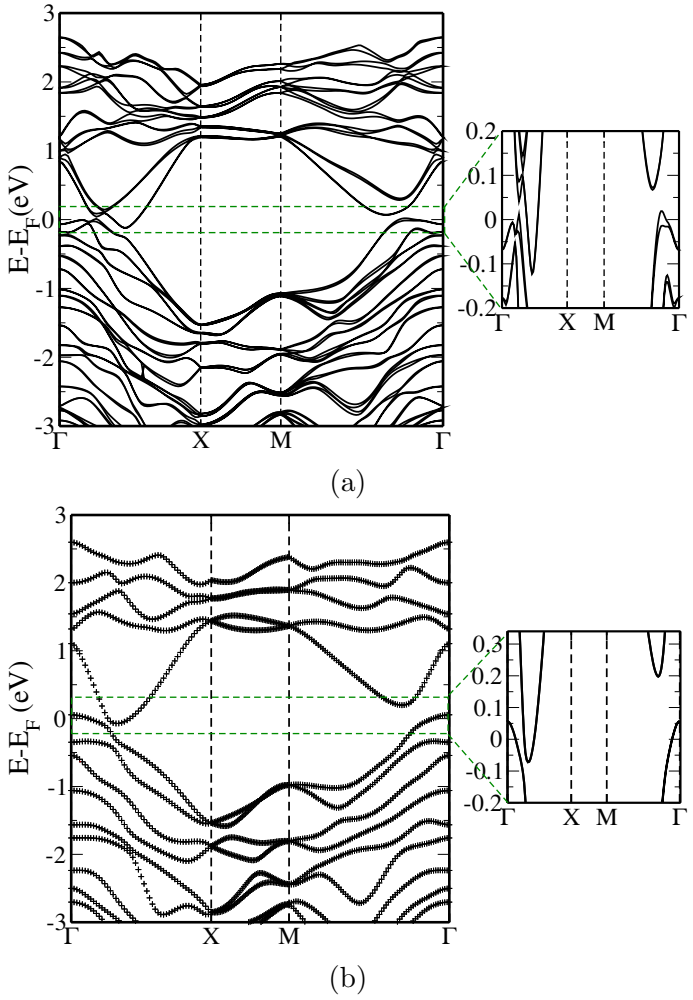

Figure 6.1: Electronic structre of Td-WTe_2 in (a) bulk and (b) monolayer forms. Highlighted part of band structures near the gap in green box is shown on the right. Note that indirect band gap close to Γ-point (along M-Γ path) in monolayer WTe_2 is higher by 0.10 eV than of bulk, which facilitates thermal excitations of carriers and leads to an increase in electrical conductivity above room temperature.

is known to take the Td structure, and our calculated phonon spectrum of bulk WTe_2 exhibits no unstable modes, confirming its stability in the Td structure.

Our analysis of the vibrational spectrum of the c$1T$ polymorph reveals that WTe_2 is structurally unstable, exhibiting structural instabilities with imaginary frequencies of about 100i cm^{-1} (refer to Figure 6.3b) at K and M points. The unstable modes at the high symmetry K-point of the BZ are doubly degenerate, while it is singly

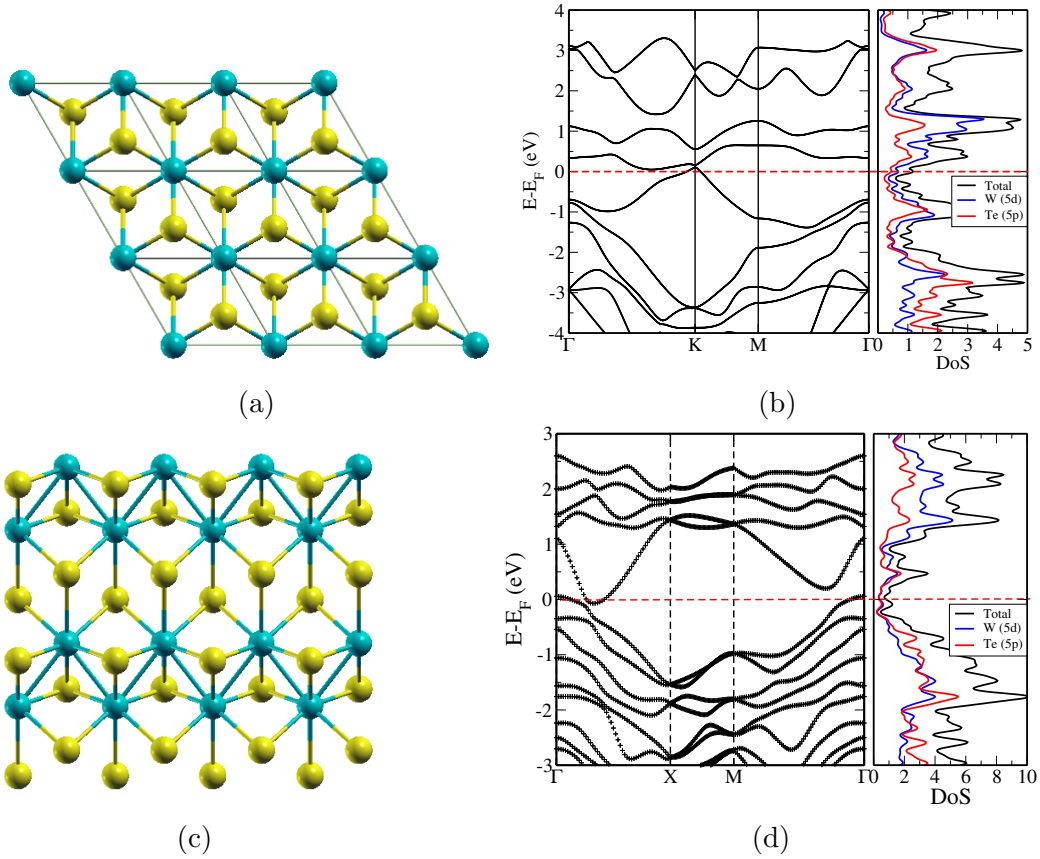

Figure 6.2: Crystal (top view) and electronic structures of monolayered, (a, b) c*1T* and (c, d) T_d forms of WTe_2. c*1T* and T_d structures of WTe_2 are metallic and semimetallic respectively. Note that spin-orbit coupling included in these calculations is crucial even for these qualitative properties of the electronic structure. W and Te atoms are shown with cyan spheres and yellow respectively.

degenerate at the M-point of the BZ. We focus on the M-point instability and its consequences to the structure of the *1T* form [4]. On distorting the c*1T* structure (Figure 6.2a) with eigen-displacements of its unstable mode at M-point, we get a $\sqrt{3}$x1 superstructure (see Figure 6.2c) with zigzag chains of metal atoms. This distorted structure involving dimerization of metal atoms (where the M-M bonds are significantly contracted by 0.8 Å) is semimetallic (see Figure 6.2d). This distorted $\sqrt{3}$x1 superstructure is similar to monolayer of *Td* structure, though the b/a ratio of experimental lattice parameter is 1.80 (as opposed to 1.73 here) due to coupling with strain. It is evident from phonon spectrum that monolayered *Td* structure is

locally stable. Weak instabilities near Γ along the Γ-X and Γ-M directions involve long wavelength rippling of the 2-D planar structure (Figure 6.3c), which is common to other 2-D materials [3, 76].

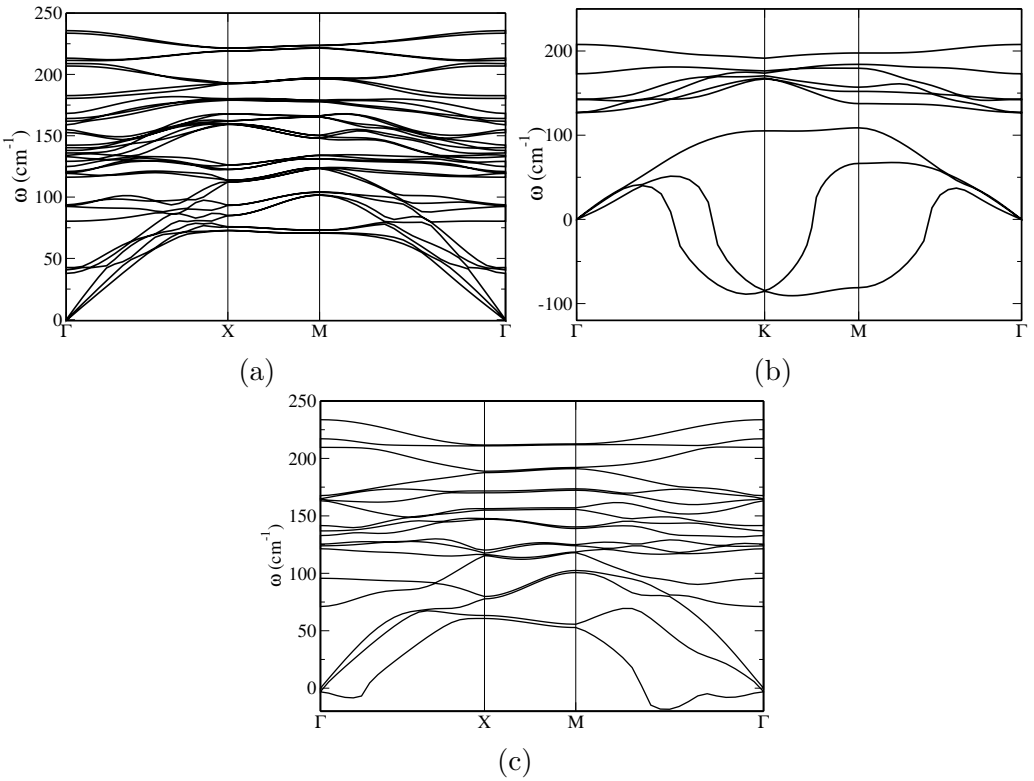

Figure 6.3: Phonon dispersion of WTe_2 in (a) bulk form, monolayer forms with (b) c*1T* and (c) T_d structures of WTe_2. Note that c*1T* WTe_2 exhibits instability at K-point in c*1T* WTe_2 is doubly degenerate and singly degenerate instabilities at K and M points respectively.

6.4.2 Analysis of Raman Spectra

Bulk WTe_2 has a Td crystal structure with a periodic unit cell containing 12 atoms, and belongs to the point group C_{2V} and the space group ($Pmn2_1$). There are 33 optically active modes at the Brillouin zone center (at Γ-point) whose irreducible representations are:

$$\Gamma_{bulk} \rightarrow 11A_1 + 6A_2 + 5B_1 + 11B_2, \tag{6.1}$$

all of which are Raman active because of the low structural symmetry crystal. To assign the irreducible representations to the calculated phonons at Γ, we obtained overlap (inner product) of a basis vector of an irreducible representation and eigen vectors of phonon modes (obtained using density functional perturbation theory). Experimentally, 5 peaks have been observed in the Raman spectrum of bulk WTe_2 [195]. There are many modes with frequencies (tabulated in Table 6.1) close to experimental peaks, which make the assignment of the experimentally observed peaks nontrivial. For example, modes with frequencies 162 cm^{-1}, 164 cm^{-1} and 168 cm^{-1} make the assignment of the experimentally observed intense peak at 165 cm^{-1} subtle, *i.e.* it can be A_2, B_1 or A_1 mode. Similarly, the modes with frequencies 211 cm^{-1} and 213 cm^{-1} are close to the experimentally observed intense peak at 212 cm^{-1} which therefore can be assigned either B_2 or A_1 irreducible representation.

Table 6.1: Calculated phonon frequencies of Raman active modes of T_d-WTe_2.

A_1	A_2	B_1	B_2
Frequency cm^{-1}	Frequency cm^{-1}	Frequency cm^{-1}	Frequency cm^{-1}
42	38	92	41
80	93	119	94
120	116	129	121
134	125	153	133
138	155	164	136
140	162		142
168			159
183			180
207			209
211			213
233			236

The Raman tensor of these possible modes can facilitate the differentiation between these modes. The Raman tensor is calculated as slope of the linear changes in electronic dielectric constant (the second derivative of the electronic density matrix

with respect to a uniform electric field [117]) with normal mode displacements. As bulk WTe_2 is semimetallic in nature (see Figure 6.1), its response to macroscopic electrical field is not finite or well defined, and it is not straightforward to determine the Raman tensor directly. To this end, we estimated the Raman tensor by constraining the occupation numbers of electrons so as to treat Td-WTe_2 as an insulator (*i.e.* number of occupied bands = number of electrons/2). We then identified the modes at $\sim$ 168 cm^{-1} and $\sim$ 207 cm^{-1} as the ones with largest Raman tensor, both belonging to the A_1 symmetry. We label them as $A_1^{'}$ ($\sim$ 168 cm^{-1}) and $A_1^{''}$ ($\sim$ 207 cm^{-1}). Our observed intense Raman peaks are at 211 cm^{-1} and 165 cm^{-1}, in agreement with these theoretical results. Experimental results show that the peak at 211 cm^{-1} is sensitive to thickness (number of layers) whereas the one at 168 cm^{-1} does not depend much on the thickness, though both belong to same symmetry (A_1). To understand such dependence on thickness, we examine the displacements of W and Te in the eigenvectors of these modes (see Figure 6.4). It is evident that (i) the mode $A_1^{'}$ involves out-of-plane (z-direction), displacements of Te atoms and in-plane displacements of W atoms, and (ii) the mode $A_1^{''}$ involves out-of-plane dispalcements of W and in-plane displacements of Te atoms (refer Figure 6.4). Such mixing of in-plane and out-of-plane components of atomic dispalcements is a consequence of low-symmetry of the structure, and has been reported for a similarly strongly distorted structure of 1T-ReS_2 [202].

Secondly, Te atoms of same plane vibrate in phase (Figure 6.4a) in the $A_1^{'}$ mode of vibration, while their motion is out of phase in the $A_1^{''}$ mode (Figure 6.4b). Thus, $A_1^{'}$ mode seems more localized to a layer of WTe_2, and exhibits weaker or no dependence on the thickness or the number of layers. To confirm the observed changes in Raman modes as a function of thickness, we compare the vibrational spectrum of monolayer WTe_2 with that of the bulk. We find hardening of $A_1^{''}$ mode by $\sim$ 3 cm^{-1} and softening of $A_1^{'}$ by $\sim$ 3 cm^{-1} in the monolayer with respect to the

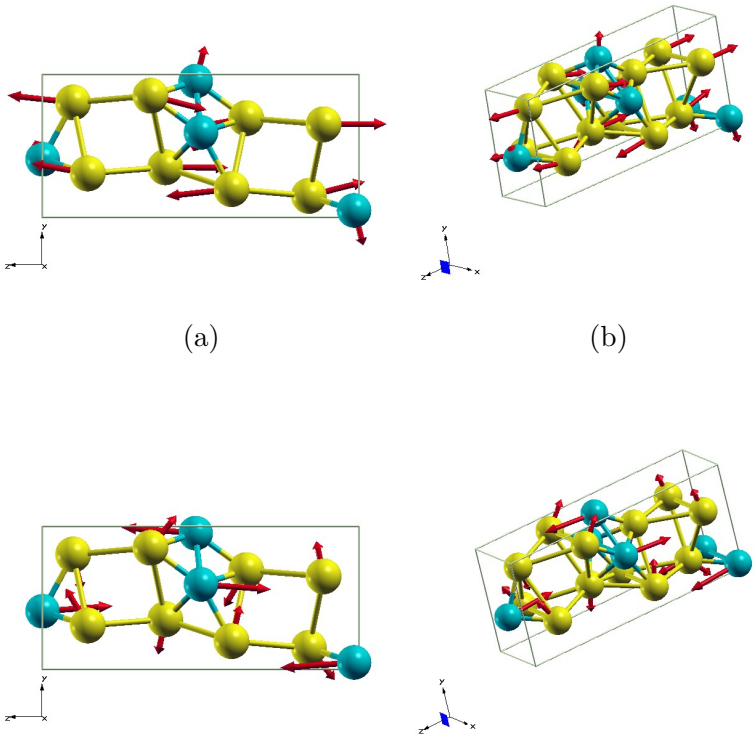

(a) (b)

(c) (d)

Figure 6.4: Raman active phonon modes of bulk *Td*-WTe_2 with largest Raman tensor. (a, b) Two views of the atomic displacement of the $A_1^{'}$ mode with frequency ~ 168 cm^{-1}. (c, d) Two views of the atomic displacement of $A_1^{''}$ mode with frequency ~ 207 cm^{-1}. W and Te atoms are shown with cyan spheres and yellow respectively.

modes of the bulk. While this is consistent with the observed trend in $A_1^{''}$ mode, it suggests additional compensating mechanism that governs the thickness dependence of $A_1^{'}$ vibrational mode, and needs further investigation.

6.5 Transport Properties

We have employed Boltztrap program [188] with input from first-principles calculations to understand the non-monotonous temperature (T) dependence of Seebeck coefficient (S), electrical conductivity (σ) and thermal conductivity (κ) (refer Figure

6.5). This program is based on the smoothened Fourier interpolation of the electronic band structure and used for calculating transport coefficients within semi-classical treatment. Assuming that the band structure does not change with T, we estimated E_F as a function of T. Within this rigid band picture, we could capture the behavior of σ(T) at high T and the nature of S(T) (n-type) at low T. We find that σ increases with T as seen in experiments at higher temperature ($>$ 375 K) (Figure 6.5a), and S becomes more negative as E_F shifts to higher energies into the conduction band (Figure 6.5b). We note that the electronic structure of WTe_2 reveals both electron and holes as carriers and the resulting Seebeck coefficient involves cancellation between their contributions and hence is subtle. We believe that the polycrystalline WTe_2 involves defects and incipient doping along with structural changes that are relevant to the n-p crossover in the Seebeck coefficient as a function of T. Explanation of the observed n- to p-type transition as a function of T seen in experiments probably requires determination of electronic structure as a function of T-dependent structure. Interestingly, the electronic contribution to κ(T) is in qualitative agreement with experiment [195] (refer Figure 6.5c), which increases with increasing T.

6.6 Conclusions

We present electronic structure and vibrational properties of WTe_2 in the monolayered and bulk Td forms, determined using first-principles calculations. We highlight the importance of spin-orbit coupling in accurate description of its electronic structure particularly near the Fermi-level. Due to the lower structural symmetry, all the optical phonons of WTe_2 are Raman-active. We have effectively used symmetry analysis and estimation of Raman tensor in identification of the strongly Raman-active modes, and assigned the symmetry labels to the observed peaks. Finally, we

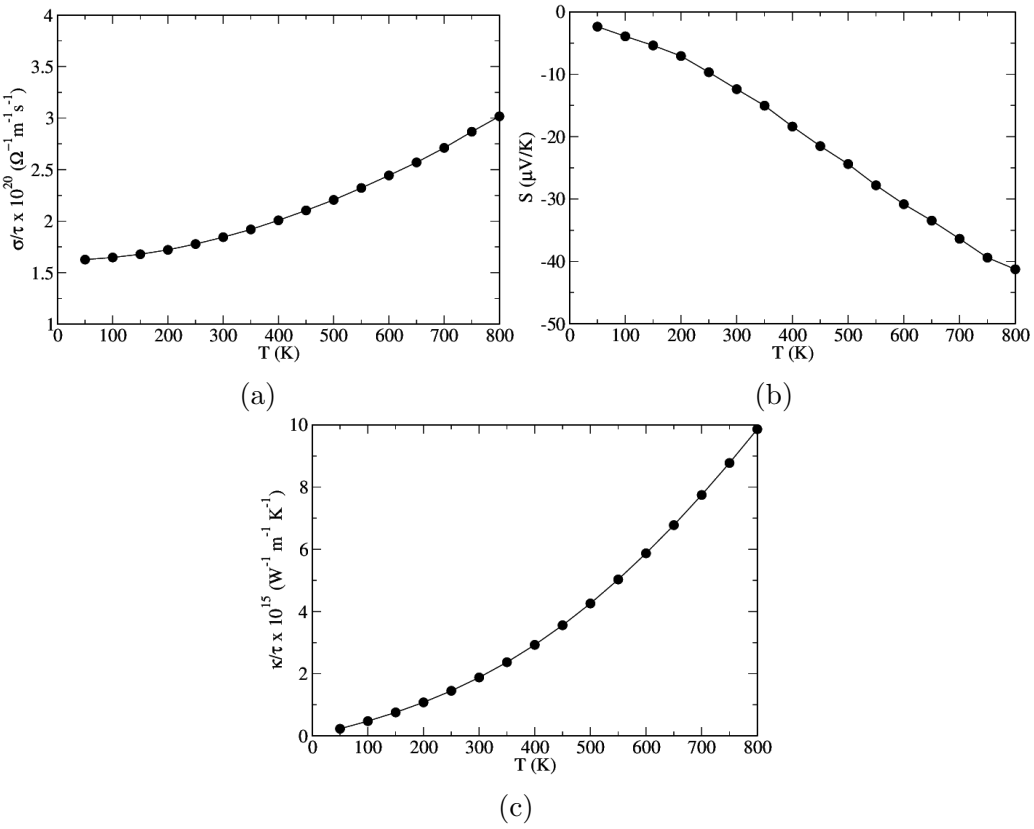

Figure 6.5: T-dependent transport properties of bulk Td-WTe2. (a) Electronic conductivity (σ/τ) (b) Seebeck coefficient (S) (c) electrical contribution (κ/τ) to thermal conductivity calculated using Boltztrap program.

bring out the connection of the Td structure with $1T$ form of layered metal dichalcogenides, and understand its stability in terms of electronic and vibrational properties of the $1T$ form. Transport properties calculation shows qualitative agreement with experimental results of thermal and electrical conductivies as a function of T. The n-p crossover in the Seebeck cofficient as a function of T could be due to defects and incipient doping along with structural changes. Furthur determination of electronic structure as a function of T-dependent structure is required to understand the observed n- to p-type transition as a function of T seen in experiments.

Part III

Black Phosphorus

Chapter 7

Black phosphorus under external fields

7.1 Phosphorene: Electron-hole asymmetry in electron-phonon coupling*

7.1.1 Introduction

Monolayer of black phosphorous (BP) is referred to as phosphorene. Phosphorene lattice structure is a 2-D puckered network (Figure 7.1a) where each atom is covalently bonded with three neighboring atoms (Figure 7.1b). Its in-plane anisotropy is unique feature of phosphorene. The puckered crystal structure of BP leads to asymmetric electronic and phonon dispersion relations such that electronic bands are more dispersive along the armchair direction than along the zigzag direction, whereas the phonon dispersion is more dispersive along the zigzag direction [23,203,204]. Carrier mobility is higher along the armchair direction as the effective mass along the zigzag direction is about 10 times larger than that of armchair direction [205, 206]. Also,

*This work has been published in part in *2D Materials*, 2015 [6]. Reproduce with permission of Institute of Physics (IOP), URL: *http* : //*iopscience.iop.org*/2053 − 1583/3/1/015008.

the Hall mobility along the armchair direction is 1.8 times the mobility along the zigzag direction [207].

Monolayer and few layers BP absorb light ranging from infrared to a part of visible spectrum polarized along arm chair axis, whereas they are transparent for polarization along the zigzag direction [23]. Recent reports of photoluminescence measurements of phosphorene reveal the existence of anisotropic excitons emitting light polarized along direction with a higher exciton binding energy of 0.7-0.8 eV and quasi particle gap of 2.2 eV [208–211].

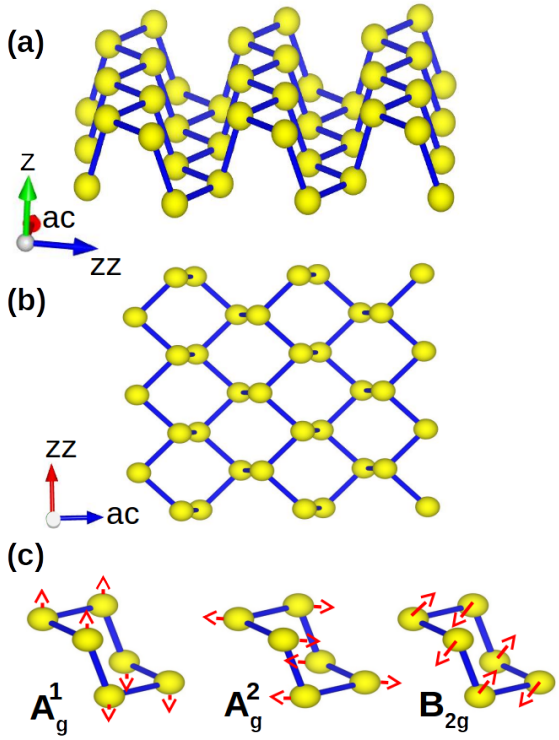

Figure 7.1: (a) Crystal structure of monolayer BP showing the armchair (ac) and zigzag (zz) directions. (b) Top view of monolayer BP. (c) Atomic vibrations of Raman active modes A_g^1, A_g^2 and B_2g.

Electron-phonon coupling (EPC) plays an important role in the resistivity behavior at high carrier concentration for 2D systems like graphene [212]. Raman spectroscopy is a powerful tool for estimation of the number of layers in 2D materials such as graphene and TMDCs [213–216], to characterize EPC of graphene and

evaluating thermal conductivity of graphene [217, 218] among various other properties. For BP also, Raman spectroscopy has shown its potential as successful and noninvasive technique to determine the crystal orientation [207, 208, 219, 220]. The degradation of BP flakes due to environmental aspects have been proved by Raman spectroscopy [221].

The unit cell of phosphorene contains 4 atoms. Out of the nine optical modes, phosphorene has six Raman active modes, out of which three prominent modes have irreducible representation A_g^1, A_g^2 and B_{2g}, as observed in back scattering geometry [6]. The eigen-vectors of these modes show that A_g^1 mode involve out-of-plane displacement of atoms, and A_g^2 and B_{2g} modes are along armchair and zigzag directions respectively (Figure 7.1).

In the section 7.1, we identify the effect of doping on the Raman active phonons in phosphorene, revealing characteristic EPC. While A_g modes are affected by doping, B_{2g} mode remain insensitive (Figure 7.3a-c) [6]. Further A_g modes soften and their linewidths broadens with electron doping while remains unaffected by holes as observed in experiments (Figure 7.3) [6]. Using first-principle calculations, we understand the contrasting effect of electron and hole doping on Raman active modes of phosphorene (in complement to Raman measurements by Prof. Sood's group).

7.1.2 Computational Details

Our first-principles calculations are based on density functional theory as implemented in Quantum ESPRESSO package, [41] and norm-conserving pseudopotentials [168, 169] to model the interactions between valence electrons and ionic cores. The exchange-correlation energy of electrons is treated within a Local Density Approximation (LDA) functional as parametrized by Perdew and Zunger [37]. We use an energy cutoff of 60 Ry to truncate the plane wave basis used in representing Kohn-Sham wave functions, and an energy cutoff of 240 Ry to represent charge

density. Structures are relaxed till the Hellman-Feynman force on each atom is less than 0.03 eV/Å. We have used a periodic supercell to simulate a phosphorene sheet, with a vacuum of 15 Å (along y-direction) to separate its adjacent periodic images. Integrations over the Brillouin Zone (BZ) are sampled on a 12x1x9 and 48x1x36 uniform meshes of k-points in the calculation of total energy and electron-phonon coupling respectively. For a few hole doping concentrations (1.3 x 10^{13} cm^{-2} and 1.8 x 10^{13} cm^{-2}), we have used 72x1x54 uniform mesh of k-points in determination of electron-phonon coupling.

7.1.3 Electronic structure

Electronic structure of phosphorene determined from our first-principles calculations exhibits a direct band gap of 0.89 eV (see Figure 7.2a) at the Γ point, which is in good agreement with the earlier theoretical results [22]. We note that electronic structure is remarkably different along zigzag (Γ-Z) and armchair (Γ-X) directions. It shows linear dispersion along the armchair and parabolic dispersion along the zigzag directions. States at conduction band minimum (CBM) and valance band maximum (VBM) are constituted of p_y orbitals of phosphorous (Figure 7.2b) at Γ point. We observe that symmetry of the wavefunctions at CBM and VBM is distinct (see Figure 7.2), which leads to a contrast in the effects of electron and hole doping on electron-phonon coupling (to be explained in detail later).

7.1.4 Effect of charge doping on vibrational spectra

We have simulated carrier (electron and hole) doping in phosphorene by adding small fraction of electron/hole (according to doping concentration) to the unit cell. This affects mostly A_g^1 and A_g^2 modes (see Figure 7.3g-i): A_g^1 and A_g^2 modes soften significantly ($A_g^1 \sim 3$ cm^{-1} and $A_g^2 \sim 2$ cm^{-1} at $\sim 1.8 \times 10^{13}$ cm^{-2}) with electron

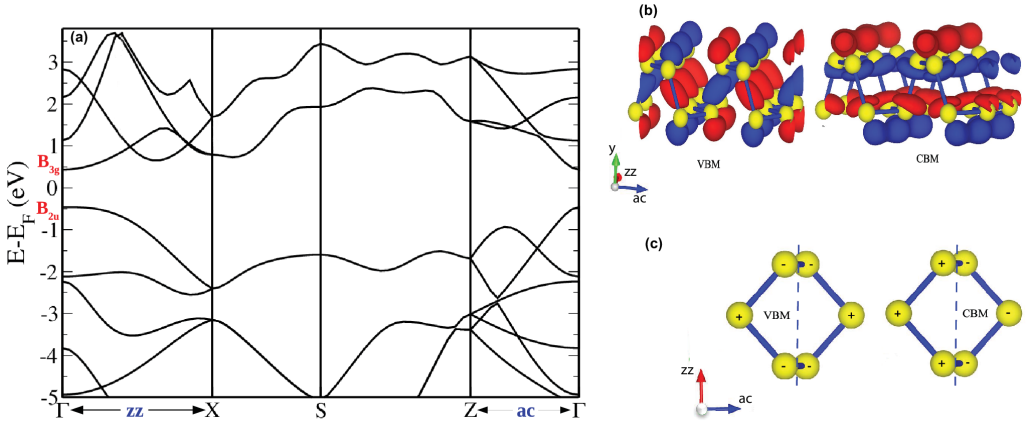

Figure 7.2: (a) Electronic structure of phosphorene with symmetry labels B_{2u} at VBM (valance band maximum) and B_{3g} at CBM (conduction band minimum) at Γ-point (b) isosurfaces of wavefunctions at VBM and CBM at the Γ-point, and (c) a schematic diagram showing symmetry of the wavefuction at VBM and CBM at Γ-point where dashed lines are showing mirror planes. Note that wavefuction at VBM and CBM are even and odd respectively, under mirror reflection.

doping as compared to hole doping. In contrast, B_{2g} mode remains unaffected by carrier (both electron and hole) doping, which is in good agreement with the experimental results (see Figure 7.3a-c). To understand this observed trend (see Figure 7.3a-c) and the associated interactions between electrons and phonons, we have performed systematic study of electron-phonon coupling with carrier doping. The electron-phonon coupling (EPC) of a phonon mode ν at wavevector q is given as

$$\lambda_{q\nu} = \frac{\gamma_{q\nu}}{\pi\hbar N(\epsilon_F)\omega_{q\nu}^2}, \tag{7.1}$$

$$\gamma_{q\nu} = 2\pi\omega_{q\nu}\sum_k\sum_{ij}\left|g_{k+q,k}^{q\nu,ij}\right|^2\delta(\epsilon_{k+q,i}-\epsilon_F)\delta(\epsilon_{k,j}-\epsilon_F), \tag{7.2}$$

where $N(\epsilon_F)$ is density of states at the Fermi energy and ω is the frequency of phonon $q\nu$. The electron-phonon coupling matrix element is defined as

$$g_{k+q,k}^{\nu,ij} = \left(\frac{\hbar}{2M\omega_{q\nu}}\right)^{\frac{1}{2}}\langle\psi_{k+q,i}|\frac{\partial V}{\partial U^\nu(q)}|\psi_{k,j}\rangle, \tag{7.3}$$

where $\psi_{k,j}$ is electronic wavefunction at wavevector k for j band, M is an effective mass, and $\frac{\partial V}{\partial U^{\nu}(q)}$ is the change in the self consistent potential associated with atomic displacements of phonon qν. Our calculations show that (a) A_g^1 and A_g^2 modes couple

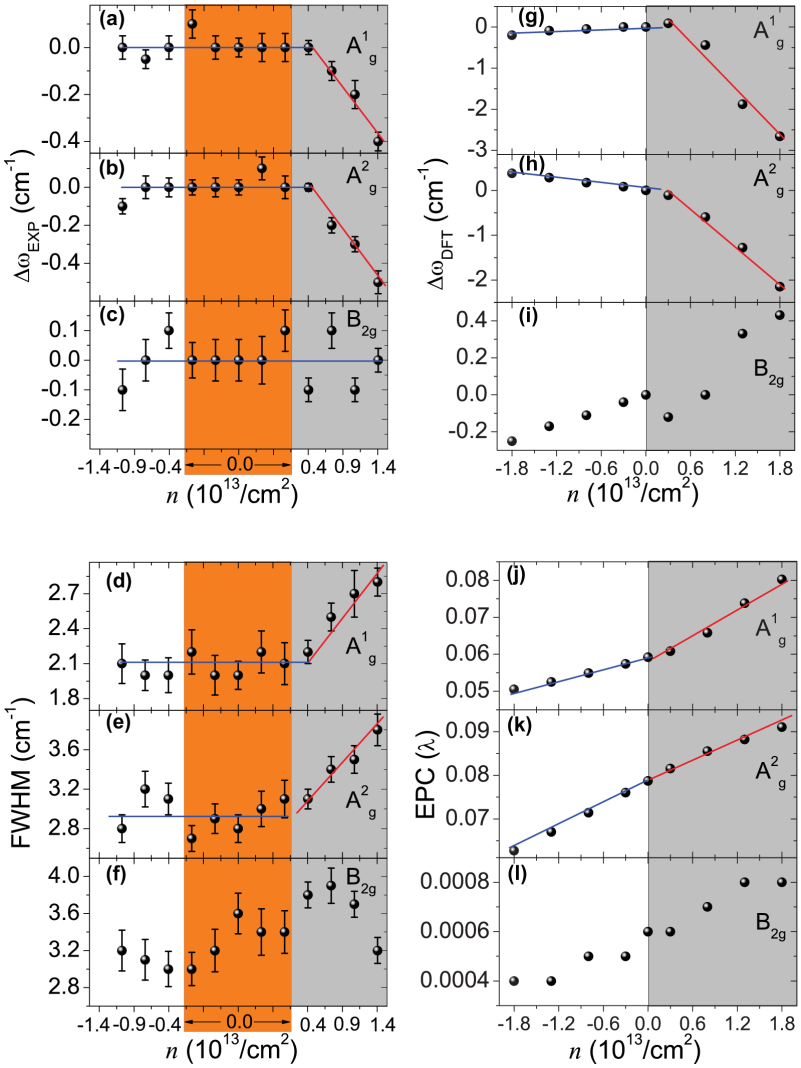

Figure 7.3: (a)-(c) Changes in phonon frequencies $\Delta\omega$, and (d)-(f) FWHM of Raman peaks, as obtained from experiments, as a function of carrier concentration n. (g)-(i) $\Delta\omega$ obtained from DFT calculations and (j)-(i) calculated values of EPC (λ) as a function of n. The lines are guide to eye. The off-state and electron doped regions are marked with orange and grey shades.

much more strongly with electrons than B_{2g} mode, and (b) these modes show couple more strongly with electrons than holes (consistent with experiments, Figure 7.3d-f). Strong coupling of A_g^1 mode with electrons can be understood with analysis of

the governing symmetry. The A_g modes (see Figure 7.1c) have the symmetry of the lattice, *i.e.* distortion along these modes does not break the symmetry of the lattice. As a result, all the electronic states have a non-zero matrix element (from Eq.7.3) for the perturbation of A_g modes, for $\nu = q = 0$. With the same argument, matrix element (Eq. 7.3) vanishes for B_{2g} mode which breaks the symmetry of the lattice (B_{2g} mode is orthogonal to A_g modes).

We do observe an asymmetry in EPC with hole and electron doping: EPC increases with increasing concentration of electron doping while it decreases with increasing concentration of hole doping. This asymmetry can be explained in terms of the symmetry of the wavefunctions at VBM and CBM at Γ point. At the VBM, wavefunction is even under mirror reflection, while that wavefunction at the CBM is odd under mirror reflection. Thus magnitude as well as the sign of the coupling matrix (Eq. 7.3) is different for electron and hole doping. It is evident in Figure 7.3 that A_g^1 mode is affected more strongly by electron doping than the hole doping. In contrast, A_g^2 mode is affected by both electron as well as by hole doping. To understand these effects of electron and hole doping on A_g^1 and A_g^2 modes quantitatively, we obtained the energies of VBM and CBM as a function of structural distortions frozen corresponding to eigenvectors of these modes.

We clearly see that the CBM varies more strongly as compared to the VBM with A_g^1 mode (Figure 7.4). On the other hand, freezing of A_g^2 mode affects both VBM and CBM quite significantly though the effect on CBM is slightly more in comparison to that on VBM. Thus the contrast in the dependence of A_g^1 and A_g^2 modes on electron and hole doping originates from the matrix element $\langle\psi_{k,i}|\Delta V_\nu|\psi_{k,j}\rangle$. Interestingly, we find inversion of CBM and CBM+1 bands for phosphorene (see Figure 7.5) with structural distortion of A_g^1 mode, which is relevant to studies of excited state properties.

The symmetry of the monolayer of black phosphorous (phosphorene) is D_2h and

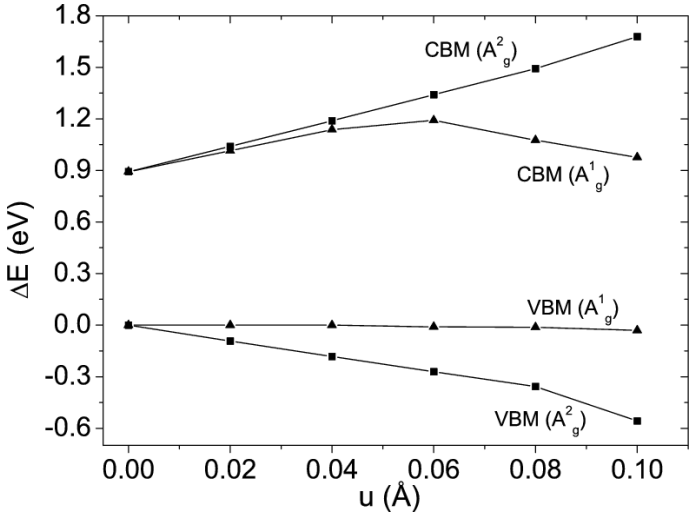

Figure 7.4: (a) Change in the energies of CBM, CBM+1 and VBM (relative to VBM at zero freezing), as a function of structural distortion obtained with A^1_g mode (a) and energies of CBM and VBM as a function structural distortion obtained with A^2_g mode (b).

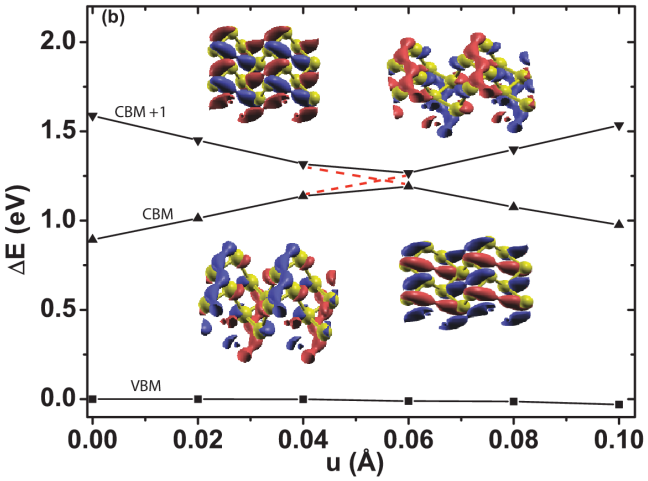

Figure 7.5: Isosurfaces of wavefunctions of CBM and CBM+1 with structural distortion of A^1_g mode for 0.04 Å and 0.06 Å, that reveal the band inversion between CBM and CBM+1 bands. If both the p_y orbitals are seen in the same reference frame across the red dashed line, we observe that p_y orbitals get flipped by 180° *i.e.* $\psi = -\psi$ confirms band inversion of CBM and CBM+1.

does not alter with increasing number of layers. The symmetry arguments given to explain the nature of A_g and B_2g modes with carrier doping hold good for few layers

of black phosphorous.

We note that low levels of doping result in changes in the population of only the states that have energies close to the VBM and CBM at the Γ point. Thus, the states lining the band-gap along Γ-X direction (Figure 7.2) are more relevant to our experiments than the ones along Γ-Z (energies of the states at Z-point are too far (Figure 7.2a) from the gap to be affected by low levels of doping in phosphorene transistor). In Figure 7.6, we now include isosurfaces of wavefunctions of the valence and conduction bands at X-point and a diagram of their projections on p-orbitals of P. We note that the bands at X point are doubly degenerate, and are made from p_x and p_y orbitals of P, in contrast to the VBM and CBM at Γ point consist of p_y orbitals. From the Figure 7.6, it is clear that the relative phases of p orbitals of the P sublattices are the same for wave functions at X and Γ (Figure 7.2c) points. Hence, our symmetry analysis of the coupling of Raman active phonons to the states along Γ to X is similar. Since the orbitals involved in the VBM and CBM bands at X point are different from those at Γ point, their relative phase factors are not simple. In fact, they involve rotations in the 3-dimensional space of bands made of two p-orbitals. Thus, their relative phases can be meaningfully described with a Hermitian matrix that is responsible for the complex Raman tensor relevant to the polarization dependent Raman scattering observed in Ref. [219]. To connect more closely with the results of Ref. [219], we determined optical dielectric constants of structures obtained by freezing A_g^1 and A_g^2 modes. $\Delta\epsilon_{xx}$ and $\Delta\epsilon_{zz}$ are 0.05 and 1.3 for A_g^1 and 0.2 and 1.5 for A_g^2 modes respectively which show (i) a remarkable anisotropy in the Raman tensor, and (ii) are quite distinct for A_g^1 and A_g^2 modes, in qualitative agreement with empirical parameters obtained from polarization dependent Raman spectra of Phosphorene [219].

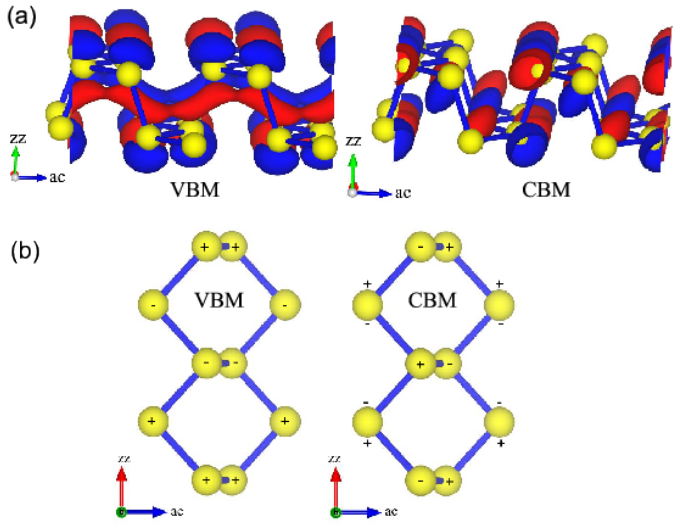

Figure 7.6: (a) Isosurfaces of wavefunctions of VBM and CBM at the X-point and (b) a schematic diagram of projection on $p_{x,y}$ orbitals of P showing symmetry of the wavefunction at VBM and CBM at X-point. Note that the states at the VBM and CBM at X-point are doubly degenerate and isosurfaces of the degenerate states (VBM and VBM+1 or CBM and CBM+1) are similar.

7.1.5 Conclusions

The Raman active modes with A_g symmetry soften significantly with electron doping than with the hole doping, while the mode B_{2g} is insensitive to any doping due to the symmetry of relevant electronic states. The contrasting effect of electron and hole doping on EPC is also explained with symmetry arguments, and quantitatively with first-principles calculations. For reproducing experimental results for the intensity of A_g modes, the Raman tensor has to be complex whereas for B_{2g}, real values of Raman tensor elements can explain angular dependence [219]. The complex values of Raman tensor can arise from electron radiation as well as electron-phonon matrix elements [219]. We show that the imaginary part of Raman tensor elements is different for the two totally symmetric modes A_g^1 and A_g^2, pointing out that electron-phonon interaction is a key factor responsible for the complex values of the tensor.

7.2 Pressure dependent study of black phosphorus

7.2.1 Introduction

Black phosphorus (BP) is the most stable form among the exhisting allotropic structures of phosphorus at ambient conditions. The structure of BP is orthorhombic and consists of puckered layers which bind together with weak van der Waals interactions [222]. From electrical conductivity measurements, it is inferred that BP is a direct band gap semiconductor with a gap of 0.35 eV [223, 224]. Recently, BP was introduced as layered thin film materials [27, 225], with bandgap depending on layer thickness: it is 0.3 eV for thickness $>$ 4nm and 1.2 eV for a monolayered BP. This variation in bandgap of BP as a function of thickness bridges the gap between gapless graphene and relatively wide gap of transition metal dichalcogenides and makes it suitable for infrared optoelectronic devices [26]. An interesting sequence of structural transformations from the orthorhombic (semiconductor) phase to rhombohedral (semimetal) phase and then to simple cubic (metal) phase with pressure [226, 227] is observed in BP. The simple cubic phase exhibits superconductivity at 4.7 K [228, 229]. The superconducting temperature is slightly pressure dependent and increases with increasing pressure and the superconducting state remains stable for several hours even if pressure is removed. BP shows superconductivity with high transition temperature (10K) if it is cooled to 4K first and then pressure is applied, showing that pressure can be effective in tunning its characteristics significantly.

Pressure or strain have been used to change the relative strength of spin-orbit coupling inducing electronic topological transition (ETT) in materials like Sb_2Se_3

[161], b-As_2Te_3 [230], BiTeI [231]. Recently, Gong et al. [232] reported a pressure induced Lifshitz transition at P= 1.23 GPa, where black phosphorus undergoes a semiconductor to three-dimensional Dirac semimetal transition. By using first-principles density functional theoretical calculations within GGA and mBJ exchange-correlation functionals, Gong et al. [232] showed that band inversion occurs at Z point at 1.23 GPa and robust three-dimensional Dirac points appear away from Z point. In another work, Xiang et al. [233] reported colossal positive magnetoresistance in black phosphorus for P $\geq$ 1.2 GPa and observed non-trivial π Berry phase from the Shubnikov-de Haas oscillation measurement. These observed changes in black phosphorus at P = 1.2 GPa were attributed to electronic Lifshitz transition.

In this section, our goal is to understand the origin of dip (minima) observed experimentally in the line width of first order Raman modes A_g^1 , B_{2g} and A_g^2 of orthorhombic phase at 1.1 GPa (refer Figure 7.7). Secondly, we want to understand the observed anomalies in frequencies of B_{2g} and A_g^2 modes at 7.4 GPa and the origin of new modes (N1, N2 and N3) emerging within 4-11 GPa, where BP exhibits rhombohedral structure. These new modes show anomalous softening with pressure (refer Figure 7.8). Experimental results presented this section are performed by Prof. A. K. Sood's Group (IISc).

We determine electronic and vibrational spectra of BP as a function of pressure (upto 24 GPa) using first-principles calculations. We find a low pressure electronic topological transition at P $\sim$ 0.5 GPa, identified as the one from semiconductor to metal, and establish a strong topological character above $P = 0.5$ GPa.

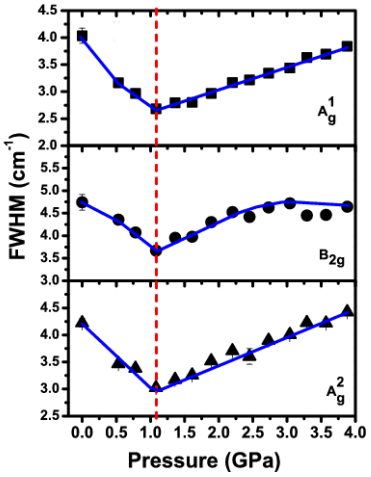

Figure 7.7: Pressure evolution of FWHM of various Raman modes. The vertical dashed lines indicate the phase transition pressures. The vertical dashed line indicates the metallic phase transition pressures. The solid blue line are the guide to the eye.

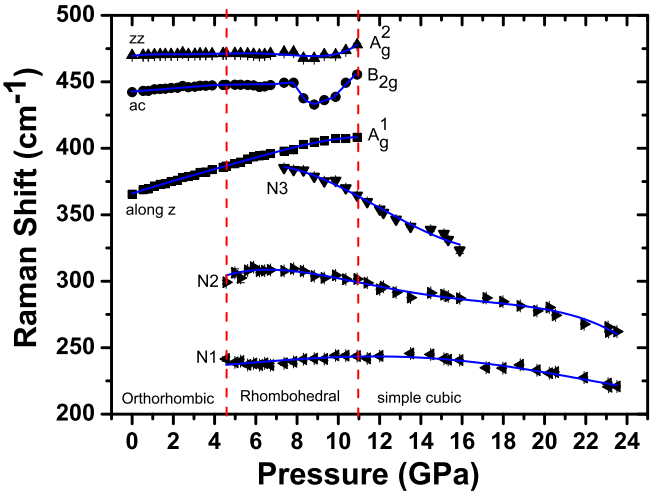

Figure 7.8: Pressure dependence of various phonon frequencies. The vertical dashed lines indicate the phase transition pressures. The solid blue line are the guide to the eye.

7.2.2 Methods

Our first-principles calculations are based on density functional theory (DFT) as implemented in Quantum ESPRESSO package [41], in which the interaction between ionic core and valence electrons modeled with norm-conserving pseudopotentials [168, 169]. The exchange-correlation energy of electrons is treated within a

generalized gradient approximation (GGA) with a functional form parameterized by Perdew, Burke and Ernzerhof [36]. We use an energy cutoff of 55 Ry to truncate the plane wave basis used in representing Kohn-Sham wave functions, and energy cutoff of 220 Ry for the basis set to represent charge density. Structures are relaxed to minimize energy till the magnitude of Hellman-Feynman force on each atom is less than 0.03 eV/Å. We include van der Waals (vdW) interaction with the parametrization given in Grimme scheme [56]. In self-consistent Kohn-Sham (KS) calculations of configurations of bulk black phosphorous with orthorhombic and rhombohedral unit cell, the Brillouin zone (BZ) integrations are sampled with a uniform mesh of 18x16x16 and 16x16x16 k-points respectively, and 32x32x32 mesh of k-points is used for calculation of electron-phonon coupling of both the structural forms. Phonon and dynamical matrices at Γ-point (q= (0, 0, 0)) as a function of lattice constant (or pressure) were determined using density functional linear response as implemented in Quantum ESPRESSO(QE) [41], which employs the Greens function method to avoid explicit calculations of unoccupied Khon-Sham states. Since DFT typically underestimates the electronic bandgap, we have used HSE functional [46] as implemented in QE to estimate the gaps accurately, with the mixing parameter of 0.25 and reciprocal space integration sampled on a 4x4x4 mesh of k-points. We calculated Z_2 topological invariant using Z2Pack code [234], which uses the ideas of time reversal polarization formulated in terms of hybrid Wannier charge centers [235, 236]. To determine the topological invariant (ν_0), we chose two time-reversal invariant planes ($k_z = 0$ and $k_z = 0.5$ planes) in the BZ, and tracked the evolution of the hybrid Wannier charge centers (WCCs) in each of the planes during an adiabatic cycle [235].

7.2.3 Structure and Electronic structure

The structure of BP consists of puckered layers, with a unit cell characterized by a stacking sequence ABA, where A and B label P layers (see Figure 7.9a). The puckered network is formed by phosphorus atoms with each atom covalently bonded to three neighboring atoms and layers are bound together by weak van der Waals interactions (see Figure 7.9b). Our optimized structural parameters of orthorhombic structure, a, b, c, d_1, d_2, α_1 and α_2 are 4.42Å, 3.32Å, 10.46Å, 2.224 Å, 2.244 Å, 96.34° and 102.09° respectively, in good agreement experimental values [237], where d_1 is the bond length of in-plane P atoms while d_2 defines the distance out-of-plane P atoms. α_2 and α_1 are the bond angles between d_1 and d_2 and two d_1 bonds respectively (Figure 7.9b). BP is a direct band gap semiconductor at Z-point (0.0, 0.0, 0.5) with a gap of 0.33 eV estimated with HSE functional (Figure 7.10a) in good agreement with experiment ($E_g = 0.35$ eV) whereas there is no gap observed at 0 GPa with GGA functions (refer Figure 7.10b).

7.2.4 Vibrational Signatures

The space group of BP in orthorhombic structure is $C_{mca} - D_{2h}$ with primitive cell containing 4 atoms. The optical modes at the BZ center (Γ point) are classified into following irreducible representations at Γ:

$$2A_g + A_u + B_{1g} + B_{1u} + 2B_{2g} + B_{2u} + B_{3g} \tag{7.4}$$

B_{1u} and B_{2u} are Infra Red active and A_g, B_{1g}, B_{2g} and B_{3g} are Raman active modes. Here, we focus on the changes in A_g^1, B_{2g} and A_g^2 modes with pressure. The other two modes, B_{1g} and B_{3g}^1, Raman active modes are very weak and difficult to separate from the background experimentally.

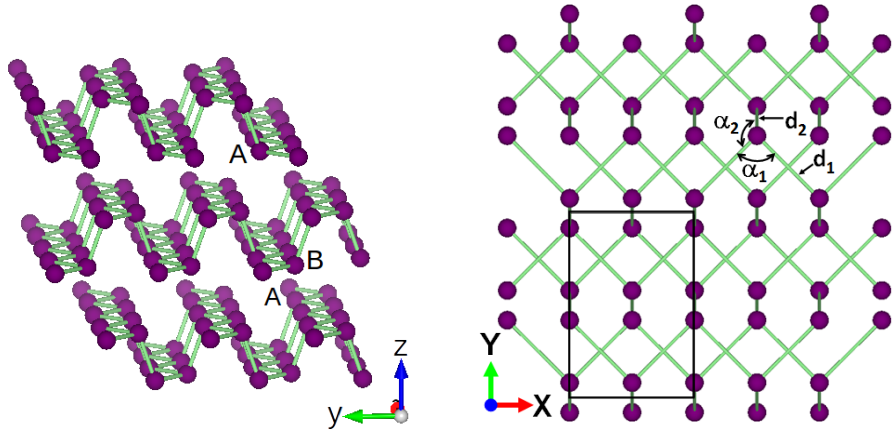

(a) (b)

Figure 7.9: Side (a) and top (b) views of the layered structure of bulk black phosphorous. d_1 and d_2 are the P-P bonds lengths. d_1 is the distance between two P atoms in a plane while d_2 is the nearest neighbor distance. α_1 is the bond angle between two d_1's and the bond angle between d_1 and d_1 is α_2.

7.2.5 Low pressure transition

The calculated frequencies of A_g^1, B_{2g} and A_g^2 are 453 cm^{-1}, 418 cm^{-1} and 354 cm^{-1}, which agree well with the observed frequencies of these modes. In our Raman experiments (see Figure 7.7), we observed anomalous changes in FWHM of A_g^1, B_{2g} and A_g^2 modes at 1.1 GPa. To capture this anomalies, we performed electron-phonon coupling calculations and find a dip (minima) at -1.5 GPa in the electron-phonon coupling of A_g^1 and A_g^2 modes as a function of pressure (Figure 7.11). We do not see any anomaly in the electron-phonon coupling of B_{2g} with pressure. A careful examination of electronic structure at -1.5 GPa show a semiconductor to semi-metal transition.

Since the anomalous change in FWHM can be an indicator of electronic topological transition (ETT) [161], and given the experimental observations of Xiang et al. [233] and theoretical study of Gong et al. [232], we studied electronic structure of black phosphorus as a function of hydrostatic pressure using highly accurate HSE

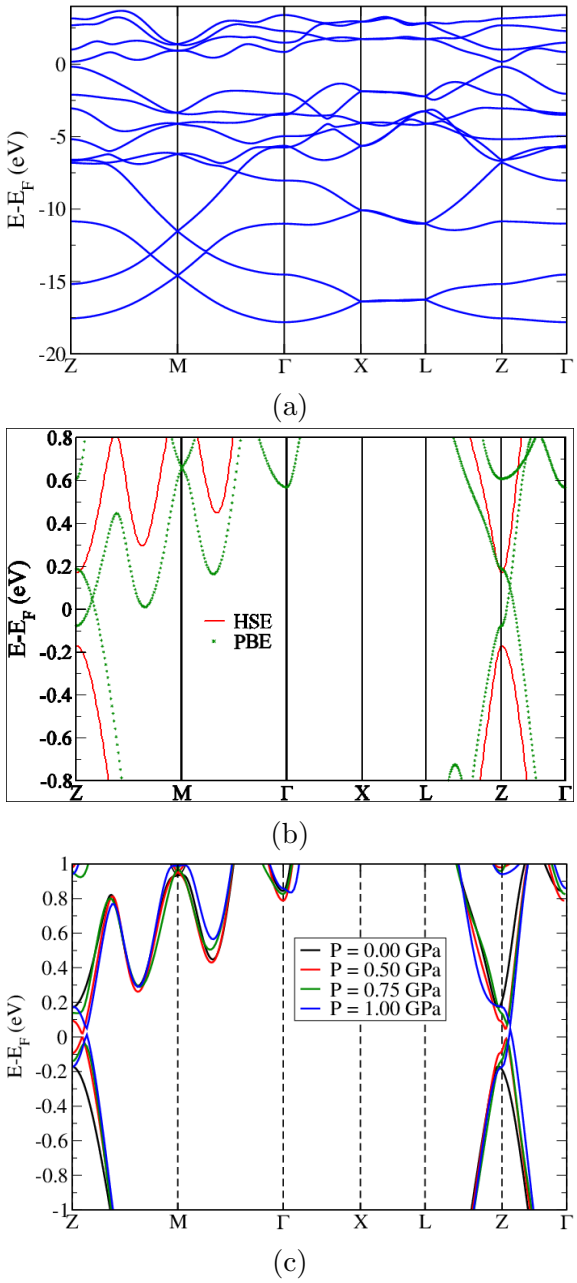

Figure 7.10: Electronic structure of BP in A11 phase. (a) Electronic structure of BP at $P = 0$ GPa calculated with HSE functionals. Note that we used Wannier functions [1] to plot band structure with HSE functionals. (b) Comparison of electronic structure near the gap obtained with HSE and PBE functionals at $P = 0$ GPa. BP exhibit a gap of 0.33 eV at Z-point, which is captured correctly with HSE functionals whereas PBE calculations gives no gap. (c) Electronic structure near the gap obtained with HSE functionals at different pressures.

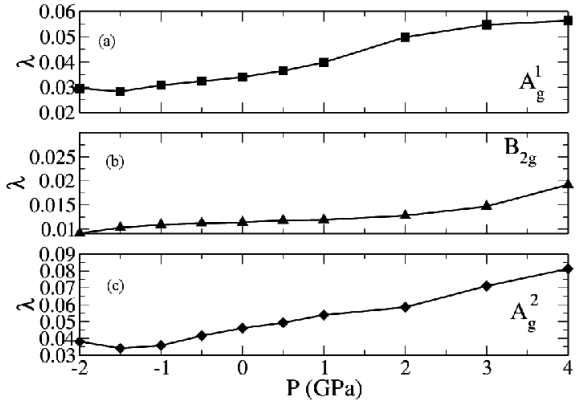

Figure 7.11: Variation in the calculated electron-phonon coupling of Raman active modes with pressure (a) A_g^1, (b) B_{2g} and (c) A_g^2 modes of BP in A11 phase.

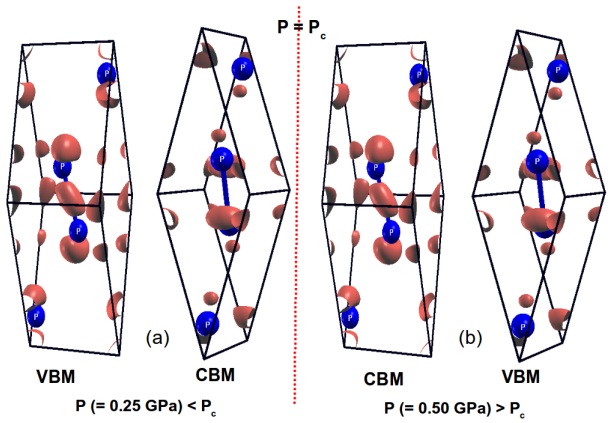

Figure 7.12: Band inversion during pressure induced electronic topological transition (ETT) in BP. Isosurfaces of charge densities associated with electronic states at valance band maximum and conduction band minimum at Γ-point (a) before and (b) after the ETT revealing band inversion across this transition.

calculations. Our calculations show that band inversion occurs at Z point between $P = 0.25$ and $P = 0.50$ GPa (Figure 7.12) following which the band gap opens up above $P \geq 0.5$ GPa (refer Figure 7.10c), which is in contrast to that earlier DFT study (within GGA and mBJ functional) where persistence of robust band crossing is reported after band inversion [232]. We use HSE calculations to predict the correct transition pressure as with GGA functionals transition pressure is predicted at -1.5 GPa. Our estimate of the transition pressure with HSE functionals is P $\sim$ 0.5

GPa, in agreement with theoretically predicted transition pressure (P $\sim$ 0.6 GPa) by Ruixiang *et. al* [238].

Although earlier studies [232, 233] reported pressure induced electronic topological transition (Lifshitz transition) in black phosphorus following band inversion near P = 1.2 GPa, the nature of electronic topology of the bulk has not been clear. To investigate the electronic topology of black phosphorus, we determined the Z_2 topological invariant (ν_0) as a function of pressure (see Figure 7.13). We find that $\nu = 0$ for $P < 0.5$ GPa, whereas $\nu_0 = 1$ for $P \geq 0.5$ GPa signifying Z_2 topological insulating nature of black phosphorus above 0.5 GPa. Thus, we attribute the anomalous changes in FWHM of Raman active modes to the pressure induced electronic topological phase transition. The observation of non-trivial π Berry phase and colossal magneto-resistance for P>1.2 GPa in experiment [233] are also consistent with the fact that black phosphorus becomes topologically non-trivial for $P > 0.5$ GPa. The discrepancy between our calculated transition pressure (0.5 GPa) and previously reported ones (1.2 GPa) falls within the typical errors of DFT calculations.

7.2.6 Anomalies at high pressure transition: structural origin

In this section, change in frequencies and electron-phonon coupling with pressure is studied using PBE functionals. At P= 0 GPa, our calculations do not capture the correct gap with PBE fuctionals as shown in previous subsection. Thus, to capture the semiconductor to semimetal transition, we have to apply the negative pressure. Estimated transition pressure is P $\sim$ -1.5 GPa with PBE functionals. BP is a complex material due to its in-plane and out-of-plane anisotropies. We could not stabilize it below P = -2 GPa: it goes to another structural form which is even lower in energy that of the structure at P = 0 GPa. The electronic structure

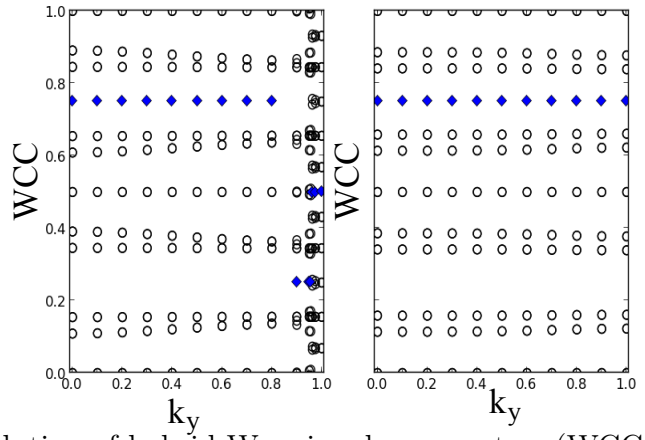

Figure 7.13: Evolution of hybrid Wannier charge centers (WCCs) along y-direction (marked by circle) and their largest gap function (blue rhombus) for (a) k_z =0 plane and (b) k_z=0.5 plane. It is clear show that $k_z = 0$ plane is topologically non-trivial whereas k_z=0.5 plane is topologically trivial.

of this new structural form is quite different from the structure at P = 0 GPa. It is metallic in nature whereas structure at P = 0 GPa is semiconductor. BP exhibits orthorhombic structure from 0-4.6 GPa. In this pressure range, frequencies of all the Raman active mode are seen to harden in experiments (see Figure 7.8). Our theoretical calculations show that only A_g^1 mode hardens whereas other two modes softens anomalously. This softening and hardening can be explained with the variation of internal structural parameters with pressure. A careful examination of frequency vs. P graph of A_g^2 and B_{2g} shows that the observed anomalies at P = 7.4 GPa (see Figure 7.8) are captured at P = 10 GPa (refer Figure 7.14) in our calculations. These modes soften anomalously: especially B_{2g} mode softens by $\sim$ 80 cm^{-1} at 10 GPa and starts hardening beyond this pressure (see Figure 7.14). A_g^2 mode softens by $\sim$ 30 cm^{-1} at 10 GPa. At 10 GPa, BP transforms to the rhombohedral structure. We suggest that the anomalies seen in experiments in the rhombohedral phase are basically due to co-existence of orthorhombic and rhombohedral structures.

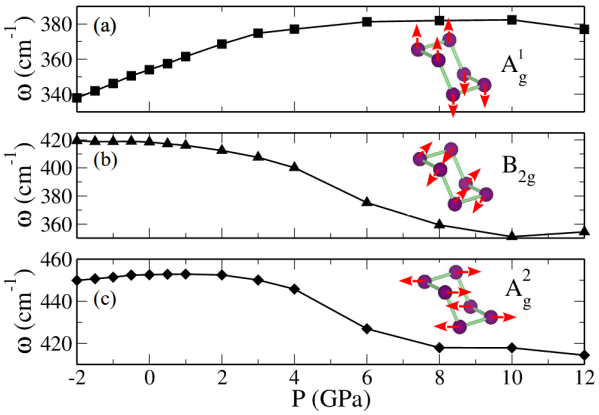

Figure 7.14: Change in the frequencies of Raman active modes (a) A_g^1, (b) B_{2g} and (c) A_g^2 modes of BP in A11 phase with pressure. Insets of (a), (b) and (c) show atomic displacements in these Raman active modes.

Atomic vibration of A_g^1 mode (refer Figure 7.14) involve stretching the d_2 bond. From the variation of d_2 bond with pressure (see Figure 7.15a), we find that d_2 decreases monotonically with pressure and the Δd_2 is 0.04 Å. As a result, A_g^1 hardens with pressure. The atomic vibration of B_{2g} (refer Figure 7.14) affects bond angle, α_2. From Figure 7.15(b), α_2 decreases with increasing pressure. We find that the frequency of B_{2g} mode decreases with pressure in the same fashion as α_2, and observe a sudden drop in α_2 from 4 GPa to 6 GPa, which is also evident in the frequency of B_{2g} as a function of pressure (see Figure 7.14b). Atomic displacements of A_g^2 mode (refer Figuure 7.14) involve stretching of d_1 bond. d_1 decreases with pressure upto 3 GPa, and starts increasing from 3-6 GPa, and subsequently decreases with pressure upto 12 GPa (see Figure 7.15a). In this case, Δd_1 with pressure is much smaller than Δd_2 which is also reflected in softening of B_{2g} and A_g^2. As a result of variation of d_1 with pressure, A_g^2 softens with pressure and this softening is less than the softening observed in B_{2g}.

The space group of BP in rhombohedral structure is $R-3m-D_{3d}(-3m)$ with primitive cell containing 2 atoms. The optical modes at the Brillouin zone center

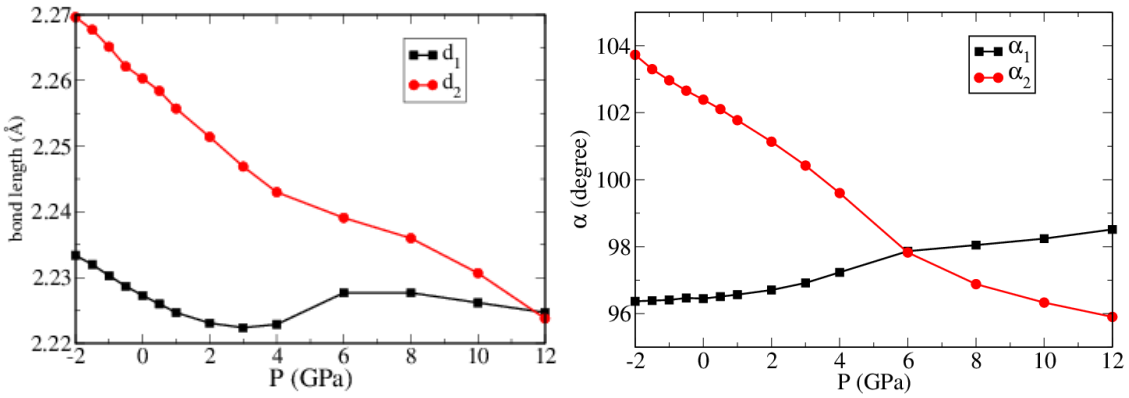

(a) (b)

Figure 7.15: Evolution of bond lengths (a) and bond angles (b) of BP in A11 phase with pressure.

(Γ point) are classified into following irreducible representation:

$$A_{1g} + A_{2g} + E_g + A_{1u} + A_{2u} + E_u \tag{7.5}$$

A_{1g} and E_g are the Raman active mode and A_{2u} and E_u are infrared active mode. Rhombohedral phase of BP is also known as the A7 phase. A7 is the high pressure phase, it appears at $P \geq 4.6$ GPa and survives till $P = 11$ GPa. Beyond this pressure ($P = 11$ GPa), BP transforms to the cubic structure, which (a high pressure phase) is stable upto $P = 24$ GPa. The frequencies of A_{1g} and E_g modes are 350 cm^{-1} and 255 cm^{-1} at 4 GPa. There are three Raman active modes which appear in rhombohedral phase (Figure 7.8). The frequencies of these modes are N1, N2 and N3 are $\sim$ 250 cm^{-1}, 300 cm^{-1} and 380 cm^{-1} respectively. We identify N3 mode as A_{1g} mode and N1 as E_g. From first-principles calculations, rhombohedral structure is stable from 4 GPa to 12 GPa, unstable modes start appearing in phonon dispersion beyond this pressure. With increasing pressure, A_{1g} and E_g modes soften consistent with softening of N3 and N1 modes (Figure 7.16(a, b) and Figure 7.8).

N2 mode can appear due to defects, which can lead to splitting in the degeneracy

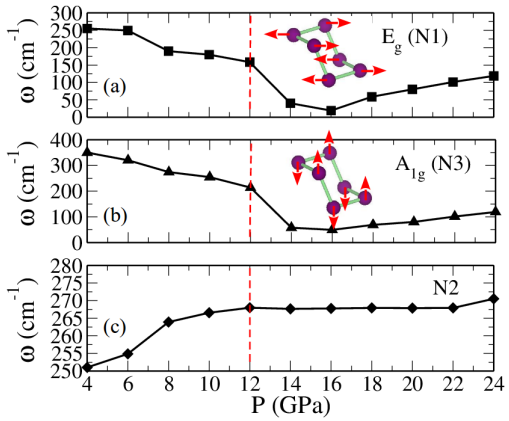

Figure 7.16: Change in the calculated frequencies of Raman active modes with pressure of BP in A7 phase, (a) E_g mode, (b) A_{1g} mode and (c) N2 mode (Insets of (a) and (b) showing their atomic displacements). Note that N1, N2 and N3 are the modes observed in experiments. Here N2 shows the frequency of longitudinal acoustic mode at Z-point of the Brillouin zone of A7 phase.

of frequencies of E_g modes. We have investigated frequency of longitudinal acoustic mode at Z-point with pressure which hardens with pressure whereas N2 softens with pressure.

7.2.7 Conclusions

Using first-principles calculations, we find that the low pressure phase transition in BP at P $\sim$ 0.5 GPa is a semiconductor to semimetal transition. Our calculations of the Z_2 invariant confirm the change in electronic topology making a transition from band to topological insulating state. We uncover the origin of anomalous softening of Raman active modes in the variation of internal structural parameters with pressure, and identify the symmetry of the new modes appearing in experiments.

Chapter 8

Summary

The central theme of this dissertation has been to explore the role of defects and effect of external fields (*e.g.* pressure and charge doing) in modification of physical properties and behavior of bulk and two dimensional materials. The materials studied in this thesis are not only technologically important, but are also fundamentally interesting as they exhibit unusual phenomena involving fascinating physics. We have employed first-principles density theoretical calculations and modeling in our analysis.

Grain boundaries are always present in materials and have particularly interesting consequences to the properties of 2D materials. We present a comparative study of changes in the structure and vibrational properties associated with two types of interfaces or grain boundaries (GB) (i) stacking and (ii) growth faults in h-BN and graphene and label them with the polygonal ring-structure. We identify that a 4:8 GB (stacking fault) is more stable in h-BN, while a 5:5:8 GB (growth fault) is relatively more stable in graphene. We predicted four novel GBs: 6:5:8:4:8:5 GB in graphene and 4:4, 6:5:8:4:8:5 N-N and 6:5:8:4:8:5 B-B GBs in h-BN. We reported a novel GB in graphene, which is 6:5:8:4:8:5 GB, having the lowest energy among all the four GBs, and should therefore be common and relevant to experiment. Our

work highlights the remarkable diversity in the structures of grain boundaries in h-BN and graphene. We show that grain boundaries intrinsically cause rippling and wrinkles in the h-BN sheet and affect the electronic structure greatly. We identified the vibrational signatures of these GBs, specifically hardening and softening (frequency shifts) of A_2'' and E′ modes, which will be useful for the characterization of these interfaces by IR and Raman spectroscopies. Electronic signature of the lowest energy 4:8 GB of h-BN is in the charge accumulation localized at the interface, which accessible to scanning tunneling microscope.

Among 2-D materials planar defects can be found in materials such as MX_2 compounds (M= (Mo, W); X= (S, Se)) whose monolayers consist of 2 or 3 atomic planes. Upon introduction of a planar defect, MX_2 compounds makes transition from insulator (2H-phase) to metal (1T-phase) because of increase in the covalency of M and X atoms. We have determined the energies and electronic structure of the states along the transition pathway connecting $1H$ and c1T structures of monolayers of MX_2 (M= Mo, W and X= S, Se). We find that the c1T structure is typically higher in energy by 0.7-0.9 eV/f.u. than the $1H$ structure. Secondly, an energy barrier associated with this transition through glide of a plane of X atom is about 1.5 to 1.7 eV. We have shown that the c$1T$ polymorphic structure is unstable, exhibiting instabilities at the valley point K and zone boundary point M. These structural instabilities lead to symmetry and energy lowering distortions of the $c1T$ structure to form $\sqrt{3}$x$\sqrt{3}$ (for K-point) and $\sqrt{3}$x1 (for M-point) stable superstructures respectively. The $\sqrt{3}\times1$ structure associated with dimerization of metal atoms remains metallic, while the $\sqrt{3}\times\sqrt{3}$ superstructure exhibits a nonzero electronic band gap arising from strong trimerization of metal atoms. The $\sqrt{3}\times\sqrt{3}$ structure of (Mo, W)(S, Se)$_2$ exhibits a spontaneous polarization (0.25-0.3 μC/cm^2) along the direction perpendicular to the sheet, making them the thinnest known ferroelectrics. However, the $\sqrt{3}\times\sqrt{3}$

structure is (a) more stable than the $\sqrt{3}\times 1$ structure, and (b) exhibits a stable dipolar domain structure only in MoS_2. Thus, MoS_2 is the only suitable candidate for possible use in the *dipolectronic* devices. As a result of vicinity of these compounds to metal-semiconductor and ferroelectric transitions, all of them exhibit anomalous responses to an electric field.

Due to variety of 1T structures exhibited by TMX_2 compounds, the precise nature of 1T-phase occuring in experiment is not clear. Our work prove into the mystery of precise atomic and electronic structure of the 1T phase of 2D MoS_2, which is known to have properties that are relevant to its applications. This meta-stable phase is known to occur in nano-scale regions of commonly grown samples of 2D MoS_2. We used self-energy corrected first-principles calculations of electronic structure to determine its electronic nature, which along with experiments by Prof. D. D. Sarma (IISc), show that the 1T phaseof 2-D MoS2 has a $2a \times a$ super-structure with Mo dimerization, and exhibits a band-gap of 90 meV.

In our work on photo-catalytic properties of TMX_2 for water splitting, we found that (i) $MoSe_2$ has a lower work function in each of the 1T and 2H structures in comparison to MoS_2 and (ii) 1T-structure exhibits lower work function than the 2H-structure for each MoX_2 (X= S and Se). These result in easy transfer of electron from the $MoSe_2$ substrate to reduce proton, and hence $MoSe_2$ is more efficient in catalysis of hydrogen evolution reaction than MoS_2. This is also reflected in our analysis of binding energies of H at $MoSe_2$ edges.

We have analyzed the pressure induced semiconductor to semi-metal transition at ~ 8 GPa and a Lifshitz transition at ~ 20 GPa in 2H-$MoTe_2$ with first-principles density functional theoretical calculations (in complement to Raman measurements by Prof. Sood's group). The signatures of semiconductor to semimetal and the Lifshitz transitions are carried by the frequencies of the first order A_{1g} and E^1_{2g} Raman modes observed in experiments and theory. The occurrence of a maximum in

the integrated ratio of the A_{1g} and E^1_{2g} modes arises from a non-monotonous change in the Raman tensor of E^1_{2g} mode with pressure. We find that pressure influences the electron-phonon of A_{1g} most strongly, and Raman active modes generally harden with increasing pressure, and electron phonon coupling increases under compression due to changes in the Fermi surface. We believe that our findings will be useful in further studies of high pressure and low temperature resistivity experiments to capture the anomalies near the Lifshitz transition.

We presented structural, electronic and transport properties of the three polymorphs of $MoTe_2$, determining the effects of Te vacancies. We show that the pristine 2H-$MoTe_2$ (bulk-form) is an indirect gap semiconductor, whereas the 1T' and Td forms of $MoTe_2$ are semi-metallic. In the presence of Te vacancies, 2H form shows reduction in the indirect semiconducting gap, whereas the other two forms become more metallic. The observed trends in transport properties can be explained with theory only by including the effects of Te-vacancies and incipient electron doping. Thus, Te-vacancies in $MoTe_2$ essentially govern the trends in the observed temperature-dependent electronic transport properties of $MoTe_2$.

We presented a comparative analysis of electronic structure and vibrational properties of WTe_2 in its monolayered and bulk Td forms. The importance of spin-orbit coupling in accurate description of its electronic structure particularly near the Fermi-level is highlighted in this work. We assigned the symmetry labels to the observed experimental Raman active peaks with symmetry analysis and estimation of Raman tensor. We also highlighted the connection of the Td structure with $1T$ form of layered metal dichalcogenides, and explained its stability in terms of the electronic and vibrational properties of the c1T form. We found qualitative agreement between experimental and calculated results of thermal conductivity and electrical conductivity as a function of T. The experimentally observed n-p crossover in the Seebeck coefficient as a function of T in experiments is likely due to defects and

incipient doping along with structural changes.

Our work uncovered a remarkable electron-hole asymmetry in the coupling between charge carriers with phonons in phosphorene: phonons with A_g symmetry couple much more strongly with electrons than with holes. Further, only the phonons (A_g) preserving the symmetry of the lattice couple strongly with electrons. Our first-principles calculations reveal that the electron-hole asymmetry arises from rather different orbital characters of conduction and valence bands involving π and σ bonding states respectively.

Using first-principles calculations, we found that the observed low pressure phase transition in black phosphorous at P $\sim$ 0.5 GPa is a semiconductor to semimetal transition. Our calculations of the Z_2 invariant confirmed the change in electronic topology making a transition from band to topological insulating or semimetallic state. We showed that origin of anomalous softening of Raman active modes lies in the variation of internal structural parameters with pressure, and identified the symmetry of the new modes appearing in experiments.

We have summarized the work in this thesis in a schematic (see Fig. 8.1) that brings out the commonality and central theme of the topics covered. In summary, we highlighted how various defects and external fields govern the properties of 2D layered and bulk materials, giving rise to unexpected physical phenomena and fascinating behavior. Our work should be helpful in experimental characterization of these materials and devices based on them.

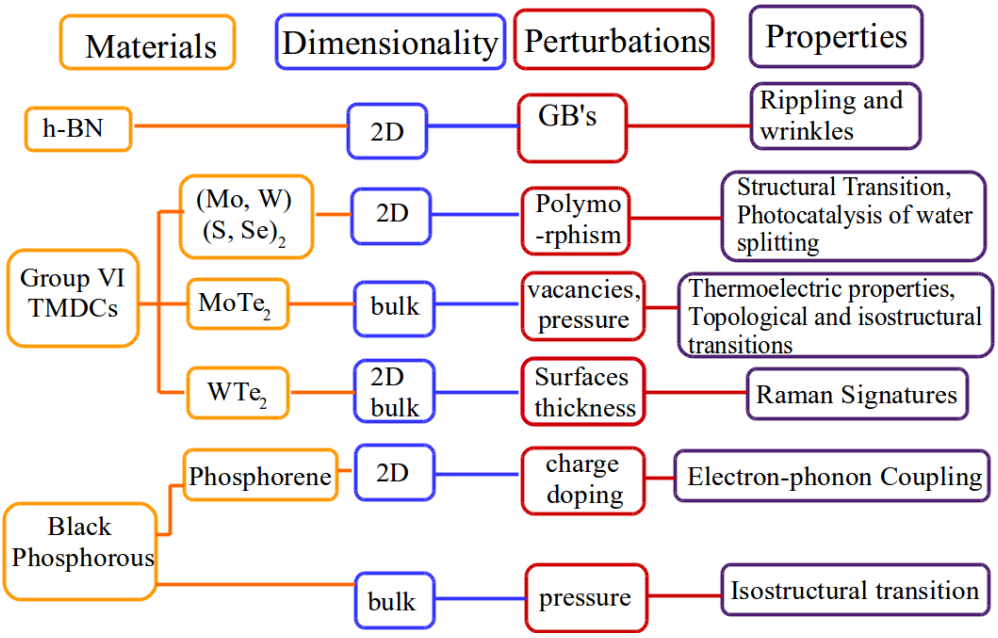

Figure 8.1: A schematic summarizing our work presented in this thesis

Bibliography

[1] A. A. Mostofi *et al.*, Computer Physics Communications **185**, 2309 (2014).

[2] K. S. Novoselov *et al.*, Science **306**, 666 (2004).

[3] A. Singh and U. V. Waghmare, Phys. Chem. Chem. Phys. **16**, 21664 (2014).

[4] A. Singh, S. N. Shirodkar, and U. V. Waghmare, 2D Materials **2**, 035013 (2015).

[5] S. N. Shirodkar and U. V. Waghmare, Phys. Rev. Lett. **112**, 157601 (2014).

[6] B. Chakraborty *et al.*, 2D Materials **3**, 015008 (2016).

[7] M. K. Jana *et al.*, Journal of Physics: Condensed Matter **27**, 285401 (2015).

[8] M. M. Ugeda *et al.*, Nat Phys **12**, 92 (2016).

[9] C. Xu *et al.*, Nat Mater **14**, 1135 (2015).

[10] J. A. Flores-Livas and A. Sanna, Phys. Rev. B **91**, 054508 (2015).

[11] Y. Ge, W. Wan, F. Yang, and Y. Yao, New Journal of Physics **17**, 035008 (2015).

[12] K. Rana, J. Singh, and J.-H. Ahn, J. Mater. Chem. C **2**, 2646 (2014).

[13] K. S. Novoselov *et al.*, Nature **438**, 197 (2005).

[14] Y. Zhang, Y.-W. Tan, H. L. Stormer, and P. Kim, Nature **438**, 201 (2005).

[15] F. Schwierz, Nat Nano **5**, 487 (2010).

[16] Q. H. Wang *et al.*, Nat Nano **7**, 699 (2012).

[17] C. Palacios-Berraquero *et al.*, Nature Communications **7**, 12978 (2016).

[18] N. Zibouche, A. Kuc, J. Musfeldt, and T. Heine, Annalen der Physik **526**, 395 (2014).

[19] W. Yang *et al.*, Nano Letters **16**, 1560 (2016).

[20] B. Radisavljevic *et al.*, Nat. Nanotechnol. **6**, 147 (2011).

[21] Y. Yoon, K. Ganapathi, and S. Salahuddin, Nano Letters **11**, 3768 (2011).

[22] H. Liu *et al.*, ACS Nano **8**, 4033 (2014).

[23] V. Tran, R. Soklaski, Y. Liang, and L. Yang, Phys. Rev. B **89**, 235319 (2014).

[24] A. Castellanos-Gomez *et al.*, 2D Materials **1**, 025001 (2014).

[25] L. Li *et al.*, Nat Nano **9**, 372 (2014).

[26] M. Buscema *et al.*, Nature Communications **5**, 4651 (2014).

[27] J. Qiao *et al.*, Nature Communications **5**, 4475 (2014).

[28] C. Jin, F. Lin, K. Suenaga, and S. Iijima, Phys. Rev. Lett. **102**, 195505 (2009).

[29] J. Lahiri *et al.*, Nat. Nanotechnol. **5**, 326 (2010).

[30] P. Y. Huang *et al.*, Nature **469**, 389 (2011).

[31] *Models of Disorder: The Theoretical Physics of Homogeneously Disordered Systems*, edited by J. M. Ziman (Cambrige University Press, Cambridge, 1979).

[32] *Reactions and Characterization of Solids*, edited by S. E. Dann (The Royal Society of Chemistry, Cambridge, 2000).

[33] M. U. Kahaly, S. P. Singh, and U. V. Waghmare, Small **4**, 2209 (2008).

[34] W. Kohn and L. J. Sham, Phys. Rev. **140**, A1133 (1965).

[35] P. Hohenberg and W. Kohn, Phys. Rev. **136**, B864 (1964).

[36] J. P. Perdew, K. Burke, and M. Ernzerhof, Phys. Rev. Lett. **77**, 3865 (1996).

[37] J. P. Perdew and A. Zunger, Phys. Rev. B **23**, 5048 (1981).

[38] A. St.-Amant, W. D. Cornell, P. A. Kollman, and T. A. Halgren, Journal of Computational Chemistry **16**, 1483 (1995).

[39] J. P. Perdew, P. Ziesche, and H. Eschrig, *Electronic structure of solids 91* (Akademie Verlag, Berlin, 1991), Vol. 11.

[40] D. Vanderbilt, Phys. Rev. B **41**, 7892 (1990).

[41] P. Giannozzi *et al.*, Journal of Physics: Condensed Matter **21**, 395502 (2009).

[42] X. Gonze *et al.*, Computational Materials Science **25**, 478 (2002).

[43] P.-O. Widmark, P.-Å. Malmqvist, and B. O. Roos, Theoretica chimica acta **77**, 291 (1990).

[44] P.-O. Widmark, B. J. Persson, and B. O. Roos, Theoretica chimica acta **79**, 419 (1991).

[45] S. G. Louie, K.-M. Ho, and M. L. Cohen, Phys. Rev. B **19**, 1774 (1979).

[46] J. Heyd, G. E. Scuseria, and M. Ernzerhof, The Journal of Chemical Physics **118**, 8207 (2003).

[47] C. Pisani and R. Dovesi, International Journal of Quantum Chemistry **17**, 501 (1980).

[48] K. N. Kudin and G. E. Scuseria, Phys. Rev. B **61**, 16440 (2000).

[49] L. D. Landau, Journal of Experimental and Theoretical Physics **30**, 1058 (1956).

[50] L. D. Landau, Journal of Experimental and Theoretical Physics **32**, 59 (1957).

[51] A. B. M. V. M. Galitskii, Journal of Experimental and Theoretical Physics **34**, 139 (1958).

[52] V. M. Galitskii, Journal of Experimental and Theoretical Physics **7**, 104 (1958).

[53] P. Hobza, J. poner, and T. Reschel, Journal of Computational Chemistry **16**, 1315 (1995).

[54] M. J. Allen and D. J. Tozer, The Journal of Chemical Physics **117**, 11113 (2002).

[55] I. E. Dzyaloshinskii, E. M. Lifshitz, and L. P. Pitaevskii, Phys. Usp. **4**, 153 (1961).

[56] S. Grimme, Journal of Computational Chemistry **27**, 1787 (2006).

[57] A. Tkatchenko and M. Scheffler, Phys. Rev. Lett. **102**, 073005 (2009).

[58] H. W. Kroto *et al.*, Nature **318**, 162 (1985).

[59] S. Iijima, Nature **354**, 56 (1991).

[60] A. K. Geim and K. S. Novoselov, Nat. Mater. **6**, 183 (2007).

[61] Z. Chen *et al.*, Advanced Materials **26**, 339 (2014).

[62] H. Jiang, P. S. Lee, and C. Li, Energy Environ. Sci. **6**, 41 (2013).

[63] L. S. Panchakarla *et al.*, Advanced Materials **21**, 4726 (2009).

[64] D. P. Hashim *et al.*, Sci. Rep. **2**, 363 (2012).

[65] A. Stone and D. Wales, Chemical Physics Letters **128**, 501 (1986).

[66] X. Li, X. Wu, X. C. Zeng, and J. Yang, ACS Nano **6**, 4104 (2012).

[67] S. Stankovich *et al.*, Carbon **45**, 1558 (2007).

[68] Y. Shi *et al.*, Nano Lett. **10**, 4134 (2010).

[69] Y. Si and E. T. Samulski, Nano Lett. **8**, 1679 (2008).

[70] K. K. Kim *et al.*, Nano Lett. **12**, 161 (2012).

[71] S. J. Chae *et al.*, Advanced Materials **21**, 2328 (2009).

[72] W. Auäwter, H. U. Suter, H. Sachdev, and T. Greber, Chemistry of Materials **16**, 343 (2004).

[73] J. C. Meyer *et al.*, Nano Lett. **8**, 3582 (2008).

[74] A. Nag *et al.*, ACS Nano **4**, 1539 (2010).

[75] A. Zobelli *et al.*, Nano Lett. **6**, 1955 (2006).

[76] S. N. Shirodkar and U. V. Waghmare, Phys. Rev. B **86**, 165401 (2012).

[77] S. Bhowmick and U. V. Waghmare, Phys. Rev. B **81**, 155416 (2010).

[78] J. Červenka and C. F. J. Flipse, Phys. Rev. B **79**, 195429 (2009).

[79] N. M. R. Peres, F. Guinea, and A. H. Castro Neto, Phys. Rev. B **73**, 125411 (2006).

[80] O. V. Yazyev and S. G. Louie, Nat. Mater. **9**, 806 (2010).

[81] A. Mesaros *et al.*, Phys. Rev. B **82**, 205119 (2010).

[82] Y. Liu and B. I. Yakobson, Nano Lett. **10**, 2178 (2010).

[83] R. Grantab, V. B. Shenoy, and R. S. Ruoff, Science **330**, 946 (2010).

[84] S. Malola, H. Häkkinen, and P. Koskinen, Phys. Rev. B **81**, 165447 (2010).

[85] J. Cervenka, M. I. Katsnelson, and C. F. J. Flipse, Nat Phys **5**, 840 (2009).

[86] H. F. Bettinger, T. Dumitrică, G. E. Scuseria, and B. I. Yakobson, Phys. Rev. B **65**, 041406 ((2002)).

[87] Y. Liu, X. Zou, and B. I. Yakobson, ACS Nano **6**, 7053 (2012).

[88] O. V. Yazyev and S. G. Louie, Phys. Rev. B **81**, 195420 (2010).

[89] J. M. Carlsson, L. M. Ghiringhelli, and A. Fasolino, Phys. Rev. B **84**, 165423 (2011).

[90] T.-H. Liu, G. Gajewski, C.-W. Pao, and C.-C. Chang, Carbon **49**, 2306 (2011).

[91] W. Zhou *et al.*, Nano Lett. **13**, 2615 (2013).

[92] J. E. Northrup, J. Neugebauer, and L. T. Romano, Phys. Rev. Lett. **77**, 103 (1996).

[93] M. S. C. Mazzoni, R. W. Nunes, S. Azevedo, and H. Chacham, Phys. Rev. B **73**, 073108 (2006).

[94] M. Topsakal, E. Aktürk, and S. Ciraci, Phys. Rev. B **79**, 115442 (2009).

[95] R. Geick, C. H. Perry, and G. Rupprecht, Phys. Rev. **146**, 543 (1966).

[96] J. Tersoff and D. R. Hamann, Phys. Rev. B **31**, 805 (1985).

[97] L. Rapoport *et al.*, Wear **225**, 975 (1999).

[98] L. Rapoport, N. Fleischer, and R. Tenne, J. Mater. Chem. **15**, 1782 (2005).

[99] U. Gupta *et al.*, APL Mat. **2**, 092802 (2014).

[100] D. J. Late *et al.*, ACS Nano **7**, 4879 (2013).

[101] J. J. Auborn *et al.*, J. Electrochem. Soc. **134**, 580 (1987).

[102] J. Rouxel and R. Brec, Annu. Rev. Mater. Sci. **16**, 137 (1986).

[103] A. J. Jacobson, R. R. Chianelli, and M. S. Whittingham, J. Electrochem. Soc. **126**, 2277 (1979).

[104] M. Chhowalla *et al.*, Nat. Chem. **5**, 263 (2013).

[105] Q. H. Wang *et al.*, Nat. Nanotechnol. **7**, 699 (2012).

[106] O. Lopez-Sanchez *et al.*, Nat. Nanotechnol. **8**, 497 (2013).

[107] R. Cheng *et al.*, Nano Letters **14**, 5590 (2014).

[108] R. S. Sundaram *et al.*, Nano Lett. **13**, 1416 (2013).

[109] C. Rao, U. Maitra, and U. V. Waghmare, Chem. Phys. Lett. **609**, 172 (2014).

[110] D. M. Guzman and A. Strachan, J. Appl. Phys. **115**, 243701 (2014).

[111] K.-A. N. Duerloo, Y. Li, and E. J. Reed, Nat. Commun. **5**, 4214 (2014).

[112] Y.-C. Lin, D. O. Dumcenco, Y.-S. Huang, and K. Suenaga, Nat. Nanotechnol. **9**, 391 (2014).

[113] J. Wilson and A. Yoffe, Adv. Phys. **18**, 193 (1969).

[114] K. F. Mak *et al.*, Phys. Rev. Lett. **105**, 136805 (2010).

[115] U. Maitra *et al.*, Angew. Chem. Int. Ed. **52**, 13057 (2013).

[116] J. Heising and M. G. Kanatzidis, J. Am. Chem. Soc. **121**, 638 (1999).

[117] M. Lazzeri and F. Mauri, Phys. Rev. Lett. **90**, 036401 (2003).

[118] M. J. Mehl, D. A. Papaconstantopoulos, N. Kioussis, and M. Herbranson, Phys. Rev. B **61**, 4894 (2000).

[119] K. P. O'Donnell and X. Chen, Appl. Phys. Lett. **58**, 2924 (1991).

[120] S. Sugai and T. Ueda, Phys. Rev. B **26**, 6554 (1982).

[121] C. Rovira and M. H. Whangbo, Inorg. Chem. **32**, 4094 (1993).

[122] F. Wypych, T. Weber, and R. Prins, Chem. Mater. **10**, 723 (1998).

[123] G. Henkelman and H. Jónsson, J. Chem. Phys **113**, 9978 (2000).

[124] K. M. Rabe, in *Functional Metal Oxides* (Wiley-VCH Verlag GmbH & Co. KGaA, Weinheim, 2013), pp. 221–244.

[125] Y. Lin *et al.*, Nano Lett. **14**, 5569 (2014).

[126] M. Born and K. Huang, *Dynamical Theory of Crystal Lattices* (Oxford: Oxford University Press, Amen House, London E.C.4, 1954), bibliography: p. 432.

[127] U. V. Waghmare, N. A. Spaldin, H. C. Kandpal, and R. Seshadri, Phys. Rev. B **67**, 125111 (2003).

[128] K. F. Mak, K. He, J. Shan, and T. F. Heinz, Nat Nano **7**, 494 (2012).

[129] T. Cao *et al.*, Nature Communications **3**, 887 (2012).

[130] R. G. Dickinson and L. Pauling, Journal of the American Chemical Society **45**, 1466 (1923).

[131] I. Song, C. Park, and H. C. Choi, RSC Adv. **5**, 7495 (2015).

[132] G. Eda *et al.*, Nano Letters **11**, 5111 (2011).

[133] M. Acerce, D. Voiry, and M. Chhowalla, Nat Nano **10**, 313 (2015).

[134] D. Voiry *et al.*, Nano Letters **13**, 6222 (2013).

[135] R. Kappera *et al.*, Nat Mater **13**, 1128 (2014).

[136] G. Kresse and J. Furthmüller, Computational Materials Science **6**, 15 (1996).

[137] G. Kresse and J. Furthmüller, Phys. Rev. B **54**, 11169 (1996).

[138] P. E. Blöchl, Phys. Rev. B **50**, 17953 (1994).

[139] G. Kresse and D. Joubert, Phys. Rev. B **59**, 1758 (1999).

[140] M. Shishkin and G. Kresse, Phys. Rev. B **74**, 035101 (2006).

[141] M. A. Py and R. R. Haering, Canadian Journal of Physics **61**, 76 (1983).

[142] P. J. Mulhern, Canadian Journal of Physics **67**, 1049 (1989).

[143] D. Yang *et al.*, Phys. Rev. B **43**, 12053 (1991).

[144] F. Wypych, T. Weber, and R. Prins, Chemistry of Materials **10**, 723 (1998).

[145] G. Onida, L. Reining, and A. Rubio, Rev. Mod. Phys. **74**, 601 (2002).

[146] L. Hedin, Phys. Rev. **139**, A796 (1965).

[147] M. S. Hybertsen and S. G. Louie, Phys. Rev. B **34**, 5390 (1986).

[148] R. W. Godby, M. Schlüter, and L. J. Sham, Phys. Rev. B **37**, 10159 (1988).

[149] B. Hinnemann *et al.*, Journal of the American Chemical Society **127**, 5308 (2005).

[150] X. Zong *et al.*, Chem. Commun. **30**, 4536 (2009).

[151] J. Yang and H. S. Shin, J. Mater. Chem. A **2**, 5979 (2014).

[152] X. Zong *et al.*, Journal of the American Chemical Society **130**, 7176 (2008).

[153] M. A. Lukowski *et al.*, J. Am. Chem. Soc. **135**, 10274 (2013).

[154] J. Kang *et al.*, Applied Physics Letters **102**, 012111 (2013).

[155] H. Jiang, The Journal of Physical Chemistry C **116**, 7664 (2012).

[156] J. Heising and M. G. Kanatzidis, Journal of the American Chemical Society **121**, 11720 (1999).

[157] Y. Li *et al.*, Catal. Sci. Technol. **3**, 2214 (2013).

[158] J. K. Nrskov *et al.*, J. Electrochem. Soc. **152**, J23 (2005).

[159] Z.-H. Chi *et al.*, Phys. Rev. Lett. **113**, 036802 (2014).

[160] N. Bandaru *et al.*, The Journal of Physical Chemistry C **118**, 3230 (2014).

[161] A. Bera *et al.*, Phys. Rev. Lett. **110**, 107401 (2013).

[162] Y. Blanter, M. Kaganov, A. Pantsulaya, and A. Varlamov, Physics Reports **245**, 159 (1994).

[163] I. M. Lifshitz, Journal of Experimental and Theoretical Physics **11**, 1130 (1960).

[164] K. P. Meletov *et al.*, Journal of Experimental and Theoretical Physics Letters **75**, 406 (2002).

[165] S. Benhabib *et al.*, Phys. Rev. Lett. **114**, 147001 (2015).

[166] M. Kan, H. G. Nam, Y. H. Lee, and Q. Sun, Phys. Chem. Chem. Phys. **17**, 14866 (2015).

[167] Z. Zhao *et al.*, Nature Communications **6**, 7312 (2015).

[168] S. Goedecker, M. Teter, and J. Hutter, Phys. Rev. B **54**, 1703 (1996).

[169] C. Hartwigsen, S. Goedecker, and J. Hutter, Phys. Rev. B **58**, 3641 (1998).

[170] A. D. Corso and A. M. Conte, Phys. Rev. B **71**, 115106 (2005).

[171] M. Rifliková, R. Martoňák, and E. Tosatti, Phys. Rev. B **90**, 035108 (2014).

[172] Y. Qi *et al.*, Nature Communications **7**, 11038 (2016).

[173] G. Eda *et al.*, ACS Nano **6**, 7311 (2012).

[174] Y. Ma *et al.*, Phys. Chem. Chem. Phys. **13**, 15546 (2011).

[175] Y. Guo, D. Liu, and J. Robertson, Applied Physics Letters **106**, 173106 (2015).

[176] J. Zhao, R. J. Angel, and N. L. Ross, Journal of Physics: Condensed Matter **23**, 175901 (2011).

[177] S. Fathipour *et al.*, Applied Physics Letters **105**, 192101 (2014).

[178] W. G. Dawson and D. W. Bullett, Journal of Physics C: Solid State Physics **20**, 6159 (1987).

[179] D. H. Keum *et al.*, Nature Physics **11**, 482 (2015).

[180] A. N. Enyashin, M. Bar-Sadan, L. Houben, and G. Seifert, The Journal of Physical Chemistry C **117**, 10842 (2013).

[181] M. Bar-Sadan *et al.*, The Journal of Physical Chemistry B **110**, 25399 (2006).

[182] C. Ataca, H. ahin, E. Aktrk, and S. Ciraci, The Journal of Physical Chemistry C **115**, 3934 (2011).

[183] S. McDonnell *et al.*, ACS Nano **8**, 2880 (2014).

[184] H.-P. Komsa *et al.*, Phys. Rev. B **88**, 035301 (2013).

[185] M. Ghorbani-Asl *et al.*, Phys. Rev. B **88**, 245440 (2013).

[186] A. Conan, A. Bonnet, A. Amrouche, and M. Spiesser, Journal de Physique **45**, 459 (1984).

[187] T. Böker *et al.*, Phys. Rev. B **64**, 235305 (2001).

[188] G. K. Madsen and D. J. Singh, Computer Physics Communications **175**, 67 (2006).

[189] N. F. Mott and E. A. Davis, *Electronic processes in non-crystalline materials* (Oxford: Clarendon Press, New York, 1971), bibliography: p. 408-425.

[190] K. Berland *et al.*, Reports on Progress in Physics **78**, 066501 (2015).

[191] T. Thonhauser *et al.*, Phys. Rev. B **76**, 125112 (2007).

[192] B. E. Brown, Acta Cryst. **20**, 268 (1965).

[193] S. Cho *et al.*, Science **349**, 625 (2015).

[194] A. V. Dmitriev and E. S. Tkacheva, Journal of Electronic Materials **43**, 1280 (2014).

[195] M. K. Jana *et al.*, Journal of Physics: Condensed Matter **27**, 285401 (2015).

[196] V. Nicolosi *et al.*, Science **340**, 1226419 (2013).

[197] C. Rao, U. Maitra, and U. V. Waghmare, Chemical Physics Letters **609**, 172 (2014).

[198] A. Mar, S. Jobic, and J. Ibers, Journal of the American Chemical Society **114**, 8963 (1992).

[199] J. Augustin *et al.*, Phys. Rev. B **62**, 10812 (2000).

[200] M. N. Ali *et al.*, Nature **514**, 205 (2014).

[201] I. Pletikosić *et al.*, Phys. Rev. Lett. **113**, 216601 (2014).

[202] S. Tongay *et al.*, Nat. Commun. **5**, 3252 (2014).

[203] J. Chen *et al.*, Applied Physics Letters **104**, 242405 (2014).

[204] R. Fei and L. Yang, Applied Physics Letters **105**, 083120 (2014).

[205] Y. Akahama, S. Endo, and S. ichiro Narita, Journal of the Physical Society of Japan **52**, 2148 (1983).

[206] X. Ling *et al.*, Proceedings of the National Academy of Sciences **112**, 4523 (2015).

[207] F. Xia, H. Wang, and Y. Jia, Nature Communications **5**, 4458 (2014).

[208] X. Wang *et al.*, Nat Nano **10**, 517 (2015).

[209] J. Yang *et al.*, Light Sci Appl **4**, e312 (2015).

[210] R. Schuster *et al.*, Phys. Rev. Lett. **115**, 026404 (2015).

[211] A. S. Rodin, A. Carvalho, and A. H. Castro Neto, Phys. Rev. B **90**, 075429 (2014).

[212] D. K. Efetov and P. Kim, Phys. Rev. Lett. **105**, 256805 (2010).

[213] A. C. Ferrari *et al.*, Phys. Rev. Lett. **97**, 187401 (2006).

[214] A. Gupta *et al.*, Nano Letters **6**, 2667 (2006).

[215] C. Lee *et al.*, ACS Nano **4**, 2695 (2010).

[216] A. Berkdemir *et al.*, Scientific Reports **3**, 1755 (2013).

[217] A. A. Balandin *et al.*, Nano Lett. **8**, 902 (2008), pMID: 18284217.

[218] C. Faugeras *et al.*, ACS Nano **4**, 1889 (2010).

[219] H. B. Ribeiro *et al.*, ACS Nano **9**, 4270 (2015).

[220] J. Wu *et al.*, Angewandte Chemie International Edition **54**, 2366 (2015).

[221] A. Favron *et al.*, Nat Mater **14**, 826 (2015).

[222] A. Brown and S. Rundqvist, Acta Crystallographica **19**, 684685 (1965).

[223] R. W. Keyes, Phys. Rev. **92**, 580 (1953).

[224] D. Warschauer, Journal of Applied Physics **34**, 1853 (1963).

[225] S. P. Koenig *et al.*, Applied Physics Letters **104**, 103106 (2014).

[226] J. C. Jamieson, Science **139**, 1291 (1963).

[227] T. Kikegawa and H. Iwasaki, Acta Cryst. **B39**, 158 (1983).

[228] H. Kawamura, I. Shirotani, and K. Tachikawa, Solid State Communications **49**, 879 (1984).

[229] J. Wittig and B. T. Matthias, Science **160**, 994 (1968).

[230] K. Pal and U. V. Waghmare, Applied Physics Letters **105**, 062105 (2014).

[231] X. Xi *et al.*, Phys. Rev. Lett. **111**, 155701 (2013).

[232] P.-L. Gong *et al.*, Phys. Rev. B **93**, 195434 (2016).

[233] Z. J. Xiang *et al.*, Phys. Rev. Lett. **115**, 186403 (2015).

[234] D. Gresch *et al.*, arXiv:1610.08983v1 (2016).

[235] A. A. Soluyanov and D. Vanderbilt, Phys. Rev. B **83**, 235401 (2011).

[236] J. Bhattacharjee and U. V. Waghmare, Phys. Rev. B **71**, 045106 (2005).

[237] Y. Takao and A. Morita, Physica B+C **105**, 93 (1981).

[238] R. Fei, V. Tran, and L. Yang, Phys. Rev. B **91**, 195319 (2015).